

From design to operation: a suspension platform interferometer for the AEI 10 m prototype

Von der Fakultät für Mathematik und Physik der
Gottfried Wilhelm Leibniz Universität Hannover
zur Erlangung des Grades

Doktorin der Naturwissenschaften
– Dr. rer. nat. –

genehmigte Dissertation von

Dipl.-Phys. Katrin Dahl

geboren am 16. Juni 1983
in Ludwigslust

2013

Referent: Prof. Dr. Karsten Danzmann (Leibniz Universität Hannover)
Korreferent: Dr. Andreas Freise (University of Birmingham)
Korreferent: Prof. Dr. Uwe Morgner (Leibniz Universität Hannover)
Tag der Promotion: 01.07.2013

Abstract

The research presented within this thesis has been performed within the framework of the AEI 10 m prototype. Its aims are to develop new techniques for future generations of gravitational-wave detectors and to be an ultra-low displacement noise facility with excellent seismic isolation provided by three seismic isolation systems located at each end and at the vertex of an L-shaped ultra-high vacuum envelope.

This thesis describes, from concept to operation, a suspension platform interferometer (SPI) consisting of four heterodyne Mach-Zehnder interferometers. The SPI has been designed to sense the relative motion between the three seismically isolated tables in five degrees of freedom and use this information to create a single inertially-quiet rigid platform via feedback to the table's actuators. Simulations of interferometer alignment including cross-coupling of the tables' different degrees of freedom to the interferometer signals are presented.

The interferometers feature quasi-monolithic fiber injectors. The optics are hydroxide-catalysis bonded on an ultra-low expansion base plate. Both provide high mechanical stability. The assembly accuracy using template aided bonding was investigated. To date, three out of four interferometers are fully assembled and operational. The fourth interferometer is waiting on the installation of the third table.

The relative inter-table motion between the south and central tables was interferometrically measured. The relative longitudinal path length signal of the two tables was used to stabilize the tables with respect to each other reducing the residual inter-table motion for all frequencies below 1 Hz. For frequencies below 0.2 Hz, motion was reduced by more than an order of magnitude.

Keywords: gravitational-wave detectors, AEI 10 m prototype, laser interferometer, suspension platform interferometer

Zusammenfassung

Die Untersuchungen, die in dieser Arbeit präsentiert werden, sind im Rahmen des AEI 10 m Prototyp-Projektes durchgeführt worden. Das Projekt beabsichtigt neue Techniken für zukünftige Generationen von Gravitationswellendetektoren zu entwickeln und darüberhinaus eine Einrichtung mit sehr geringem Abstandsrauschen bereitzustellen. Diese beinhaltet exzellente seismischen Isolation, welche durch drei seismische Isolationssysteme gegeben ist, die sich an jedem Ende und in der Ecke eines L-förmigen Ultrahochvakuum-system mit *ca.* 10 m langen Armen befinden.

In dieser Doktorarbeit wurden vier heterodyne Mach-Zehnder-Interferometer, das sogenannte *Suspension Platform Interferometer* (Interferometer zwischen aufgehängten Plattformen), entwickelt, um die verbleibende Relativbewegung zwischen den drei isolierten Tischen in fünf Freiheitsgraden zu messen und eine Unterdrückung dieser Relativbewegung mittels aktiver Rückkopplung zu ermöglichen, sodass sich die drei Tische wie eine Plattform verhalten. Hierfür werden die Aktuatoren in den Tischen genutzt. Des Weiteren werden Simulationsergebnisse bezüglich der Kreuzkopplung zwischen den Interferometersignalen und den verschiedenen Freiheitsgraden des Tisches sowie der Interferometerjustage präsentiert.

Die Interferometer sind mit quasimonolithischen Faserinjektoren ausgestattet. Die Optiken sind mittels der *hydroxide-catalysis bonding* Technik mit einer Basisplatte, die aus einem Material mit sehr geringen thermischen Ausdehnungskoeffizienten besteht, verbunden. Beides führt zu einer hohen mechanischen Stabilität des Aufbaus. Die erreichte Genauigkeit beim Verbinden der Komponenten, die mittels einer Schablone justiert wurden, wurde untersucht. Bis jetzt sind drei von vier Interferometern vollständig aufgebaut und in Betrieb genommen.

Die Relativbewegungen zwischen dem Süd- und Zentraltisch wurden interferometrisch vermessen. Das Messsignal der relativen, longitudinalen Bewegung wurde genutzt, um den relativen, longitudinalen Abstand zwischen bei-

den Tischen für Frequenzen unterhalb von 1 Hz zu stabilisieren. Die relative Bewegung zwischen den Tischen konnte für Frequenzen kleiner als 0,2 Hz um mindestens eine Größenordnung reduziert werden.

Schlagworte: Gravitationswellendetektoren, AEI 10 m Prototyp, Laserinterferometer, *Suspension Platform Interferometer*

Contents

Abstract	iii
Zusammenfassung	iv
List of Figures	xi
List of Tables	xv
Glossary, Acronyms, and Variables	xvii
1. Introduction	1
1.1. Motivation for a suspension platform interferometer	2
1.2. Outline of this thesis	4
2. The AEI 10 m prototype	7
2.1. Planned experiments	7
2.2. Sub-systems of the AEI 10 m prototype	11
2.3. Conclusion	18
3. Measurement concepts	19
3.1. Displacement measurement experiments	19
3.1.1. Cavity	19
3.1.2. Digitally enhanced heterodyne interferometry	20
3.1.3. Homodyne Mach-Zehnder interferometry	20
3.2. Heterodyne Mach-Zehnder interferometry	21
3.2.1. Interferometer signals	21
4. Electro-optical and mechanical design	27
4.1. Design considerations and constraints	27
4.2. Mechanical component design	29

4.3. Minimization of cross-coupling	30
4.4. Interferometer setup / Angle of incidence	31
4.4.1. Polarizing optics	31
4.4.2. Retroreflector corner cube	32
4.4.3. Small angle	32
4.5. Beam parameter	32
4.5.1. Lenses	34
4.5.2. Curved mirror	35
4.6. Laser source	36
4.7. Frequency modulation and phase readout	37
4.7.1. Frequency modulation	37
4.7.2. Phase meter	37
4.7.3. Phase meter interface	39
4.8. Test setup	40
4.9. Optical layout of the SPI	43
4.10. Input beam alignment	49
4.11. Polarization control	51
4.12. Minimum contrast	52
4.13. Conclusion	54
5. Simulations	55
5.1. Signal dependency on interferometer alignment	57
5.1.1. <i>xy</i> -direction	57
5.1.2. Transversal and yaw degree of freedom	59
5.1.3. Coupling factors	62
5.2. Signal range	67
5.3. Impact of the radius of curvature	67
5.4. South interferometer	69
5.5. Conclusion	71
6. Construction	73
6.1. Bonding techniques	73
6.1.1. Hydroxide-catalysis bonding	73
6.1.2. Optical contacts	75
6.1.3. Optocast 3553-LV-UTF	76
6.2. Alignment and accuracy of non-critical components	77
6.3. Fiber injectors	82
6.3.1. Commercial fiber injectors	82
6.3.2. Retrofitting with quasi-monolithic fiber injectors	84
6.3.2.1. Pitch and beam height alignment	85

6.3.2.2.	Yaw alignment	90
6.3.2.3.	Additional polarization beam splitter	90
6.4.	Alignment of critical components	91
6.4.1.	Coordinate measurement machine aided alignment	92
6.4.2.	Recombining beam splitters	93
6.4.3.	South interferometer	93
6.5.	Characterization of the optical bench	95
6.5.1.	Arm length of the interferometers	95
6.5.2.	Beam profile, radius of curvature, and contrast	96
6.6.	Conclusion	98
7.	Performance	101
7.1.	Sensitivity of the phase meter	101
7.2.	Sensitivity of the SPI	103
7.3.	Measurement of seismic motion	104
7.3.1.	Measurement of coupling factors	106
7.3.2.	Inter-table distance stabilization	109
7.4.	Measurements between seismically isolated tables	111
7.5.	Conclusion	116
8.	Thesis conclusion and outlook	119
	Appendix	122
A.	Nominal optical setup	123
A.1.	Optocad file of the simplified setup	123
A.2.	Optocad file of the full setup	123
A.3.	Interferometer arm length	127
B.	IFOCAD coordinates of the bonded setup	129
C.	Coordinate measurement machine	133
C.1.	Background information	133
C.2.	Settings	134
C.3.	Error analysis of CMM measurements	134
C.3.1.	Distance and position measurement	137
C.3.2.	Diameter measurement	137
D.	Re-use of a Zerodur base plate	141
	References	143

List of publications	155
Acknowledgements	160
About the author	163

List of Figures

1.1. Schematic of the suspension point/platform interferometer. . .	2
1.2. Design goal of the SPI.	4
2.1. Expected displacement sensitivity of the SQL interferometer. . .	8
2.2. Interferometric initial configuration of the SQL experiment. . .	9
2.3. Displacement sensitivity curve of the initial configuration. . . .	11
2.4. CAD drawing of the AEI 10 m prototype.	12
2.5. Schematic side view of the SAS.	13
2.6. Photograph of the SAS before installation.	14
2.7. LVDT position within a table.	15
3.1. Schematic of a heterodyne Mach-Zehnder interferometer.	21
3.2. Relationship between LPS and LDS signals.	23
3.3. Schematic of differential wave-front sensing.	24
3.4. Schematic of the QPD labeling.	25
4.1. Configurations for inter-table displacement measurements.	28
4.2. CAD drawing of the populated central table.	29
4.3. Dimensions of the bonded components.	30
4.4. Angle of incidence configurations.	31
4.5. Photograph of the 5 axes mount attached to base plate.	33
4.6. Beam profile for a setup using a curved mirror.	35
4.7. Frequency noise of different laser systems.	36
4.8. Simplified sketch of the phase demodulation scheme.	38
4.9. Photograph of the test setup.	40
4.10. Schematic optical layout of the test setup.	41
4.11. Remote mirror shifted longitudinally.	42
4.12. Remote mirror rotated in yaw.	42
4.13. Remote mirror rotated in pitch.	43

LIST OF FIGURES

4.14. Full optical layout of the SPI.	45
4.15. Four interferometers of the SPI.	47
4.16. Schematic of the alignment of the input beams.	50
4.17. Photograph of the QPD mounts.	51
5.1. Simplified optical setup.	56
5.2. Interferometer signals dependent on beam displacement in the horizontal plane.	56
5.3. Sketch of transversal shift coupling to LPS signal.	59
5.4. Interferometer signals dependent on beam misalignment in the transversal and yaw degree of freedom.	60
5.5. Sketch of beam misalignment coupling to interferometer signals.	61
5.6. Inter-table coordinate system.	62
5.7. Expected path length noise spectra.	66
5.8. Interferometer signals dependent on radius of curvature.	68
5.9. Simplified optical setup.	69
6.1. Cleaning procedure of surfaces.	74
6.2. Photographs of different types of bonding.	75
6.3. Photographs of the template.	77
6.4. Schematic of the used coordinate system.	78
6.5. Bonding accuracy of mirrors and beam splitters.	79
6.6. 5-axes mount.	82
6.7. Beam direction measurement using a CQP.	83
6.8. Beam fluctuations.	84
6.9. Quasi-monolithic fiber injector.	86
6.10. Alignment setup of the quasi-monolithic fiber injector.	87
6.11. Alignment tool.	91
6.12. Almost finished SPI.	92
6.13. Alignment of the mirror M7.	95
6.14. Beam profile of the interfered beams.	97
6.15. Wavefront measurements.	98
7.1. Phase meter noise.	102
7.2. Displacement noise of the diagnostic interferometer.	102
7.3. Photograph of the south arm of the SPI.	104
7.4. Inter-table displacement with one clamped table.	105
7.5. Fundamental mode of a table due to Fluorel.	105
7.6. Time series of SPI length and LVDT Y signal.	106
7.7. Coupling factor measurement from y direction to DLDS signal.	107
7.8. Coupling of an excitation to LVDT signals.	108

7.9. Sketch of the relative longitudinal inter-table control.	110
7.10. Bode plot of servo and plant in y direction.	111
7.11. Stabilized inter-table motion with one table clamped.	112
7.12. DPS signals of the south interferometer.	113
7.13. Inter-table displacement of seismically isolated tables.	114
7.14. Impact of servo gain on open-loop signals.	115
8.1. Suggested position of an improved SPI.	120
C.1. Example of a distance measurement.	135
D.1. Rough Zerodur base plate before and after de-bonding.	142
D.2. Polished/polished bonded components.	142

List of Tables

2.1. Parameters of the initial and marginally stable configuration. . .	10
4.1. Design arm length mismatch.	46
4.2. Quantities for minimum contrast calculation.	53
5.1. Coupling factors; pivot point below table top.	64
5.2. Range of linear signal response.	65
5.3. Signal range of the remote interferometers.	67
5.4. Interferometer signals for different positions of BS7.	70
6.1. Beam parameters of the quasi-monolithic fiber injectors.	85
6.2. Measured beam parameters of the south interferometer.	96
7.1. Measured coupling factors.	107
A.1. Nominal arm length of SPI interferometers.	127
C.1. Measurement conditions and specifications of the CMM.	134
C.2. CMM error analysis for distance and position measurement. . .	136
C.3. Error analysis for diameter measurement with CMM.	138

Glossary, Acronyms, and Variables

Glossary

AEI is the name of the Albert-Einstein-Institute, Hannover.

aLIGO advanced Laser Interferometer Gravitational Wave Observatory. Currently, the Laser Interferometer Gravitational Wave Observatory (LIGO) is upgraded to aLIGO. There are three LIGO detectors, each in a Fabry-Perot Michelson configuration. Two detectors of 4 km and 2 km arm length are located in Hanford, WA, USA. The third detector having an arm length of 4 km is located in Livingston, LA, USA. The upgrade to aLIGO includes higher laser power (200 W), heavier test masses (40 kg), implementation of signal recycling, *etc.*, see [1] for more information.

ANSYS is an engineering simulation software for finite element analysis.

BOSEM is a Birmingham University version of an optical sensor and electro-magnetic actuator [2]. It provides sensing and low frequency damping of suspension resonances.

CAD computer-aided design. A CAD drawing is a technical drawing created with a computer program such as Autodesk Inventor.

CLIO Cryogenic Laser Interferometer Observatory

CMM stands for coordinate measurement machine. A device to measure coordinates of a point on a work piece with μm accuracy. The measurement of several points in combination with data analysis software allows the geometric properties of the workpiece to be determined, *e.g.* length, surface roughness, *etc.*

CQP is a calibrated quadrant photo diode pair to measure position and direction of an incident beam with high accuracy [3, Chapter 3]. To achieve this, the CQP is mounted onto a hexapod which is aligned such that the incident beam hits both quadrant photo diodes at their center. Next, the position of the CQP relative to the coordinate system of the beam is measured with the CMM. The CMM output is evaluated by a computer program calculating the beam's direction and position within the chosen coordinate system.

CTE is the coefficient of thermal expansion. Within this thesis CTE denotes the linear CTE which is defined as $\alpha = \frac{1}{L} \frac{dL}{dT}$ with L being the total length of the material, and dL being the induced length change due to the temperature change dT .

EPP enhanced parallel port, a bidirectional computer interface with a speed of up to 2 MB/s. It was often used to connect printers to a computer.

GAS stands for geometric anti-spring. It is a passive mechanical isolator consisting of compressed blade springs. A GAS filter provides vertical isolation [4]. Each table of the three in-vacuum tables of the AEI 10 m prototype sits on three GAS filters.

GRACE the Gravity Recovery and Climate Experiment is a US-German satellite mission launched successfully in 2002. It consists of two satellites flying in a low Earth orbit mapping the Earth's gravity field. The orbital motion of each satellite senses local variations of the Earth's gravity field. This leads to small fluctuations of the inter-satellite distance. In addition to the micro-wave technology, the GRACE follow-on (GRACE-FO) mission will be equipped with laser interferometers resulting in a higher measurement resolution.

HAM-SAS stands for horizontal access module seismic attenuation system [5]. It is a passive isolation system designed to support mirror suspensions in horizontal access modules of aLIGO's vacuum system, and was developed within the seismic isolation research program for aLIGO. The SAS for the AEI 10 m prototype has been developed based on the HAM-SAS design.

KAGRA The Large Scale Cryogenic Gravitational Wave Telescope, LCGT, has recently been renamed KAGRA. KA stands for Kamioka, and GRA stands for Gravity and Gravitational wave [6].

LISA The Laser Interferometer Space Antenna is a planned spaceborne gravitational-wave detector. LISA consists of three spacecraft forming a triangle with 5 Gm arm lengths and following the Earth by 20° in its orbit around the Sun. Heterodyne Mach-Zehnder interferometers measure the distance changes between the spacecraft in order to detect gravitational waves. LISA is designed to have its best sensitivity between 0.1 mHz and 0.1 Hz [7].

LISA Pathfinder is a precursor technology demonstration mission to test techniques for LISA, which cannot be tested on Earth, e.g. drag-free attitude control of a spacecraft and high precision measurement of two free-falling test masses [8].

LZH is the name of Laser Zentrum Hannover e.V. Hollerithallee 8, Hannover, Germany

MPE_E is the maximum permissible error for length measurement. It specifies the deviation when measuring distances and diameters. It is a measure of the accuracy of the CMM and is determined by ISO standard 10360.

Nd:YAG neodymium-doped yttrium aluminum garnet, is a crystal used as an active lasing medium. It has transitions at 940 nm, 1064 nm, 1120 nm, 1320 nm, and 1440 nm. The most common use of an Nd:YAG crystal is as a lasing medium for a laser emitting light at a wavelength of 1064 nm.

Nd:YVO₄ neodymium-doped yttrium orthovanadate, a birefringent crystal used as an active lasing medium. Its most popular transition is at 1064 nm.

UDP user datagram protocol. It is a network communications method providing a set of network protocols for, e.g. the Internet.

UHV stands for ultra-high vacuum and defines a pressure below 10^{-6} Pa which corresponds to 10^{-8} mbar.

UV stands for ultraviolet which is light of a wavelength between 10 nm and 380 nm.

Acronyms

ABS	absolute value of a complex number
ADC	analogue-to-digital converter
AOM	acousto-optic modulator
AR	anti-reflection
ARG	argument of a complex number
beamM	measurement beam
beamR	reference beam
bin	bin of the single bin discrete Fourier transform
BR	beam recombiner
BS	beam splitter
CDS	control and data system
dc	very low or zero frequency
DPS	differential power signal
DWS	differential wavefront sensing
FI	Faraday isolator
FIOS	fiber injector optical subassembly
HR	high reflection
HWP	half-wave plate
LDS	longitudinal displacement sensing
LPS	longitudinal path length sensing
LVDT	linear variable differential transformer
MS	mirror on south table
MW	mirror on west table
PD	photo diode
PDD	photo diode of the diagnostic interferometer
PDR	photo diode of the reference interferometer

PDS	photo diode of the south interferometer
PDW	photo diode of the west interferometer
PMI	phase meter interface
QPD	quadrant photo diode
QWP	quarter-wave plate
SAS	seismic attenuation system
SBDFT	single bin discrete Fourier transform
SPI	suspension platform interferometer
SQL	standard quantum limit
ul,ur,ll,lr	quadrants of a quadrant photo diode

Variables with capital letters

C	interaction constant
D_{eff}	effective spring constant
D_{grav}	gravitational (anti-)spring constant
E	amplitude of the electromagnetic field of a beam
F	force
NA	numerical aperture
N_{FFT}	length of the Fourier transform
P	power of a laser beam

Variables with lower case letters

c	contrast of a measured power in a heterodyne interferometer
c_0	speed of light in vacuum, $c_0 = 299792458 \frac{\text{m}}{\text{s}}$
d	distance
dof	degree of freedom
e	Euler's number, $e = 2.71\dots$
f	frequency
f'	focal length
f_{het}	heterodyne frequency
f_{laser}	frequency of the laser used, $f_{\text{laser}} = \frac{c_0}{\lambda_{\text{laser}}}$ with $\lambda_{\text{laser}} = 1064 \text{ nm}$
f_{res}	resolution frequency
f_{samp}	sampling frequency of the ADC

g	gravitational acceleration
i	imaginary unit, $i^2 = -1$
k	wave number, i.e. $k = \frac{2\pi}{\lambda}$
l	length
m	mass
p	parameter
r	radial distance
t	time
w_0	beam radius at waist
y_i^A	time series of channel A
z_0	Rayleigh length

Variables with Greek letters

ΔL	measured arm length change of the interferometer
Δs	path length noise of the interferometer
η_{het}	heterodyne efficiency
λ	wavelength of the laser used
ω	angular frequency, $\omega = 2\pi f$
ω_{het}	angular heterodyne frequency, $\omega_{\text{het}} = 2\pi f_{\text{het}}$
$\tilde{\omega}$	van der Waals potential per unit area between two facing solids
ϕ	phase of a measured power in a heterodyne interferometer
π	ratio of a circle's circumference to its diameter, $\pi = 3.14\dots$
ρ	number of particles per unit volume of a solid
Θ	beam divergence

List of symbols

c^*	complex conjugate
\hbar	Planck constant
\Im	imaginary part of a complex number
\Re	real part of a complex number
\overline{P}	time average, e.g. mean power
\mathcal{F}	finesse

CHAPTER 1

Introduction

Gravitational waves follow from Albert Einstein's general theory of relativity [9; 10]. They are generated by accelerated objects in space, *e.g.* binary star systems [11], and result in time-dependent curvatures of space-time. Their polarization is h_+ or h_\times . Gravitational waves have a quadrupole moment. An h_+ polarized gravitational wave, propagating along the z axis, stretches and compresses the space-time in x direction with the frequency of the gravitational wave. In the perpendicular y direction the space-time is squeezed and expanded with opposite sign. Thus, Michelson laser interferometers [12] are a suitable tool for the direct detection of gravitational waves. An international network of ground-based interferometric gravitational-wave detectors, consisting of GEO 600 [13], the two LIGO [14], and the VIRGO [15] detectors exists¹. This has been set up in the last two decades with the aim of achieving the first direct detection of gravitational waves and then do gravitational-wave astronomy. Although several joint science runs of ground-based detectors have been performed [21; 22; 23], the first direct detection of a gravitational wave is still pending. Currently, the detectors are being upgraded with second generation technologies [24; 25] to improve their sensitivity by almost an order of magnitude compared to the first generation.

Some of these new techniques, *e.g.* seismic isolation systems, including advanced suspensions, control topologies, and servo-control systems; have been developed and tested in small-scale prototypes of gravitational-wave detectors such as LASTI [26] at the Massachusetts Institute of Technology or the 40 m

¹Beyond that, several space-based laser interferometers, *e.g.* LISA [16; 17], DECIGO [18], and BBO [19; 20], are planned to measure gravitational waves in the frequency range of a few millihertz to a hertz.

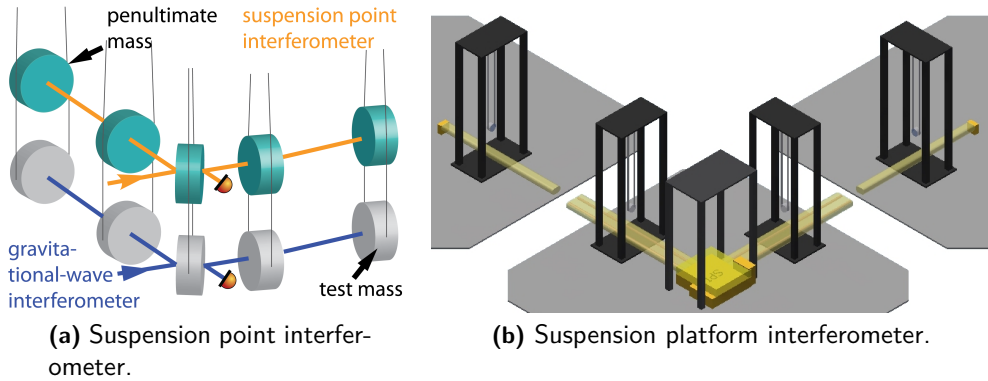


Figure 1.1.: (a) shows the schematic setup of a suspension point interferometer as proposed in [31]. The residual motion between the test masses of the gravitational-wave interferometer is further reduced by setting up an ancillary interferometer between the penultimate masses. Such an interferometer is referred to as a suspension point interferometer. It can be used to stabilize the arm cavities and the differential arm length signal. (b) depicts a simplified setup of a suspension platform interferometer. Here the relative motions between the platforms supporting the suspension cages are measured and stabilized. This configuration is utilized within the AEI 10 m prototype. Drawing (b) has been kindly provided by Conor Mow-Lowry.

prototype [27] at the California Institute of Technology. Other prototypes, *e.g.* the Glasgow 10 m prototype or CLIO [28], develop and investigate new techniques for the time beyond the second generation [29; 30]. All prototypes are aiming for the development and improvement of techniques to further increase the sensitivity of gravitational-wave detectors. One of these techniques is the development of an ancillary interferometer, the so-called suspension point or platform interferometer, to measure and subsequently pre-stabilize the displacements between the suspended test masses of the detector. The motivation for this ancillary interferometer is presented in the next section.

1.1. Motivation for a suspension platform interferometer

A suspension point/platform interferometer is an active vibration isolation tool which has been proposed in the late 1970s [31; 32]. Its name originates from the fact that this ancillary interferometer is located either at the suspension point of the gravitational-wave detector's test masses (see Figure 1.1a) or

on the platform carrying the test masses' suspension cage; see Figure 1.1b. This additional interferometer (abbreviated as SPI in the following) measures the relative motion between the various penultimate masses/platforms. Next, feedback is applied to actuate the penultimate mass/platform to suppress the relative motion between them. In this way the residual motion on the test mass is reduced compared to operation without SPI [33]. This is of special interest to further improve the sensitivity of gravitational-wave detectors in the low frequency regime (< 1 Hz) because passive seismic isolation systems start at best at a few hundreds of millihertz [34], typically around a hertz [35]. So far, no SPI has been implemented in ground-based gravitational-wave detectors because they were not aiming to be sensitive in this low frequency region. Hence, it was omitted to save additional costs and reduce the complexity of the setup.

Nevertheless, the SPI will be a necessary technique to improve the sensitivity of gravitational-wave interferometers at low frequencies in the future [36]. Another advantage of an SPI is that the gravitational-wave interferometer is much more stable. Thus, the requirements on force of the actuators within the test mass suspensions, *e.g.* coil-driver, can be relaxed. Noise sources which are introduced at the stage of the gravitational-wave interferometer, *e.g.* radiation pressure noise, various laser noise sources, and thermal coating Brownian noise, cannot be minimized by an SPI. But noise sources which are not directly coupled into the gravitational-wave interferometer, *e.g.* seismic noise, electronic noise introduced at higher isolation stages, can be reduced by an SPI.

The advantage of a suspension point interferometer over a suspension platform interferometer is that almost no additional hardware is needed, *e.g.* the penultimate mass needs to be replaced only by optics with an adequate coating and appropriate feedback actuators. Furthermore, the suspension point interferometer measures closer to the actual measurement point of the gravitational-wave interferometer. For this reason the influence of coupling from other degrees of freedom is reduced. Experiments with a suspension point interferometer in a Fabry-Perot interferometer were performed by Aso [37].

The advantage of a suspension platform interferometer over a suspension point interferometer is that the electronic noise introduced by actuating at the suspension platform stage is filtered by the many suspension stages of the test mass. It can be retrofitted to an existing setup and altered without interfering with the gravitational-wave interferometer. In the case of the AEI 10 m prototype the main gain is that not only the one main interferometer utilizing optics suspended from the stabilized platforms benefits from the SPI, but any inter-platform setup. For example it was originally planned to per-

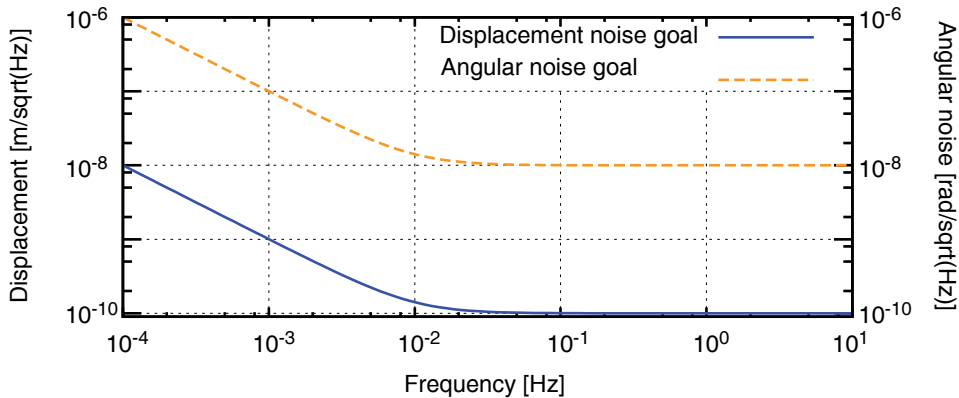


Figure 1.2.: Design goal of the SPI.

form ranging tests with interferometers for the GRACE-FO space mission in the AEI 10 m prototype. For this purpose, the suspension platform interferometer should be able to measure and stabilize the longitudinal differential platform displacements to a level of $100 \text{ pm}/\sqrt{\text{Hz}}$ from 10 mHz to 1 Hz. The angular noise should be below $10 \text{ nrad}/\sqrt{\text{Hz}}$ from 10 mHz to 1 Hz; see Figure 1.2. Due to external constraints these tests were abandoned. However, these specifications were used to design a suspension platform interferometer for the AEI 10 m prototype. The design, construction, and commissioning of the suspension platform interferometer is the topic of this thesis.

1.2. Outline of this thesis

This thesis¹ covers the development of an optical system to measure the relative inter-table motion of three seismically isolated optical tables in five degrees of freedom with the purpose of stabilizing them with respect to each other. This dissertation is split into eight chapters:

Chapter 2 introduces the aspired experiment and the subsystems of the AEI 10 m prototype with special emphasis on the tables, whose relative displacement has been measured within this thesis.

Chapter 3 reviews displacement measurement experiments and familiarizes with the technique of heterodyne Mach-Zehnder interferometry.

Chapter 4 tackles all relevant design considerations leading to the optical layout of the SPI.

¹Excerpts of this thesis have been published in [38; 39; 40].

Chapter 5 presents simulation results on suspension platform interferometer alignment and expected coupling factors.

Chapter 6 illustrates the construction of the SPI's in-vacuum optical system, investigates the alignment accuracies, and closes with a characterization of the system.

Chapter 7 reports measurements of the relative displacement between two tables and features the stabilization of the inter-table motion.

Chapter 8 gives a résumé of this thesis and an outlook for future work.

The AEI 10 m prototype

The research presented within this thesis has been performed within the framework of the AEI 10 m prototype group which was founded in 2008 at the AEI Hannover. Its aim is not only to prototype new techniques for future generations of gravitational-wave detectors, but also to provide a testbed for experiments that require any combination of excellent seismic isolation, a frequency stabilized high-power laser source, an ultra-high vacuum environment, or a length of about 10 m. This chapter describes planned experiments with the AEI 10 m prototype and introduces its individual subsystems with special emphasis on the seismic isolation system of the optical tables. The suspension platform interferometer (SPI) measures their inter-table motion and provides stabilization using the tables' actuators.

2.1. Planned experiments

Among the first experiments within the AEI 10 m prototype facility will be an interferometer which aims for a displacement sensitivity at (and later beyond) the standard quantum limit (SQL) [41]. The SQL is the lower limit of classical interferometer noise and is given by the quadrature sum of quantum radiation pressure noise and shot noise. The origin of the latter are fluctuations of the number of detected photons per time interval. The time of arrival of a photon at a photo detector is independent of the time of arrival of another photon and follows the Poisson distribution. Thus, signal normalized shot noise has a white amplitude spectral density which scales with $1/\sqrt{P}$ with P being the input laser power of the interferometer. Radiation pressure noise is induced by the momentum transfer onto a mirror, if a photon is reflected at a suspended

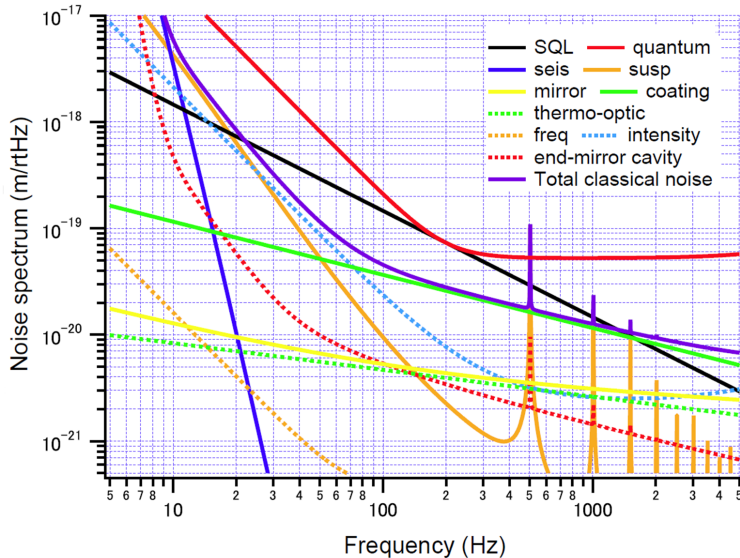


Figure 2.1.: Expected noise contributions of the original design of the SQL interferometer. The quadratic sum of all classical noise sources (violet-colored curve) is below the quadratic sum of quantum noise (red solid line). A variation of the laser power yields a shift of the quantum noise along the black-colored line, labeled as SQL. This graph is taken from [42].

mirror. This momentum transfer changes the mirror position. The higher the laser power the higher the radiation pressure noise. This noise source scales with \sqrt{P} and has a frequency dependence of $1/f^2$ via the mechanical low-pass response of a suspended mirror. Thus radiation pressure noise is the dominant quantum noise source at lower frequencies while shot noise dominates at higher frequencies. The intersection point of both noise sources is shifted to a different frequency when the input laser power of the interferometer is changed. The SQL itself depends on the mirror mass m , the interferometer length L , and the frequency f [11]

$$h_{\text{SQL}} = \frac{1}{\pi f L} \sqrt{\frac{\hbar}{m}} \quad (2.1)$$

and increases when the mirror mass is decreased. In order to measure the SQL of interferometry the sum of all classical noise sources has to be below the quantum noise. A dominant classical noise source is coating Brownian thermal noise. Several possibilities exist to decrease this noise source, *e.g.* increasing the beam diameter, improved coatings, or a reduced number of coating layers.

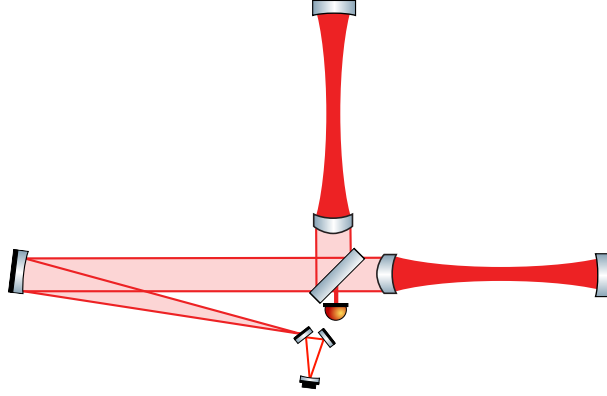


Figure 2.2.: Initial configuration of the SQL experiment consisting of a Fabry-Perot Michelson interferometer. The input beam is filtered by a pre-mode cleaner cavity and converted to a collimated beam by a suspended curved mirror. In this way the incoming beam is matched to the cavity's eigenmode when the cavity length is increased step-wise towards the marginally stable configuration. The interfered beam will also be shaped by a curved mirror (not shown in this figure) and will then be detected by the photo diode.

The last method (in addition to larger beam diameters) was used within the original design document for the SQL interferometer [42] proposing a Fabry-Perot Michelson interferometer with anti-resonant end cavities (see Figure 2.1 for the expected displacement sensitivity) – often referred to as Khalili cavities [43]. The idea is the following: the high reflection (HR) end mirrors of the Fabry-Perot cavities are replaced by compound mirrors consisting of two mirrors. The first mirror has a reduced number of coating layers, thus contributing less coating Brownian thermal noise. The transmitted light is reflected by a second highly reflective mirror which forms a cavity with the mirror having a reduced number of coating layers. The combined reflectivity of the compound mirror is close to that of a single HR coated mirror [44]. A drawback of this configuration is the increased complexity of the interferometer control topology.

Hence, the initial configuration (see Figure 2.2) will be a conventional Fabry-Perot Michelson interferometer with improved coatings: Titania-doped $\text{Ta}_2\text{O}_5/\text{SiO}_2$ mirror coatings. The coating Brownian thermal noise of this type of coating is a factor of two below a mirror coated with pure tantalum pentoxide [45]. Additionally, large beam spots will be used, because coating Brownian thermal noise scales inversely proportional to the beam radius on the mirror surface. In the original design document the proposed beam radius on the cavity mirrors is 9.72 mm which yields to a marginally stable config-

Table 2.1.: Parameters of the initial and marginally stable Fabry-Perot Michelson interferometers.

Parameter	Initial configuration	Marginally stable configuration	Unit
	Value	Value	
Cavity:	length	10.8	11.4 m
	g -factor	0.8	0.998
	finesse	670	670
Cavity mirrors:	radius of curvature	5.7	5.7 m
	diameter	48.6	48.6 mm
	thickness	24.5	24.5 mm
	mass	100	100 g
Beam radius on cavity mirrors	2.86	9.72	mm
Input power	≈ 5	≈ 5	W
Wavelength	1064	1064	nm

uration (cavity length 11.4 m; see Table 2.1) with a cavity g -factor of 0.998 close to instability. For comparison, the highest cavity g -factor of advanced gravitational-wave detector is 0.871 [46]. So far, it is not known how far the arm cavities can be pushed towards instability before the interferometer becomes inoperable. Hence, the initial interferometer configuration has a cavity g -factor of 0.8, an arm cavity length of 10.8 m (see Table 2.1), and a beam radius on the cavity mirrors of 2.86 mm coming at the expense of increased coating thermal noise. It will enable a direct measurement of coating Brownian noise between 100 Hz and 1 kHz; see blue colored curved in Figure 2.3. After successfully commissioning this interferometer, the cavity length will gradually be increased by shifting the end mirrors, resulting in a marginally stable configuration with a cavity length of about 11.4 m. With this stepwise approach, the potential of coating thermal noise reduction will be investigated by increasing the beam radii on the optics. The marginally stable configuration allows to get close to the desired state of operation, with a measured spectrum dominated by quantum noise, see solid orange line in Figure 2.3.

When the cavity length is changed the eigenmode of the cavity differs and the mode matching to the cavity has to be adapted. The mode matching idea for the SQL interferometer is to vary the waist size and not the waist position within the cavities. This is realized by a collimated input beam originating from reflection from a suspended, curved mirror; see Figure 2.2. Next, the collimated beam is matched to the cavities by the anti-reflection (AR) coated,

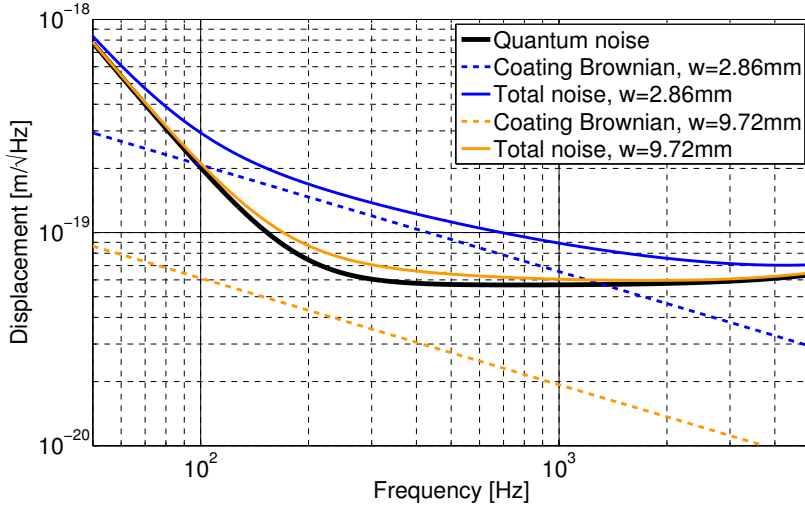


Figure 2.3.: Displacement sensitivity curves for the initial (blue graphs) and the marginally stable (orange graphs) configurations. The quantum noise which is independent of the cavity length is depicted in black. This graph is taken from [46].

rear surfaces of the cavity input mirrors. For further details on this stepwise approach and the SQL interferometer design see [46; 47].

For a study of marginally stable cavities and their lock acquisition no high-quality mirrors, which are rather expensive but a necessity in reaching the SQL, are required. A single interferometer arm using standard quality mirrors will be set up for this study. This single arm setup allows the operation of the novel electro-static drive design for the cavity mirrors to be tested. This leaves the mirror aperture open such that it can be used for transmissive optics. Capacitor plates are placed above and below the mirror, and effect mirror motion when some voltages are applied. Furthermore, the single arm test allows investigations to determine if the beam jitter is sufficiently low or if the design of the input steering mirror suspension has to be revised.

2.2. Sub-systems of the AEI 10 m prototype

Due to its design, the AEI 10 m prototype facility will be a unique experimental testbed. It comprises a large ultra-high vacuum system, seismically isolated tables that are inter-linked, a well-stabilized high-power laser, and a digital control and data acquisition system. The sub-systems are described in the

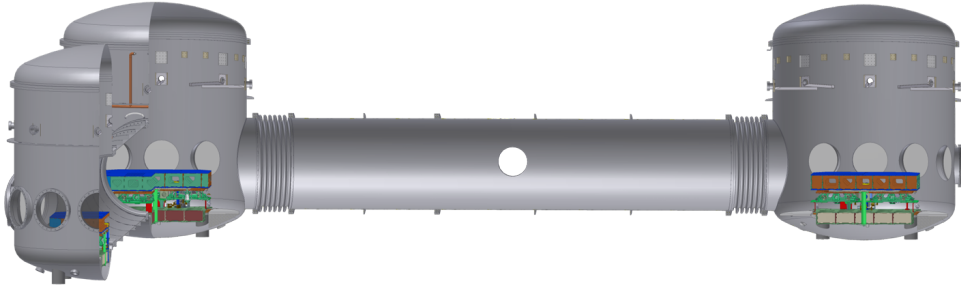


Figure 2.4.: CAD drawing of the AEI 10 m prototype and a view inside. In each tank is a seismic attenuation system supporting an optical table.

following.

Vacuum system

The vacuum system (*cf.* Figure 2.4) of the AEI 10 m prototype has been designed to be flexible and to house more than one experiment at the same time. It consists of three “walk-in” vacuum tanks (\varnothing 3 m, height 3.4 m) arranged in an L-shaped configuration and connected by 8.65 m long tubes (\varnothing 1.5 m). Short pump down times (a pressure of 10^{-6} mbar is reached after 12 h of pumping) are guaranteed by use of one screw pump (with 1751/s pumping rate) starting from atmospheric pressure and two magnetically levitated turbo-molecular pumps (24001/s) that start below 10^{-1} mbar. So far the lowest measured pressure is $\approx 5 \cdot 10^{-8}$ mbar. This pressure is dominated by water vapor.

Seismic attenuation system

The seismic isolation of the optical interferometer components is provided by the seismic attenuation system (SAS). The SAS [48] is a mechanical system carrying an optical bench which will be installed in each of the three tanks. At the time of writing the central and south tanks are equipped with such a system. Even though the SAS is designed as a fully passive system, it is equipped with sensors and actuators for additional active feedback control. The design is based on the HAM-SAS [5] that was developed as part of the seismic isolation research program for aLIGO [1].

A prominent feature of the SAS is the large magnitude of isolation at very low frequencies of a few hundreds of millihertz. Vertical and horizontal isolations are provided by two different devices: geometric anti-springs filters and inverted pendulum legs.

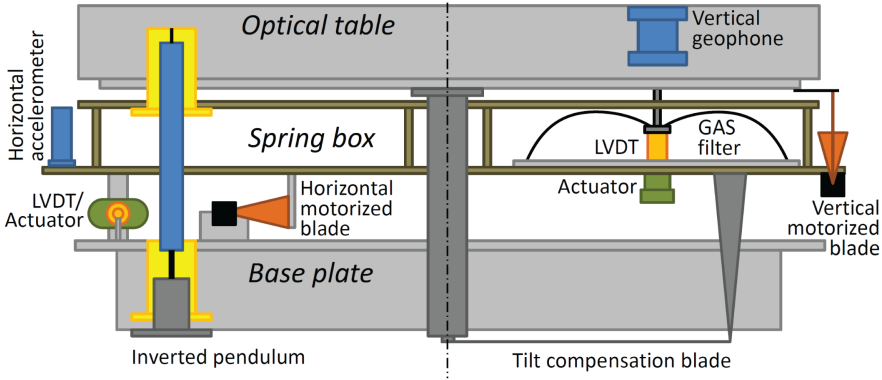


Figure 2.5.: Schematic side view of the SAS. The abbreviation GAS stands for geometric anti-spring. This drawing is taken from [48, p.48].

Horizontal isolation The horizontal isolation stage is composed of three inverted pendulum legs [49; 50], that isolate the spring box (see Figure 2.5) against horizontal ground motion. An inverted pendulum leg is attached to the base plate via a stiff maraging steel flexure and to the spring box via a soft maraging steel flexure. The flexures are the pivot points of the inverted pendulum leg. If the mass on top of the inverted pendulum leg is displaced, *i.e.* if the spring box is displaced by a distance x ($x \ll l$), a force F of

$$F = D_{\text{eff}} \cdot x \quad (2.2)$$

is acting on the spring box [49]. D_{eff} is the effective spring constant

$$D_{\text{eff}} = (D - mg/l) \cdot x \quad (2.3)$$

with m being the mass supported by the inverted pendulum leg which is of length l and the gravitational acceleration g . Due to the gravitational anti-spring effect ($D_{\text{grav}} = -mgx/l$) the resonant frequency of the inverted pendulum can be tuned to very low frequencies. The resonant frequency of the SAS is around 100 mHz. The measured isolation at 4 Hz value is 80 dB.

Vertical isolation The vertical isolation is provided by a set of three geometric anti-spring filters [4]. Such a filter consists of a disk bolted to the spring box and an inner ring, the so-called keystone, carrying the optical table. The disk and the keystone are connected via pairs of cantilever-mounted blade-springs which are radially compressed against each other. This radial compression generates an anti-spring effect, which means that the spring constant is reduced. The resonant frequency of a geometric anti-spring filter is

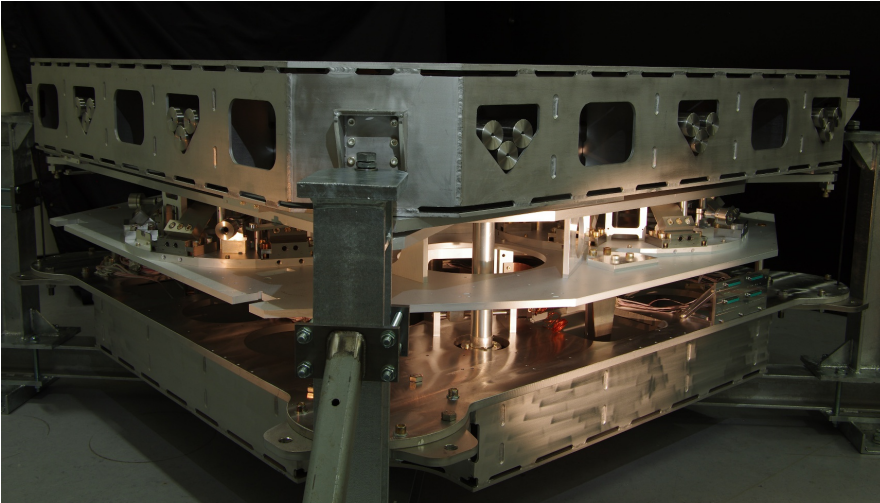


Figure 2.6.: Photograph of the first fully assembled SAS sitting in a horizontal shaker testbed just before installation. The dimensions of the optical bench are $1.75\text{ m} \times 1.75\text{ m}$. Ballast rods are stored in some pockets of the optical table.

about 200 mHz [34]. Best isolation of 60 dB is at a few tens of hertz. This isolation performance could be improved by an additional 20 dB by the use of magic wands [34; 51].

Sensors Different types of sensors are used to monitor displacement of the optical table. Relative motion is sensed by a set of linear variable differential transformers (LVDTs). A LVDT consists of a sensing coil and an actuation coil. The output voltage of a LVDT is proportional to table's displacement and the sign indicates the direction of displacement. LVDTs monitor displacements from dc to 10 Hz with nanoscale resolution [48, p.106].

Three horizontal LVDTs measure the relative motion of the table's spring box to ground. They are located in the vicinity of the inverted pendulum legs; see Figure 2.7. Three vertical LVDTs sense the motion between spring box and intermediate plate carrying the optical table; *cf.* Figure 2.5. They are placed below the keystone of each geometric anti-spring filter, see Figure 2.5.

At frequencies up to 50 Hz, monolithic accelerometers are used to monitor the horizontal inertial motion of the spring box. The sensitivity of such a device is $2.8 \cdot 10^{-10} \text{ms}^{-2}/\sqrt{\text{Hz}}$ at 1 Hz [34]. The vertical inertial motion is sensed by three geophones (L-22D from Mark Products) which are placed inside the optical table.

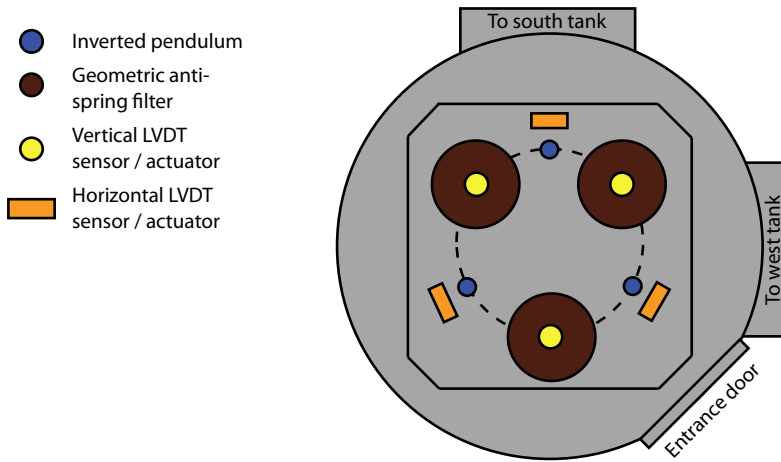


Figure 2.7.: Position of the LVDTs within the horizontal plane of the central table. All displayed devices appear as triplets and are located on circles separated by 120° . The circle's center is the table's center. The radius for the horizontal LVDTs is 787 mm and 525 mm for the vertical LVDTs [48, p.107].

Actuators An SAS is equipped with two types of actuators: motorized blade springs and voice-coil actuators. The latter are part of the aforementioned LVDTs, namely the actuation coil which is co-located with the sensing coil. These coil actuators are used for fine table alignment and modal damping of the fundamental modes of the SAS [48, p.111].

Stepper motorized blade springs [48, p.109] will be also used for alignment of the table position, and to reduce dc load from the voice-coil actuators. Furthermore, they will be used to compensate for thermal drifts. Compared to the LVDTs their noise performance is not as good. At the time of writing the blades were installed, but the implementation of the stepper motor driver to the control and data system (CDS) was not finished. Hence, for all table alignments presented in this thesis, the voice-coils of the LVDTs were used for actuation.

Payload and clamping The SAS has been designed for a defined table payload of 220 kg [48, p.57]. Initially this payload is contributed by ballast rods stored within the optical bench; see Figure 2.6. Whenever anything is put on the table a ballast rod with the corresponding mass has to be removed from the optical bench. Additionally, the table leveling depends on the mass distribution on the table top. This means, that the table will move whenever someone is working on the table, *e.g.* when tightening a screw. Thus,

the table is equipped with clamps between optical bench and spring box to prevent the table's vertical motion, and between spring box and the table's base plate to fix horizontal motion. The seismic isolation performance of the table is shortened when it is clamped. At some points in this thesis the table is called "free" which means the table is not clamped and seismically isolated from ground motion.

Table control As previously mentioned the tables are equipped with sensors and actuators. These are used to control the motion of each table relative to ground and to damp the fundamental table resonances. The residual inter-table motion is measured by the SPI. The derived control signals are fed back to the actuators within the tables. In this way, the relative table displacement is minimized.

Mirror suspensions

Although the seismic attenuation systems of the tables provide excellent seismic isolation, further isolation is needed to be able to measure at the SQL of interferometry for 100 g mirrors. Therefore, all relevant mirrors will be suspended. Three different types of suspensions are utilized: *(i)* steering mirror suspensions, *(ii)* reference cavity mirror suspensions, and *(iii)* the SQL interferometer mirror suspensions.

The steering mirrors have a diameter of 5 cm, a thickness of 1 cm, and a weight of 40 g. The steering mirrors will be suspended as fused silica/aluminum compound mirrors (430 g) by a single horizontal stage. Steel wires will be used for suspension.

The reference cavity mirrors (\varnothing 10 cm, thickness 4.9 cm, 850 g) will be suspended by three suspension stages in series. These all provide horizontal isolation, and the top two stages also provide vertical isolation. The suspension will use steel wires. Local control of the mirrors and damping of eigenmodes will be done at the uppermost stage. Damping and actuation will be provided by means of modified BOSEMs [2]. Passive eddy-current damping will reduce resonant features while active feedback from shadow sensors and magnet-coil actuators will be implemented to further shape the isolation performance and suppress slow environmental changes.

The SQL interferometer mirrors (\varnothing 4.86 cm, thickness 2.45 cm, 100 g) will be suspended by triple pendulum suspensions with two vertical stages of cantilever springs. The final stage of the suspension consists of four fused silica fibers with a diameter of 15 μm . A fused silica final stage is utilized in order to lower the suspension thermal noise arising from mechanical loss in the sus-

pension fibers. Eddy-current dampers and coil-magnet actuators will act on the upper masses and a weaker, less noisy electrostatic drive [52] will act on the test mass.

Laser

Most experiments that will be performed in the AEI 10 m prototype facility, *e.g.* the SQL interferometer, will use a 35 W laser system at a wavelength of 1064 nm. The laser system is a joint development for aLIGO by AEI Hannover and LZH [53]. The multi-stage system is based on a commercially available 2 W Innolight Mephisto [54] with a Nd:YAG crystal in a non-planar ring oscillator configuration. The amplification stage is composed of four Nd:YVO₄ crystals. They are pumped via fiber coupled diodes at 808 nm. More than 95 % of the light is emitted in the fundamental Gaussian mode [53]. The light is injected into the vacuum system by a 5 m long photonic crystal fiber. This fiber serves as a mode cleaner, reducing the higher order mode content of the beam. The laser table moves relative to the isolated in-vacuum table. In comparison with a free space configuration, pointing noise of the fiber output relative to the in-vacuum table will be reduced. This is important since pointing noise at the input of a cavity produces power noise at its output. More than 10 W of power has been transmitted through the 5 m long fiber.

Reference cavity

The laser frequency will be stabilized using a suspended reference cavity between the central and south tables. The reference cavity is a triangular cavity with an optical path length of about 20 m and a finesse of $\mathcal{F} \approx 3000$. The design goal of the reference cavity is to suppress the frequency noise of the laser to a level of about $10^{-4} \text{ Hz}/\sqrt{\text{Hz}}$ at 20 Hz falling off with a $1/f$ slope, and $6 \cdot 10^{-6} \text{ Hz}/\sqrt{\text{Hz}}$ above 1 kHz [55]. A Pound-Drever-Hall [56] scheme will be used to lock the laser frequency to the length of the suspended cavity above the fundamental eigenfrequencies of the suspension systems. The laser will be phase-modulated at 8 MHz with a design modulation depth of 0.6 rad. Several actuators will be used to keep the laser frequency on resonance with the cavity: below 1 Hz the laser crystal temperature will be used to change the frequency, between 1 Hz and 10 kHz a piezo-electric element will act on the laser crystal, and a phase correcting electro-optic modulator will be used above 10 kHz. The target unity gain frequency of the frequency control loop is 250 kHz. The phase lag at the unity gain frequency is 10 degrees, assuming the longest possible control path of 33.2 m, and is thus small enough to cope with additional

phase lag from electronics. An automatic beam alignment system will maintain a stable overlap between the ingoing beam with the cavity fundamental eigenmode [57]. The automatic alignment system consists of two parts: spot position control and wave-front alignment control [58]. Two steering mirrors in front of the reference cavity will be used to correct misalignments with a control bandwidth of a few hertz. The reference cavity mirror suspensions are used as actuators to center the beam on the mirrors with a bandwidth of up to 0.1 Hz.

Control and data acquisition system

The experiments and sub-systems of the AEI 10 m prototype, *e.g.* reference cavity, SPI, *etc.*, will be controlled by a Linux-based digital real-time CDS [59]. The CDS has been developed for aLIGO to run real-time control loops at sample rates of up to 64 kHz. Data will be stored in the frame format on hard disk for later evaluation. For a detailed description of the CDS used for the AEI 10 m prototype see [60].

2.3. Conclusion

The AEI 10 m prototype and its various subsystems were introduced. The most important facts for this thesis are that three seismic attenuation systems each carrying an optical table are orientated in an “L”-shaped configuration in an ultra-high vacuum envelope. The inter-table distance is 11.65 m. Each seismic attenuation system is equipped with six voice-coil actuators to align the table in all six degrees of freedom. These actuators are used to reduce the inter-table motion by applying SPI signals.

This chapter is devoted to measurement concepts. Different concepts to measure displacement are introduced and prominent experiments are presented. It will be explained why a set of heterodyne Mach-Zehnder interferometers is the method of choice for the SPI. The chapter closes with a brief introduction to the technique of heterodyne Mach-Zehnder interferometry, its readout, and output signals.

3.1. Displacement measurement experiments

Different techniques can be used to measure the displacement between two points. Depending on the goal of the measurement it might be advantageous to choose one technique over the other. In the following three displacement measurement experiments and their results are described briefly.

3.1.1. Cavity

An optical resonator is a useful tool to measure tiny changes in displacement between the cavity mirrors. Using a technique like the one of Pound-Drever-Hall [61] the cavity can be locked on resonance. An ancillary cavity (or interferometer) can be installed and locked beside a main interferometric gravitational-wave detector to improve lock acquisition and the operation of the main interferometer, especially at low frequencies. The ancillary interferometer should be set up at the intermediate stage of the suspended mirrors of the main interferometer to reduce their residual rms motions. This idea was proposed in the late 1970s [31] and tested by Aso *et al.* [33]. They measured

40 dB noise reduction between 0.1 Hz and 1 Hz using a suspended 15 cm long Fabry-Perot cavity. Still, this technique is not used for the AEI 10 m prototype SPI because the Pound-Drever-Hall error signal is only available over one laser wave length. The SPI should be able to monitor the differential table displacement over the whole displacement range of the tables, which with ± 5 mm is larger than the usable range of the Pound-Drever-Hall signal.

3.1.2. Digitally enhanced heterodyne interferometry

In digital heterodyne interferometry [62] a digital pseudo-random noise code is modulated on a beam in one of the two interferometer arms. After detecting the beat note at the output port of the interferometer the signal is demodulated with the same pseudo-random noise code. The phase shift between modulation and demodulation is equivalent to the displacement noise. Thus, with a single modulation the displacement between several optics can be measured at the same time. This scheme needs no additional optical components. Digitally enhanced heterodyne interferometry was a new measurement concept at the time of the decision-making process for the best technique for the SPI. No articles on demonstrator experiments showing the performance have been published back then. In the meantime several experiments have been conducted demonstrating the feasibility of the technique of digitally enhanced heterodyne interferometry [63; 64].

3.1.3. Homodyne Mach-Zehnder interferometry

A prototype of a seismic platform interferometer (also abbreviated as SPI) for aLIGO has been set up between two 10 m apart seismic isolation platforms in the Engineering Test Facility at Stanford University [65]. In contrast to the SPI at the AEI 10 m prototype it is not actuated on the remote platform itself but on a mirror glued to a PZT which is located on one of the platforms. The Stanford SPI is a homodyne Mach-Zehnder interferometer and aims to operate at frequencies below 0.5 Hz. The Mach-Zehnder interferometer is locked to mid-fringe. Additionally, the technique of fringe counting is used to measure over more than one optical wave length. The differential length at 10 mHz could be controlled to about $40 \text{ nm}/\sqrt{\text{Hz}}$ which is three orders of magnitude below the differential length measurement when no control has been applied. The relative motion in pitch and yaw was monitored with optical levers and could be reduced by almost one order of magnitude to approximately $70 \text{ nrad}/\sqrt{\text{Hz}}$ at 10 mHz [66]. The disadvantage of the fringe counting technique is that no information on the direction of displacement is available at the maximum and minimum of the sinusoidal fringe signal.

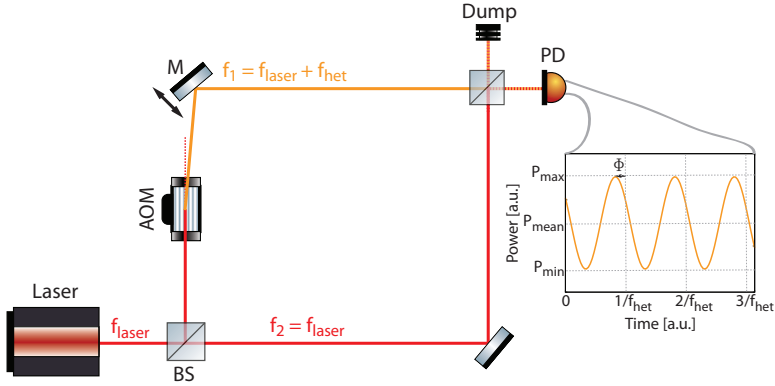


Figure 3.1.: Schematic of a heterodyne Mach-Zehnder interferometer.

3.2. Heterodyne Mach-Zehnder interferometry

For the SPI of the AEI 10 m prototype a decision was made in favor of heterodyne Mach-Zehnder interferometry to monitor the relative motions of the three suspended tables. This technique provides the desired constant performance at any table position over many optical wavelengths. Utilizing heterodyne Mach-Zehnder interferometry the SPI senses all degrees of freedom except for roll about the beam axis. The SPI can operate simultaneously with other experiments conducted in the AEI 10 m prototype and does not interfere with them. Furthermore, the SPI project can benefit from in-house experience gained with experiments for LISA Pathfinder [8].

In the following the concept of heterodyne interferometry is presented. The interferometer signals are derived and the phase measurement system is introduced.

3.2.1. Interferometer signals

The simplest optical layout of a heterodyne Mach-Zehnder interferometer is depicted in Figure 3.1. The laser light is split in two paths. One beam is shifted in frequency by an acousto-optic modulator (AOM) ending with a beam at frequency f_1 . The other beam remains at frequency f_2 . The beams are recombined by a recombining beam splitter and the interference signal of the two beams, which is a sine wave oscillating with the heterodyne frequency, f_{het} ,

$$f_{\text{het}} = f_1 - f_2 \quad (3.1)$$

is detected at the photo diode (PD). The detected power P is computed by integrating over the active area of the photo diode

$$P = \int |E'_1 + E'_2|^2 d^2r \quad (3.2)$$

$$= \int |E_1 \cdot e^{i(\omega_1 t + \varphi_1)} + E_2 \cdot e^{i(\omega_2 t + \varphi_2)}|^2 d^2r \quad (3.3)$$

with $E_{1,2}$ being the electric field amplitude of beam 1 and beam 2, $\omega_{1,2}$ is the angular frequency of the beams ($\omega=2\pi f$), r is the radial distance, and $\varphi_{1,2}$ being the phase of beam 1 and beam 2. Equation 3.3 can be rewritten as

$$P = \int |E_1|^2 + |E_2|^2 + 2|E_1 E_2^*| \cos [(\omega_1 - \omega_2) t + (\varphi_1 - \varphi_2)] d^2r \quad (3.4)$$

using $\omega_{\text{het}} = \omega_1 - \omega_2$ and $\phi = \varphi_1 - \varphi_2$ yields to

$$P = (P_1 + P_2) \left[1 + \frac{2 \int |E_1 E_2^*| d^2r}{P_1 + P_2} \cos(\omega_{\text{het}} t + \phi) \right] \quad (3.5)$$

The maximum, minimum, and mean detected power are

$$P_{\text{max}} = P_1 + P_2 + 2 \int |E_1 E_2^*| d^2r \quad (3.6)$$

$$P_{\text{min}} = P_1 + P_2 - 2 \int |E_1 E_2^*| d^2r \quad (3.7)$$

$$\bar{P} = \frac{1}{2} (P_{\text{max}} + P_{\text{min}}) = P_1 + P_2. \quad (3.8)$$

The contrast of the interferometer is defined as

$$c = \frac{P_{\text{max}} - P_{\text{min}}}{P_{\text{max}} + P_{\text{min}}} \quad (3.9)$$

which is equivalent to

$$c = \frac{2 \int |E_1 E_2^*| d^2r}{P_1 + P_2} \quad (3.10)$$

and

$$c = \frac{P_{\text{Amp}}}{\bar{P}} \quad (3.11)$$

with P_{Amp} being the amplitude of the detected power, *i.e.*

$$P_{\text{Amp}} = \frac{P_{\text{max}} - P_{\text{min}}}{2} = 2 \int |E_1 E_2^*| d^2r \quad (3.12)$$

Using the definition for the contrast (see Equation 3.10) and the mean power (cf. Equation 3.8) Equation 3.5 can be rearranged to

$$P = \bar{P} [1 + c \cos(\omega_{\text{het}}t + \phi)] \quad (3.13)$$

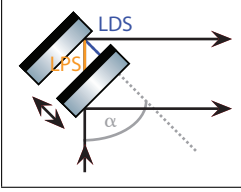


Figure 3.2.: This sketch shows the relation LPS and LDS for Figure 3.1 when mirror M is displaced.

If one of the mirrors in Figure 3.1 is stable and the other mirror is moving, resulting in an optical path length change ΔL , the interferometric signal detected at the photo diode is shifted by phase ϕ . This phase ϕ is related to a length change—the so-called **longitudinal path length sensing (LPS)**—by the wave number k

$$\text{LPS} = \frac{\phi}{k} = \frac{\lambda}{2\pi} \phi \quad (3.14)$$

The LPS signal is related to the longitudinal displacement sensing (LDS) signal which is a measure of the distance the mirror M (see Figure 3.1) has been shifted. The relation between LPS signal and LDS signal depends on the layout of the optical setup. In case of the setup depicted in Figure 3.1 the relation is

$$\text{LDS} = \text{LPS} \cdot \cos \alpha \quad (3.15)$$

This relation is sketched in Figure 3.2.

The heterodyne efficiency, η_{het} , is defined as [67]

$$\eta_{\text{het}} = \frac{|\int E_1 E_2^* d^2r|^2}{P_1 \cdot P_2} \quad (3.16)$$

and is a measure of the matching of two beams on the surface of a photo diode. η_{het} depends on wave-front misalignment as well as tilt and offset between the two beams. The heterodyne efficiency is at maximum when the amplitude and phase of the two beams are matched [68] and both beams are aligned best.

The above equation and Equation 3.10 relate contrast and heterodyne efficiency

$$c = 2 \frac{\sqrt{P_1 \cdot P_2}}{P_1 + P_2} \sqrt{\eta_{\text{het}}} \quad (3.17)$$

Thus, the contrast depends on the power of the individual beams and the wave-front misalignment of the two beams.

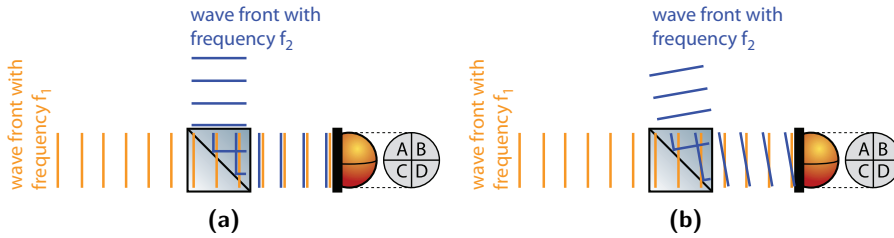


Figure 3.3.: Schematic of differential wave-front sensing (a) with untilted wave fronts and (b) with tilted wave fronts.

Differential wave-front sensing technique

The technique of differential wavefront sensing (DWS) aims to measure angular misalignment between two beams by measuring the differential phase between the wave-fronts of those beams.

To use this technique a single-element photo diode needs to be replaced by a segmented photo diode, *e.g.* a quadrant photo diode (QPD). If no angular misalignment exists between the two beams (see Figure 3.3a) all photo diode segments detect the same phase difference. On the other hand, if the wave-fronts of the two beams are tilted with respect to to each other (see Figure 3.3b) the phase difference is positive on one segment whereas it is negative for the other segment. This information can then be used to realign the angular degree of freedom of the moving mirror M as in Figure 3.1 or to act on the remote tables as in the case of the SPI.

For the SPI QPDs are used in order to measure changes in the pitch and yaw degrees of freedom. The labeling of the QPDs is shown in Figure 3.4a. Throughout this thesis the DWS signals pitch and yaw are defined as the following

$$\text{DWS}_{\text{pitch}} = \phi_{\text{upper}} - \phi_{\text{lower}} \quad (3.18)$$

$$\text{DWS}_{\text{yaw}} = \phi_{\text{right}} - \phi_{\text{left}} \text{ for QPD1} \quad (3.19)$$

$$\text{DWS}_{\text{yaw}} = \phi_{\text{left}} - \phi_{\text{right}} \text{ for QPD2} \quad (3.20)$$

with

$$\begin{aligned} \phi_{\text{upper}} &= \phi_{\text{ul}} + \phi_{\text{ur}} \\ \phi_{\text{lower}} &= \phi_{\text{ll}} + \phi_{\text{lr}} \\ \phi_{\text{left}} &= \phi_{\text{ul}} + \phi_{\text{ll}} \\ \phi_{\text{right}} &= \phi_{\text{ur}} + \phi_{\text{lr}} \end{aligned} \quad (3.21)$$



Figure 3.4.: (a) QPD labeling and coordinate system in the direction of beam propagation and (b) illustration of the need of different formulae for the calculation of the DWS and DPS yaw signals.

and ϕ_{XX} being the phase of photo diode quadrant XX . For the calculation of the DWS_{yaw} signal two formulae are used depending on the QPD which is used for monitoring. The need of the change in sign and the QPD nomenclature is depicted in Figure 3.4b.

Differential power sensing

The differential power signal (DPS) gives information on the beam position on the QPD. The averaged power of each quadrant is used to calculate the DPS for vertical and horizontal directions

$$DPS_z = \frac{\bar{P}_{upper} - \bar{P}_{lower}}{\bar{P}_{upper} + \bar{P}_{lower}} \quad (3.22)$$

$$DPS_x = \frac{\bar{P}_{right} - \bar{P}_{left}}{\bar{P}_{right} + \bar{P}_{left}} \text{ for QPD1} \quad (3.23)$$

$$DPS_x = \frac{\bar{P}_{left} - \bar{P}_{right}}{\bar{P}_{right} + \bar{P}_{left}} \text{ for QPD2} \quad (3.24)$$

with

$$\begin{aligned} \bar{P}_{upper} &= \bar{P}_{ul} + \bar{P}_{ur} \\ \bar{P}_{lower} &= \bar{P}_{ll} + \bar{P}_{lr} \\ \bar{P}_{left} &= \bar{P}_{ul} + \bar{P}_{ll} \\ \bar{P}_{right} &= \bar{P}_{ur} + \bar{P}_{lr} \end{aligned} \quad (3.25)$$

and \bar{P}_{XX} being the averaged power on photo diode quadrant XX . The nomenclature presented in Figure 3.4 is used. The DPS signal can be converted to an absolute position on the QPD. In general, the power P on a QPD at distance x from its center is given by [69]

$$P(x) = \frac{P_{\text{total}}}{2} \left[1 + \operatorname{erf} \left(\frac{\sqrt{2}z}{w_0} \right) \right] \quad (3.26)$$

with beam waist w_0 and the Gaussian error function, erf, being defined as [69]

$$\operatorname{erf}(t) = \frac{2}{\sqrt{\pi}} \int_0^t e^{-t'^2} dt' \quad (3.27)$$

Equation 3.26 can be rearranged to

$$x = \frac{w_0}{\sqrt{2}} \operatorname{erf}^{-1} \left(\frac{2P}{P_{\text{total}}} - 1 \right) \quad (3.28)$$

The term in brackets is equivalent to the above defined DPS signals. Thus, the horizontal, x , and vertical, z , positions of the beam from the center of the QPD (see Figure 3.4a) are:

$$\begin{aligned} x &= \frac{w_0}{\sqrt{2}} \operatorname{erf}^{-1} (\operatorname{DPS}_x) \\ z &= \frac{w_0}{\sqrt{2}} \operatorname{erf}^{-1} (\operatorname{DPS}_z) \end{aligned} \quad (3.29)$$

In case of the SPI, the DPS signals of photo diodes on the central table monitor angular misalignments and will be used for coarse alignment of the remote tables relative to the central table. The DPS signal of the QPDs located on the remote tables also sense lateral shifts of the tables.

Conclusion

A heterodyne Mach-Zehnder interferometer using QPDs as a detector provides six signals: DPS and DWS signals in vertical and horizontal directions, plus contrast and LPS signal. The contrast quantifies the quality of the alignment of the interferometer. The LPS signal is a measure of the longitudinal stability of the two interferometer arms relative to each other. The DWS signal gives information on the angular misalignment of the beams, *i.e.* tilt of the wavefronts, relative to each other. The DPS quantifies the displacement of the beam from the center of the photo diode.

Electro-optical and mechanical design

In the last chapter the technique of heterodyne Mach-Zehnder interferometry was introduced and explained in detail. The next step is to design the Mach-Zehnder interferometers to be able to measure the relative motion between the three tables. Thus, this chapter tackles the electro-optical and mechanical design of the SPI.

4.1. Design considerations and constraints

In total four interferometers are needed to sense the relative motions between the three suspended tables: an (reference) interferometer set up only on the central table to act as reference point for the inter-table motion, an identical copy of this interferometer to determine the sensitivity of the setup, and two interferometers each measuring the relative inter-table motion.

The relative motions of the three tables with respect to each other can be measured by determining the relative motions of the tables with two heterodyne Mach-Zehnder interferometers set up between the following tables:

1. central – south, central – west (see Figure 4.1a);
2. central – south, south – west (see Figure 4.1b);
3. central – west, south – west.

The last two configurations are comparable and similar to LISA Pathfinder [70; 71, p.58]. Their main disadvantage compared to the first configuration is that sensing of the relative table motion is only possible when all three tables are in operation. This is a strong limitation of the utilization of the SPI.

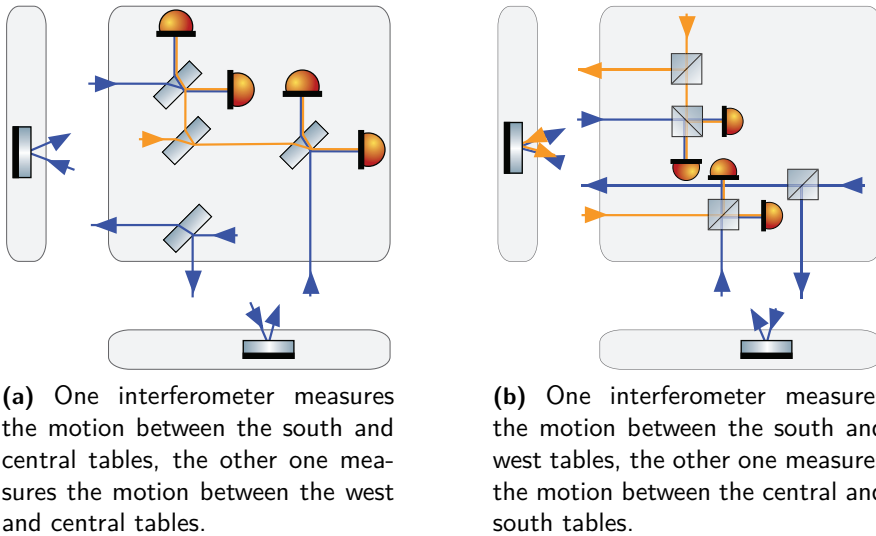


Figure 4.1.: Two possible configurations to measure the inter-table motion between three tables.

Hence, the decision was in favor the first approach. Aiming for a minimum number of components the light of the interferometer is injected on the central table.

The SPI is one of the subsystems of the AEI 10 m prototype. As such some constraints have to be kept in mind within the design phase. These constraints are:

- the whole setup has to be vacuum compatible down to 10^{-8} mbar, which especially means only greaseless components can be used;
- it has to be as light as possible to reduce load on the tables;
- the footprint of the setup should be as small as possible to leave maximum space for other subsystems (see Figure 4.2);
- the experimental setup has to be as short as possible because suspended mirrors will be placed over the SPI optics and beams (see Figure 4.2);
- the setup should need as little maintenance as possible because it won't be easy to reach the setup (again see Figure 4.2); and
- the setup has to provide the mechanical and thermal stability to measure a longitudinal displacement of $100 \text{ pm}/\sqrt{\text{Hz}}$ at 10 mHz.

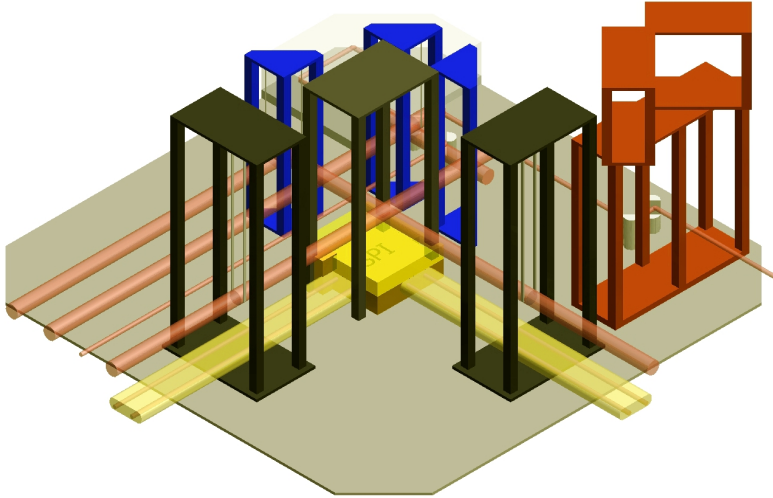


Figure 4.2.: This CAD drawing shows the central table equipped within different suspension cages for the SQL experiments and the SPI. The blue suspension cages are for the steering mirrors, the red ones are for the reference cavity, and the black ones are for the beam splitter and input test masses for the SQL interferometer. The yellow box represents the SPI. The yellow beams illustrate the clearance for the SPI beams. All dimensions are to scale. This drawing has been kindly provided by Conor Mow-Lowry.

4.2. Mechanical component design

All constraints can be met by constructing the SPI of small, non-alignable beam splitters and mirrors bonded onto a small base plate. It was decided that the SPI has to fit onto a base plate with a footprint of $250 \text{ mm} \times 250 \text{ mm}$ per table.

For different base plate materials the maximum tolerable temperature change was calculated for a measurement length of 250 mm and a maximum length change of $100 \text{ pm}/\sqrt{\text{Hz}}$ at 10 mHz . It turns out that the use of an ultra-low expansion material is mandatory for the base plate. Clearceram-Z HS is a ceramic glass with a CTE of $(0.0 \pm 0.2) \cdot 10^{-7} \text{ K}^{-1}$ and a zero-crossing at room temperature [72]. It is used as base plate material. The optical components are made of Suprasil 1 which has a low CTE of $5.1 \cdot 10^{-7} \text{ K}^{-1}$ and a low refractive index to temperature dependency of $9.6 \cdot 10^{-6} \text{ K}^{-1}$ for $\lambda = 1064 \text{ nm}$ [73]. This minimizes the change of the optical path length while the beam propagates through a beam splitter [3]. The dimensions of the used components are depicted in Figure 4.3.

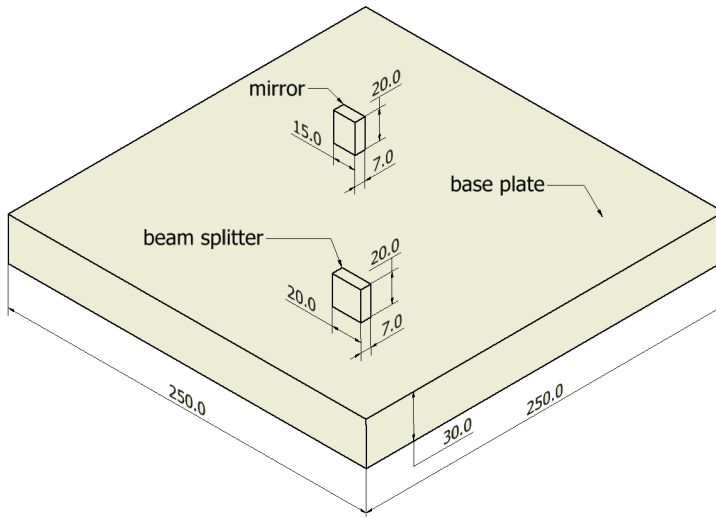


Figure 4.3.: CAD drawing showing the dimensions of bonded components given in mm.

Suprasil 1 and Clearceram-Z HS are silicate-based materials. Components of both materials can form a quasi-monolithic connection by using the technique of hydroxide-silicate bonding. A prerequisite is that the to-be-attached surfaces are polished better than $\lambda/10$ with $\lambda = 633 \text{ nm}$ [74]. During the alignment process the components cannot be adjusted in pitch. Thus, the perpendicularity between the components footprint and its front surface has to be better than $90^\circ 0' 0'' \pm 0^\circ 0' 2''^1$.

The base plate has to be thick enough that its deflection due to gravitational load is below $\lambda/10$. According to Equation (6.2.12) in [75] a base plate made of Clearceram-Z HS and the dimensions shown in Figure 4.3 has a maximum sag of 55 nm being a good compromise in meeting the requirements and minimizing the overall height of the SPI.

4.3. Minimization of cross-coupling

As stated in Section 4.1, the inter-table interferometers have one arm on the central table and the other arm probes the distance to a remote table. In this measurement, coupling from table rotation to translational motion strongly depends on the optical layout. In pitch the pivot point is approximately 346 mm

¹Hydroxide-silicate bonding is discussed further in Chapter 6 on p. 73.

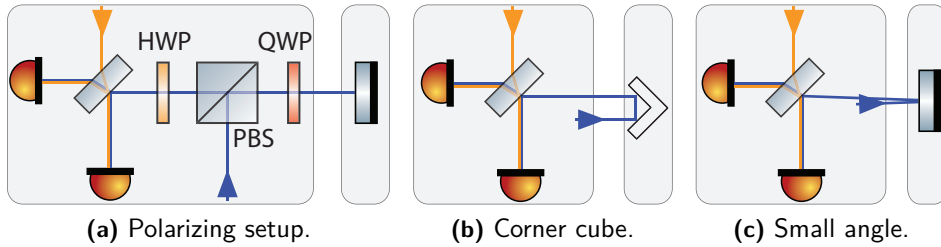


Figure 4.4.: Different possibilities to steer and reflect a laser beam between two tables. (a) utilizes polarizing optics, (b) uses a retroreflector corner cube on the remote table, and in (c) the incoming beam impinges on the remote mirror under a small angle incident.

below the surface of the table. At the height of the pivot point no space is available for the SPI. Thus the coupling from pitch to translational displacement cannot be minimized by positioning of the SPI. In contrast to the yaw degree of freedom, here the table rotates around its central axis due to the symmetric table design. Cross-coupling is minimized if the remote mirrors are placed on the central axis of the table. For a detailed investigation on coupling factors see Section 5.1.3 on p. 62. The positioning of the remote mirrors in the center of the table top implies that the base plate on the central table has to be placed in the center of the central table, too. It is beneficial when these two interferometers are identical copies of each other to ease commissioning of the SPI. Thus, the beam recombiner of the inter-table interferometers are positioned along the line that connects the central axes of the tables.

4.4. Interferometer setup / Angle of incidence

Different alternatives exist to steer the beam towards the remote tables: under a small angle and under normal incidence; see Figure 4.4. The latter can be done either by the use of polarizing optics or by the use of a retroreflector corner cube located on the remote tables. The SPI utilizes the small angle option. The reasons for this choice are presented below.

4.4.1. Polarizing optics

A simplified setup showing the use of polarizing optics is depicted in Figure 4.4a. An *s*-polarized beam (blue colored) is reflected by a polarizing beam splitter, propagates through a quarter-wave plate (QWP), impinges under normal incidence on a mirror on the remote table. The light is reflected

back and passes the QWP again, now being p -polarized. The polarization is rotated to s after passing through the half-wave plate (HWP). The beam is recombined with the other beam (depicted in orange) at the beam recombiner. An advantage of the polarizing optics setup is that a longitudinal displacement of the remote mirror along the beam axis has no impact on the beam overlap at the beam recombiner making the alignment of the interferometer much easier. Nevertheless, it was not chosen for the SPI. At the time of designing the SPI (2008) polarization optics were still suspected to be thermally unstable in transmission. This would cause a change in the optical path length, a change of the polarizing plane, and a varying extinction ratio. Furthermore, it was unclear whether periodic phase errors appear in an interferometer using polarization optics. Thus, it was refrained from using polarizing optics.¹

4.4.2. Retroreflector corner cube

Non-polarizing optics and normal incidence can be used if a retroreflector corner cube is placed on the remote tables. An advantage of a retroreflector corner cube is that a translational shift of the beam does not couple into a longitudinal phase shift. On the other hand, the outgoing beam is reflected back in the direction of the incoming beam. This means no information of a rotation of the remote table is available. Hence, a retroreflector corner cube is not used for the SPI.

4.4.3. Small angle

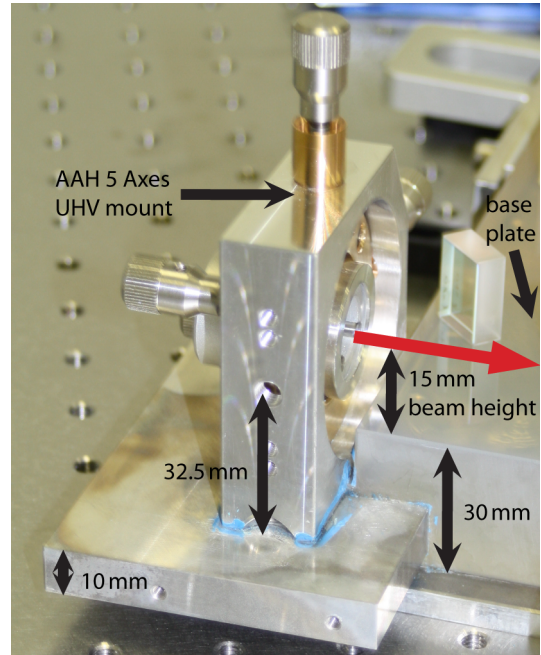
Another possibility is that the beam hits a mirror under a small angle of incidence, see Figure 4.4c. This configuration is used for the LISA Pathfinder proof masses interferometers and has been investigated in great detail [76; 77; 78]. So far, no major disadvantage has been found. A benefit of this setup is that the remote mirror can be used for beam shaping.

4.5. Beam parameter

The laser light ($\lambda=1064$ nm) is coupled into the vacuum system via polarization-maintaining optical fibers. A fiber collimator is connected to the fiber end and shapes the beam to the desired beam parameters.

¹Meanwhile, an experiment has been set up to investigate these concerns. It turned out that no periodic phase error could be measured, see [3]. [3, p. 61-74] gives a good introduction to the issue of periodic phase errors.

Figure 4.5: Photograph of the 5 axes mount attached to base plate showing the important dimensions which had to be considered in the setting of the beam height.



During the design stage only standard, adjustable fiber collimators and mounts were available, but the construction of quasi-monolithic fiber injectors for the SPI was announced for sometime in future. The design of the SPI takes both types of fiber injectors into account. The assembly started with the standard fiber injectors which were later replaced with the quasi-monolithic fiber injectors; see Section 6.3 on p. 82. The beam parameters are independent of the kind of injector and are the same for both types.

The beam height is deduced from the boundary conditions that beam clipping has to be avoided, the aforementioned mirrors and beam splitters of a height of 20 mm should be used, and the dimensions of the adjustable mount holding the standard fiber collimator. This mount has to be adjustable in at least 4-axes (x - and z -directions, pitch, and yaw) to align the two beams parallel to the surface of the base plate and to the same height. The mount AAH 5 Axes UHV mount by MICOS is the only one that fulfills this requirement in addition to the stringent restrictions regarding ultra-high vacuum compatibility. It is a custom-made version of the AAH 5 Axes mount by MICOS [79]. Due to the dimensions of this mount (see Figure 4.5) the minimum beam height is 12.5 mm above the base plate surface. The beam height is set to 15 mm.

This means, the maximum distance between beam center and top of an

optical component is 5 mm. The beam radius should be at maximum one third of this number to avoid beam clipping. A maximum beam diameter, $\varnothing_{\text{beam}}$, of 3.3 mm is possible.

From this number, the focal length f' of the collimating lens is calculated [80, p. 29]

$$f' = \frac{\varnothing_{\text{beam}}}{2 \cdot NA \cdot 0.82} \quad (4.1)$$

Typical values for the numerical aperture, NA , of a polarization-maintaining fiber are between 0.08 and 0.13. The smaller the beam diameter, the larger is the beam divergence, Θ , [80, p. 29]

$$\Theta = \frac{2\lambda}{\pi \varnothing_{\text{beam}}} \quad (4.2)$$

A good trade-off between a small beam diameter and low divergence angle is realized for a beam of the diameter of 2.1 mm, a fiber with an NA of 0.12, and a collimator lens with a focal length of 11 mm. With this set of parameters the beam divergence is $313 \mu\text{rad}$. Within the first meter the beam gains only $30 \mu\text{m}$ in diameter. This is sufficiently constant for interferometers with arm lengths below 1 m. No additional beam shaping optics are needed to ensure a good beam overlap at the beam recombiner. After propagation of 20 m the diameter is six times larger compared to its start. Thus, beam shaping optics are needed. Two options exist: lenses or mirrors.

4.5.1. Lenses

Lenses have to be either bonded onto the base plate or mounted onto adjustable mounts. Bonding of lenses is not trivial. It must be ensured that the beam propagates through the center of the lens. This cannot be guaranteed during operation of the SPI because the tables can move relative to each other by more than the allowed $\pm 1 \text{ mm}$ simulated with `JamMt` [81]. Thus, the beam parameters and the beam direction change when the beam impinges off-center on the lens. Also, it is challenging to align and to bond two lenses at the same time.

The use of adjustable lens mounts induces noise because the mounts and thus the alignment can drift. Again, if the SPI senses the relative table motion and with no feedback applied to the tables, the beam will change its parameters and, worse, its direction. This will make the interpretation of the SPI signals complicated.

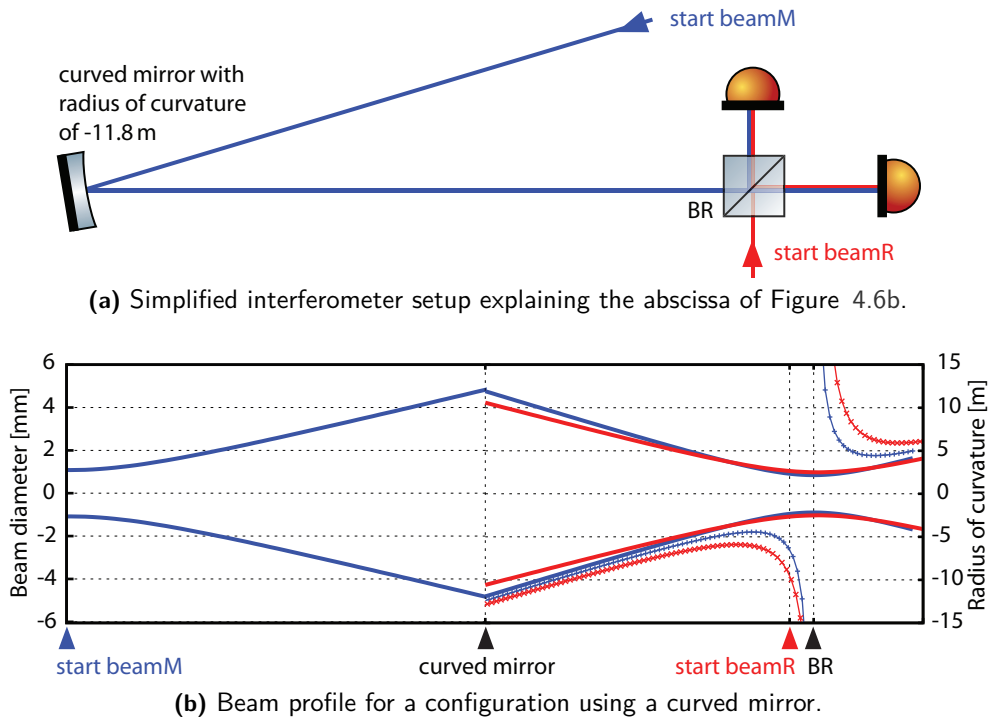


Figure 4.6.: (a) shows a simplified interferometer. For the blue colored beam (beamM) the distance between beam start and beam recombiner (BR) is 23 m. The curved mirror is placed half way. The red colored beam (beamR) propagates 0.4 m from start to BR. Subfigure (b) shows the beam diameter (solid lines) and radius of curvature (lines with points) of the design beam at these positions.

4.5.2. Curved mirror

The simplest approach to integrate a curved mirror into the interferometer is to put it on the remote tables. In this case, the specifications of the center of the radius of curvature are relatively relaxed compared to a situation of a bonded curved mirror on the central base plate. Figure 4.6b shows the beam parameters of the design at different positions. At the beam recombiner BR an interferometric contrast of 99.5% and a heterodyne efficiency of 99.0% can be realized. An advantage of a curved mirror is that the heterodyne efficiency is relatively robust to the mirror's radius of curvature, see Section 5.3 on p. 67. Moreover, the positioning of a curved mirror is less critical compared to a set of lenses. For this reasons the SPI uses a curved remote mirror to shape the beam profile.

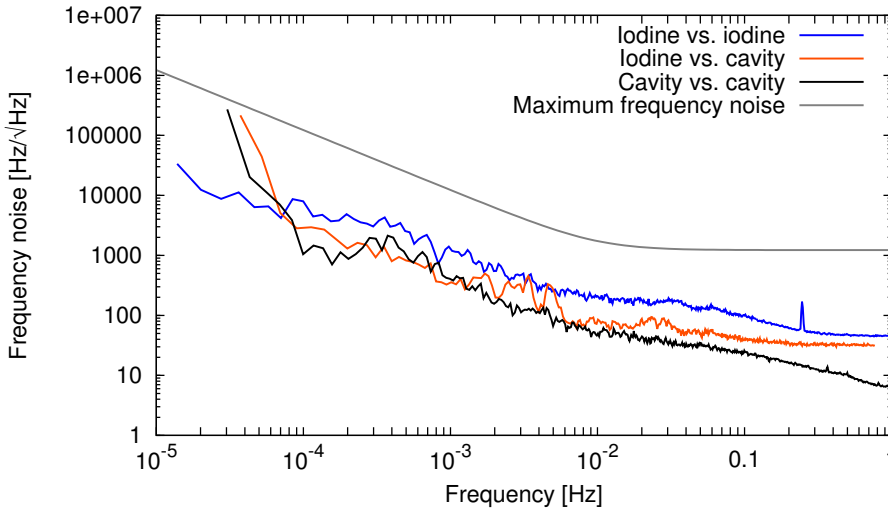


Figure 4.7.: Frequency stability of different laser systems. The stability of the beat note of two laser systems was measured. The blue colored line represents the beat note measurement of two identical iodine-stabilized laser systems as used for the SPI. The orange colored line shows the frequency stability of an iodine-stabilized laser beat with a laser stabilized to a thermally shielded Zerodur cavity [82]. The black colored line shows the frequency fluctuations of two lasers stabilized to such a cavity. The gray colored graph is the maximum allowable laser frequency noise for an interferometer with an arm length mismatch of 23 m aiming for an maximum optical path length noise of $100 \text{ pm}/\sqrt{\text{Hz}}$. These measurements have been kindly provided by Michael Tröbs and were the basis for the decision process for a suitable laser system.

4.6. Laser source

In an interferometer, any arm length mismatch, ΔL , couples proportionally into path length noise, δL , via laser frequency noise, $\delta\nu$,

$$\delta\nu = \frac{c_0}{\lambda} \frac{\delta L}{\Delta L} \quad (4.3)$$

with c_0 being the speed of light and λ the laser wavelength [83].

The measurement beams of the inter-table interferometers see an optical path length of about 23 m with respect to the first in-vacuum beam splitter. The optical path length seen by the reference beam of these interferometers have to have the same value to minimize coupling from laser frequency noise. It is not possible to design interferometers that measure the inter-table motions with no or small ($< 1 \text{ m}$) arm length mismatch. No interferometer with an arm

length mismatch of 23 m sensing only frequency noise and being insensitive to the inter-table motion can be set up. Hence, some interferometers have an arm length mismatch of about 23 m. This yields a maximum allowable laser frequency noise of $1.2 \text{ kHz}/\sqrt{\text{Hz}}$ at 10 mHz aiming for an optical path length noise of $100 \text{ pm}/\sqrt{\text{Hz}}$ at 10 mHz using a laser of the wavelength of 1064 nm. A commercially available iodine-stabilized Nd:YAG laser [84] fulfills this stringent requirement for frequency stability; see Figure 4.7. On this basis an iodine-stabilized laser system has been chosen for the SPI.

4.7. Frequency modulation and phase readout

In this section, the choice of the heterodyne frequency and the phase readout system are presented.

4.7.1. Frequency modulation

A Mach-Zehnder interferometer can be changed from homodyne to heterodyne operation by placing an AOM in one of the two arms of a homodyne Mach-Zehnder interferometer; see Figure 3.1 on p. 21. AOMs modulate light at frequencies in the range of MHz and not in the kHz range. The photo diode electronics incorporated in the phase meter (see Section 4.7.2) are designed for the detection of slow (\ll MHz) signals. A heterodyne signal in the kilohertz range is realized by the use of two AOMs (one in each interferometer arm) shifting the light at $80 \text{ MHz} + \frac{f_{\text{het}}}{2}$ and $80 \text{ MHz} - \frac{f_{\text{het}}}{2}$ respectively; the resulting beat note is at the heterodyne frequency. This frequency difference is stabilized to a reference with a phase-locked loop. 20 kHz is about the maximum frequency difference the AOM drivers can cope with. 15 kHz is the highest heterodyne frequency at which the phase-locked loop operates continuously at different laboratory temperatures. The heterodyne frequency is proportional to the control bandwidth of the interferometer, and thus a high heterodyne frequency is desirable.

4.7.2. Phase meter

The recombined light of all interferometers impinges on QPDs which are located in vacuum; see Figure 4.8. The photo current of each quadrant is fed to the phase meter, a LTP-style phase meter PM3, developed at the AEI [83; 85, p.189], which has 20 channels. The phase meter is synchronized with the phase-locked loop for the two AOMs to allow demodulation. For each channel the photo current is converted into voltages by a trans-impedance amplifier,

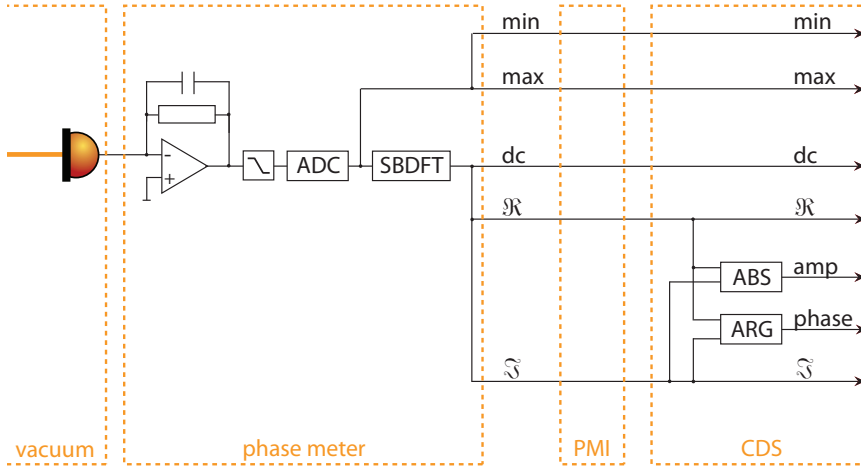


Figure 4.8.: Simplified schematic of the SPI's phase demodulation. The light modulated at the heterodyne frequency is detected by a photo diode. In the phase meter the photo current is converted to voltages by a trans-impedance amplifier, digitized by an analogue-to-digital converter, and Fourier transformed. The output of the phase meter are five signals. The min and max are the ADC's minimum and maximum values of the digitized sinusoidal signal. dc is the signal value at zero frequency. \Re and \Im are the real and imaginary parts of the Fourier transformed signal. These five signals are transferred to the phase meter interface via an EPP. The phase meter interface generates data packets and passes the signals via an ethernet cable to the CDS. Here, phase and heterodyne amplitude are calculated.

digitized by an analogue-to-digital converter (ADC) at a sampling rate, f_{samp} , of 800 kHz, and finally Fourier transformed by a single bin discrete Fourier transform (SBDFT). By choosing the resolution frequency, f_{res} , (or in other words the width of the bin of the single bin discrete Fourier transform (bin)) with which the SBDFT is performed, the frequency bin is defined via [86]

$$\text{bin} = \frac{f_{\text{het}}}{f_{\text{res}}} \quad (4.4)$$

The resolution frequency and the sampling frequency of the ADC are related by the length of the Fourier transform, N_{FFT} , [86]

$$N_{\text{FFT}} = \frac{f_{\text{samp}}}{f_{\text{res}}} \quad (4.5)$$

In the case of the SPI, the following values are used

$$\begin{aligned}
f_{\text{het}} &= 15337.423 \text{ Hz} \\
\text{bin} &= 25 \\
f_{\text{res}} &= 613.4969 \text{ Hz} \\
N_{\text{FFT}} &= 1304
\end{aligned} \tag{4.6}$$

The resolution frequency (which is the phase meter output data rate) of about 600 Hz is more than sufficient for the SPI whose signals will be used for actuation below 1 Hz. Above 1 Hz the SPI signals will be used for additional monitoring.

After the SBDFFT, the phase meter provides three more values for each channel A (in addition to the minimum and maximum values of the ADC; see Figure 4.8): the very low or zero frequency (dc) value, and the real and imaginary amplitude of the complex heterodyne frequency [83]

$$dc^A = \sum_{i=0}^{N_{\text{FFT}}-1} y_i^A \tag{4.7}$$

$$\Re(F^A) = \sum_{i=0}^{N_{\text{FFT}}-1} y_i^A \cdot \cos\left(\frac{i \cdot \omega_{\text{het}}}{N_{\text{FFT}} \cdot f_{\text{res}}}\right) \tag{4.8}$$

$$\Im(F^A) = \sum_{i=0}^{N_{\text{FFT}}-1} y_i^A \cdot \sin\left(\frac{i \cdot \omega_{\text{het}}}{N_{\text{FFT}} \cdot f_{\text{res}}}\right) \tag{4.9}$$

y_i^A is the time series of channel A where the value of the sine and cosine are precomputed and taken from a look-up table. All five values of each channel are transferred via the phase meters' enhanced parallel port (EPP) to the phase meter interface (PMI).

4.7.3. Phase meter interface

Due to the infrastructure of the AEI 10 m prototype, a phase meter interface was required to connect the phase meter to the CDS. The phase meter houses trans-impedance amplifiers that convert photo currents to voltages. The photo diodes themselves are inside the vacuum system. Thus, the phase meter has to be located as close as possible to the vacuum system. With this configuration the existing trans-impedance amplifier design can be used without any changes and pick-up of stray signals is minimized. The phase meter output is piped via the EPP to a micro-controller based phase meter interface (Atmel

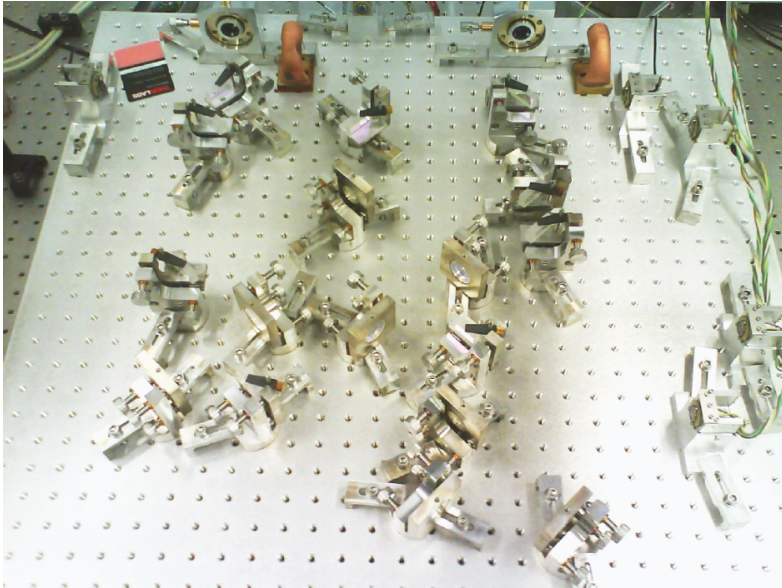


Figure 4.9.: A photograph of the test setup.

AT91SAM9260). This PMI collects the data, generates UDP¹ network packets and sends the data with a 2048 Hz update rate via an ethernet port to the CDS. Here, phase and amplitude are calculated; see Figure 4.8. Subsequently, the signals of all channels are combined, ending up with contrast, LDS, DPS, and DWS signals for the differential table motion. For more information on the PMI see [87].

4.8. Test setup

A small-scale version of the SPI was set up as a table-top experiment to gain familiarity with the technique of heterodyne Mach-Zehnder interferometry and to identify shortcomings of the complex interferometer design before finalizing the design of the bonded setup. Another idea of this test setup was to be able to start the measurement of the inter-table motion as soon as possible².

¹UDP is the abbreviation for user datagram protocol. It is a network communications method providing a set of network protocols for, *e.g.* the Internet.

²At the beginning of the AEI 10m prototype project a different, much simpler table design was foreseen such that the first two tables would have been installed about two years earlier, *i.e.* before the finalization of the bonded SPI setup. For this reason the test setup has been assembled on an aluminum breadboard using ultra-high vacuum compatible mounts; see Figure 4.9.

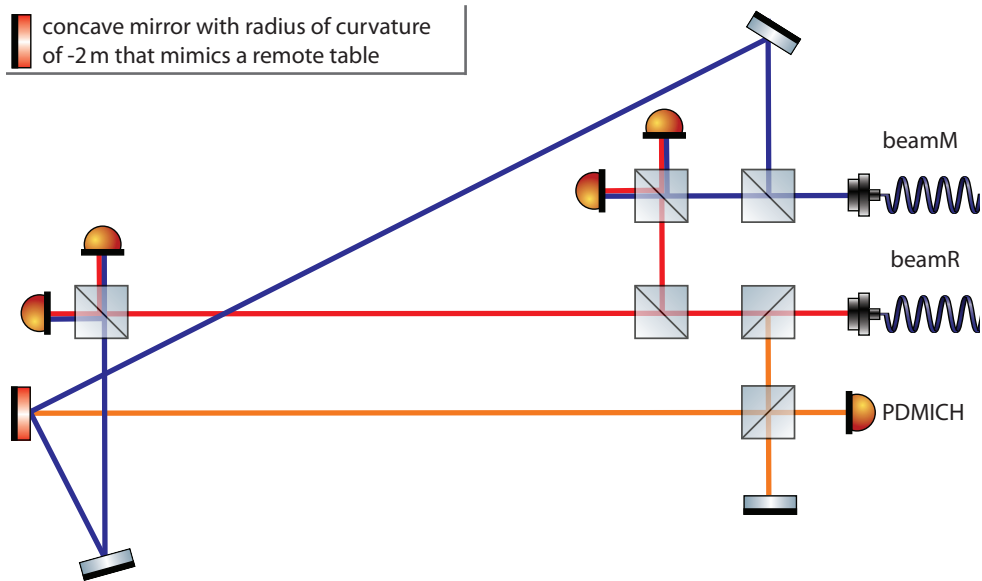


Figure 4.10.: Simplified optical layout of the test setup. Except for the curved mirror (red colored) all optics are placed on a breadboard. The distance between this breadboard and the curved mirror is about 1 m.

The layout of the test setup differs from that of the bonded SPI since the test setup was assembled before the finalization of the SPI design.

Figure 4.10 shows the optical layout of the test setup. The light which is injected by two fibers has been prepared on the same modulation bench as depicted in the lower left box of Figure 4.14 in on p. 43. The test setup consists of two Mach-Zehnder and one Michelson interferometers. One Mach-Zehnder interferometer serves as a reference; the other is the measurement interferometer. One mirror of the latter interferometer mimics a remote table which can be moved with respect to all the rest of the optics. The mirror has a curved surface (concave radius of curvature of -2 m) and is mounted in a piezo motor driven optical mount (AG-M100N by Agilis) which again is mounted onto a piezo motor driven linear stage (LS-25 by Agilis). In this way, the remote mirror can be moved in pitch, yaw, and longitudinal directions.

The Michelson interferometer can be used for an independent calibration of the piezo driven linear stages and mirror mounts. Quadrant photo diodes are placed at the output ports of all interferometers. Thus, it is possible to measure all possible motions of the remote mirror, which mimics the west table.

A heterodyne frequency of 1.6 kHz and an output data rate of 30 Hz were

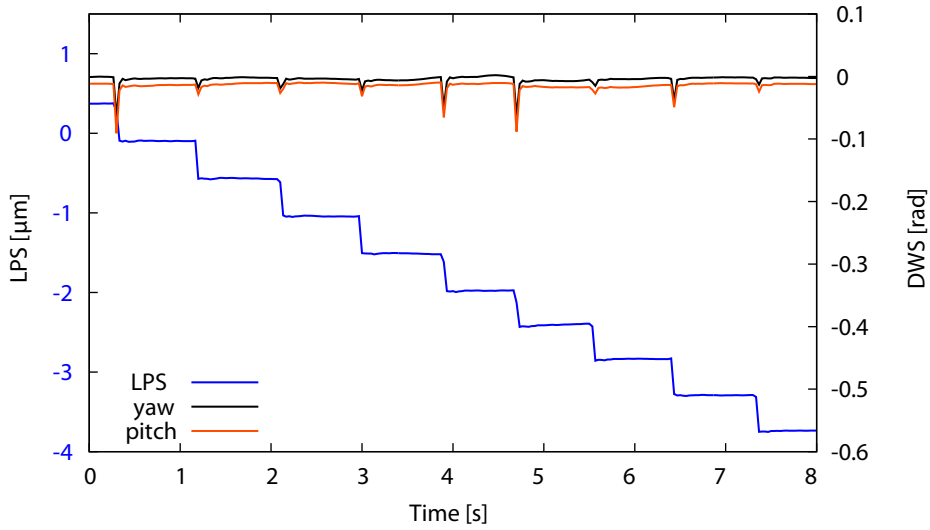


Figure 4.11.: Remote mirror shifted in the longitudinal degree of freedom.

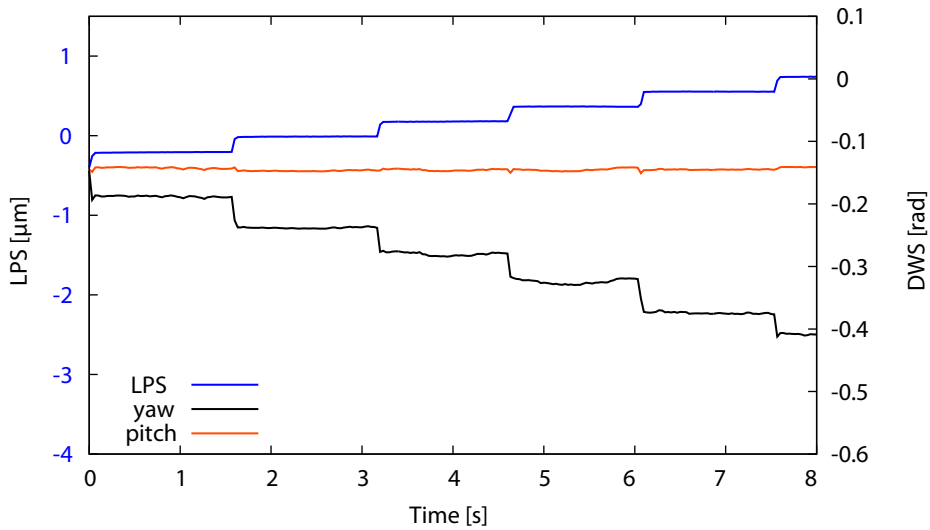


Figure 4.12.: Remote mirror rotated in yaw.

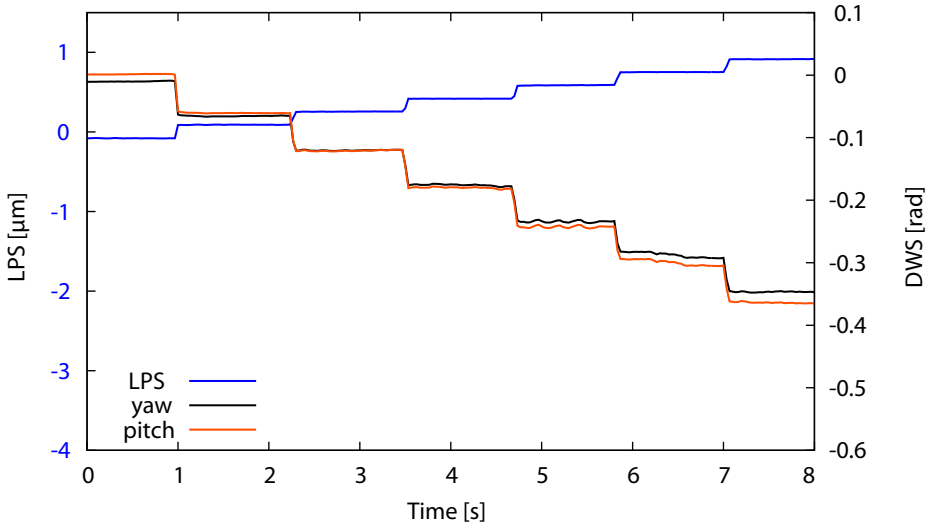


Figure 4.13.: Remote mirror rotated in pitch.

used in the test setup. The phase meter's EPP, without the phase meter interface, was used as the readout.

The aim of the measurements were to get an idea of coupling to the different readout channels, LPS signal for length and DWS signals for pitch and yaw. Since the optical layout of the test setup differs from that of the bonded SPI, these results only give qualitative information. All measurements were started with well-aligned interferometers. Figure 4.11 depicts the three different readout channels when longitudinal displacement was applied to the remote mirror. No coupling to the DWS channels was observed. For Figure 4.12 the remote mirror was moved in yaw, which couples not only to the DWS yaw, but also to the LPS channel, because the beam does not hit the mirror at its center of rotation. A displacement in pitch, see Figure 4.13, can be monitored in all three readout channels. Although some coupling can be observed, the three different motions can be easily distinguished which qualifies the technique of heterodyne Mach-Zehnder interferometry utilizing a curved remote mirror to be used for the SPI.

4.9. Optical layout of the SPI

The aforementioned considerations, in conjunction with simulations introduced in Chapter 5, p. 55, resulted in the optical layout of the SPI which

is shown in Figure 4.14. For completeness the results of this chapter are included in the description of the optical layout.

The SPI consists in total of four non-polarizing heterodyne Mach-Zehnder interferometers. All interferometers share the same optical path on the modulation bench, which is located outside of the vacuum system and shown in the lower left box of Figure 4.14.

The modulation bench houses a continuous-wave laser with a wavelength of $\lambda = 1064 \text{ nm}$ which is a commercially off-the-shelf iodine-stabilized Nd:YAG laser [84]. The laser light is split into two paths (at beam splitter BS in the lower left box of Figure 4.14). After that, each of the two beams is frequency-shifted by an AOM (Isomet 1205C-2) operating near 80 MHz, with a frequency difference between the two channels set to the desired heterodyne frequency of about 15 kHz.

The light (reference beam (beamR) and measurement beam (beamM) in Figure 4.14) is coupled into two 30 m long polarization-maintaining single-mode optical fibers. These are fed into the vacuum system, and the reference and measurement beams are delivered to fiber couplers mounted on the measurement bench. In contrast to the modulation bench which uses conventional optical mounts, the measurement bench is quasi-monolithic and thus much more stable in terms of mechanical and thermal drifts. All displacement measurements are performed on the measurement bench.

Measurement bench

The measurement bench is located on the central table (inside the vacuum system) and holds the mechanically and thermally ultra-stable part of the four interferometers. The measurement bench is made of Clearceram-Z HS, an ultra-low expansion material with a coefficient of thermal expansion of $(0.0 \pm 0.2) \cdot 10^{-7} \text{ K}^{-1}$ and a zero-crossing at room temperature [72], to ensure that thermal drifts are sufficiently small. The beam splitters and mirrors except MS and MW are hydroxy-catalysis bonded [74] to the 250 mm \times 250 mm surface of the 30 mm thick measurement bench. The remote mirrors MS and MW are bonded on two small blocks of Clearceram-Z HS of 35 mm \times 35 mm and 30 mm height.

Except for MS and MW, all mirrors and beam splitters are flat. In order to achieve a high interferometric contrast and a good sensitivity of the DWS signal, the radius of curvature of MS and MW has been chosen such that the waists of the two beams are at their recombining beam splitters (BR3, BR4). Thus, the beam radius and curvature of the beam's wave front is the same for both interfering beams. This leads to a high interferometric contrast. MS and

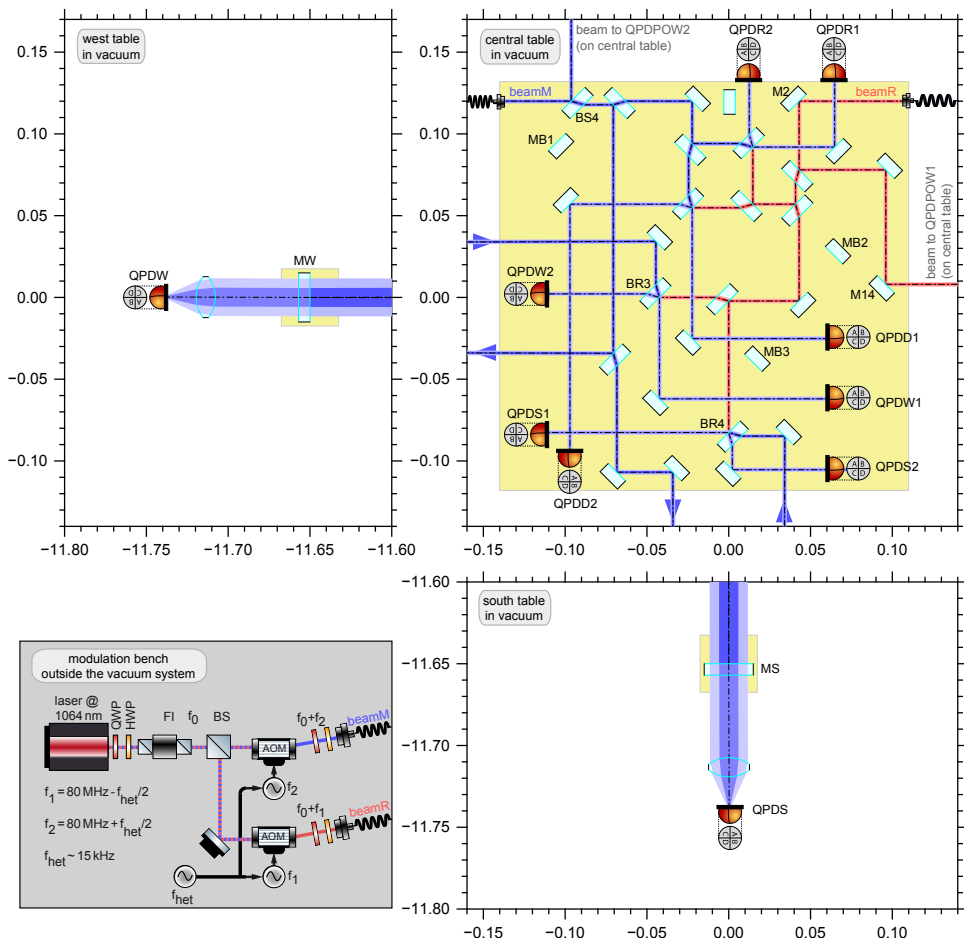


Figure 4.14.: The optical layout of the SPI. The lower left box shows the modulation bench on which the laser light is prepared and coupled into optical fibers. These fibers deliver the beams from the modulation bench to the measurement bench which is placed on the central table in the vacuum system (see upper right box). The reference beam (beamR) is drawn in red; the measurement beam (beamM) in blue. The reference beam is confined to the base plate on the central table, while parts of the measurement beam travel to the south and west tables.

All lengths are given in meters. $x = 0$ m, $y = 0$ m is the center of the central table; $x = -11.65$ m, $y = 0$ m is the center of the west table, and $x = 0$ m, $y = -11.65$ m is the center of the south table.

All quadrant photo diodes are labeled with QPD followed by another letter that indicates to which interferometer the photo diode belongs (D for diagnostic, R for reference, S for south, and W for west). BS = beam splitters, BR = beam recombiners, M = mirrors, FI = Faraday isolator.

Table 4.1.: Design arm length mismatch of the four interferometers.

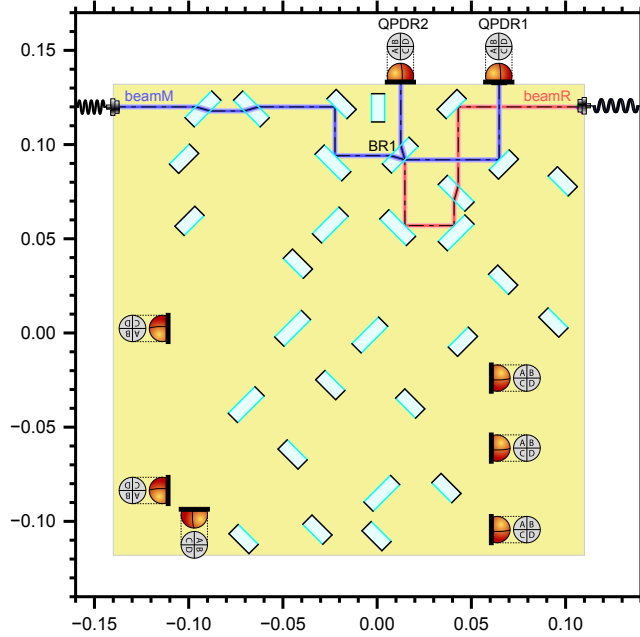
Interferometer	Reference	Diagnostic	South	West
Arm length mismatch [m]	0	0	23.165	23.165

MW have a concave radius of curvature of -11.8 m.

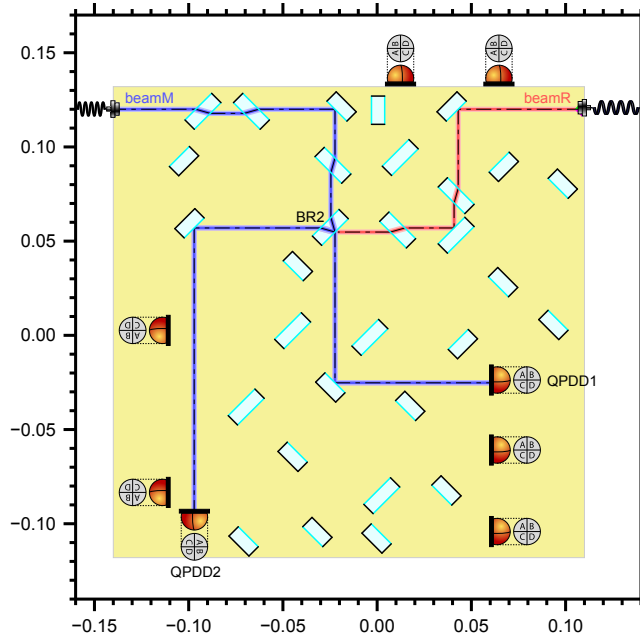
One of the four interferometers is the reference interferometer, see Figure 4.15a. It is used to cancel common mode fluctuations by measuring and subtracting them from all other interferometer outputs. The reference interferometer measures all path length equivalent fluctuations that have been picked up between the first beam splitter BS on the modulation bench and the recombining beam splitter BR1 on the measurement bench. Therefore, the reference and measurement beams are recombined at BR1 and their beat note is detected at photo diodes QPDR1 and QPDR2. Since all interferometers share the same optical paths between the modulation bench and beam splitter BSM and BSR (*cf.* Figure 4.15a) on the measurement bench, all interferometers are affected by the same phase noise. Path length equivalent fluctuations are caused by, *e.g.* drifts of the conventional mirror mounts on the modulation bench and by stress on the optical fibers. The optical fibers are flexible but need to be installed loosely so that they do not compromise the excellent seismic isolation of the optical tables.

The second interferometer, the diagnostic interferometer, is also entirely confined to the 250 mm×250 mm base plate, see Figure 7.2. The diagnostic interferometer, in conjunction with the reference interferometer, will be used for debugging purposes and to determine the sensitivity of the bonded setup since both nominally have the same signals. The diagnostic and reference interferometers are designed such that their optical arm length difference is zero, see Table 4.1. Within a Mach-Zehnder interferometer of equal arm length, laser frequency noise does not couple into the interferometric output signal. In this way, it is possible to determine, with an out-of-loop measurement, the limit to which the south and west tables can be stabilized relative to the central table. For the diagnostic interferometer, the reference and measurement beams are recombined at BR2 and detected at photo diodes QPDD1 and QPDD2.

The other two interferometers, namely the south and west interferometers (see Figure 4.15c-4.15d), measure the displacement of the south/west table

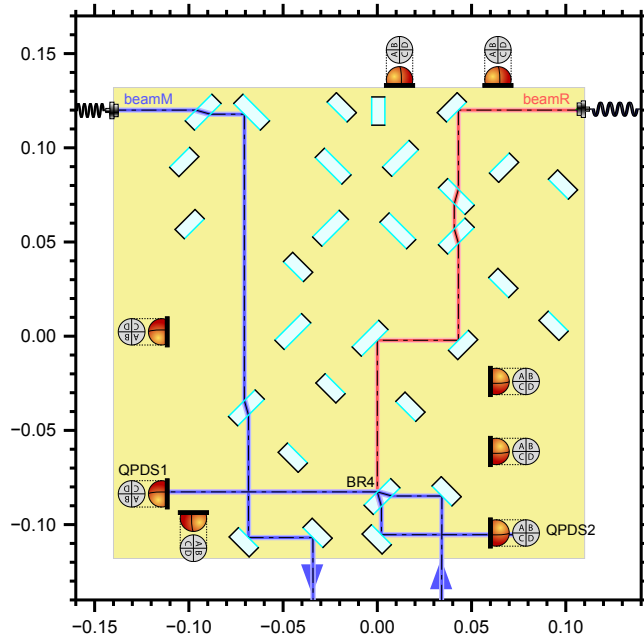


(a) Reference interferometer.

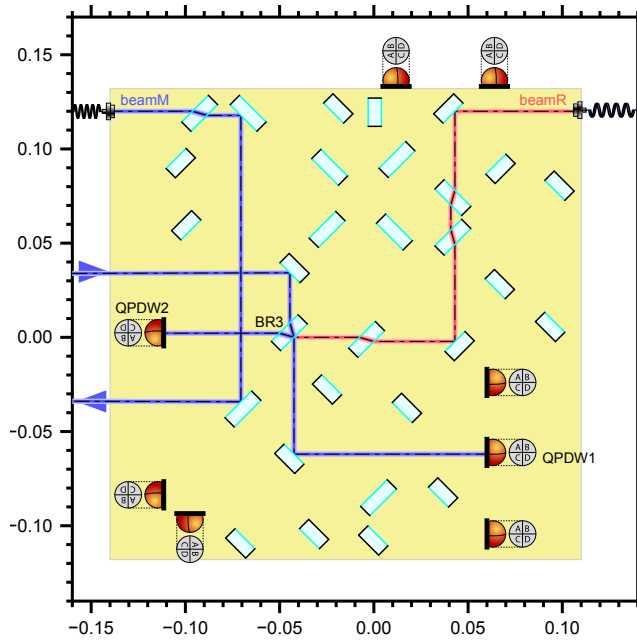


(b) Diagnostic interferometer.

Figure 4.15.: Each figure shows the optical beam paths from the fiber output coupler to the recombining beam splitter of the according interferometer.



(c) South interferometer.



(d) West interferometer.

Figure 4.15.

relative to the central table. They are the measurement interferometers, and have unequal arm lengths, see Table 4.1. One arm of each interferometer (the arm carrying the reference beam) is entirely on the central base plate. The other arm, the measurement beam, leaves the central base plate to a remote table. The measurement beam is reflected back to the measurement bench by the remote mirror.

The reference and measurement beams recombine at BR3 and BR4 for the west and south interferometers, respectively. The interference pattern of the west interferometer is detected by photo diodes QPDW1 and QPDW2, the beat note of the south interferometer at QPDS1 and QPDS2. A motion of the south/west table can be monitored by the south/west interferometer since the length of the interferometer arm carrying the measurement beam is changing while the south/west table and/or central table is moving, whereas the other arm carrying the reference beam is of constant length.

The beams reflected by beam splitter BS4 and mirror M14 (see Figure 4.14) are used for power stabilization and to monitor pointing noise of the fiber injectors. For further details on pointing noise of fiber injectors see Section 6.3, p. 82. The light being transmitted by MS and MW due to the residual transmission of the dielectric coating is detected by quadrant photo diodes. These are operated incoherently and are used to get additional information of the south and west tables' motion relative to the central table. All photo diodes used for the SPI are quadrant photo diodes QPD50-6 TO8S by First Sensor [88].

Substrates MB1, MB2, and MB3 (see Figure 4.14) are not part of any of the four interferometers. They were needed as references during the manufacturing process of the quasi-monolithic measurement bench. For more details on the bonding process and the accuracy achieved see Chapter 6, p. 73.

4.10. Input beam alignment

The reference and measurement beams must be aligned relative to each other such that they are parallel to the base plate and of the same height.

A section of the measurement bench depicting the beam alignment is shown in Figure 4.16. The most important optic is mirror MA. It has the same coating (HR coating for an angle of incidence of 45° at $\lambda = 1064 \text{ nm}$) as all other bonded mirrors. Thus some light is transmitted under normal incidence.

For the initial beam alignment mirror MA is bonded onto the base plate and the fiber couplers are connected to the plate, too. At this stage, only MA is bonded onto the base plate. The height of the beam is aligned to the desired

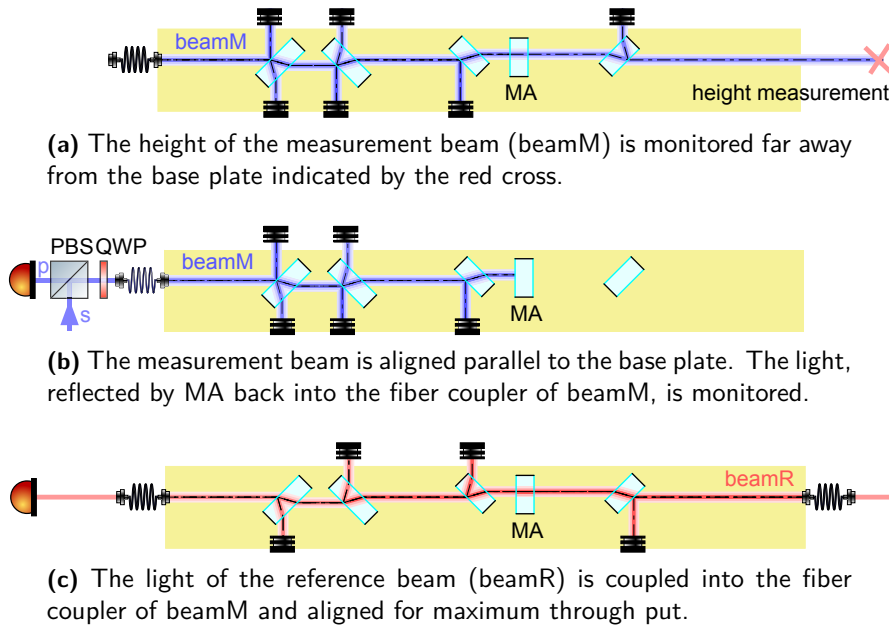


Figure 4.16.: Schematic of the alignment of the input beams relative to each other using a laser of a wavelength different from 1064 nm. The sketch depicts the upper part of the measurement bench shown in Figure 4.15.

value (measured at a distance far away from the base plate), as depicted in Figure 4.16a.

At the same time, some light is reflected by the front surface of MA. The measurement beam is parallel to the base plate when all of this light is coupled back into the fiber injector of the measurement beam, see Figure 4.16b. The measurement beam is parallel to the base plate when the detected power at the *p*-port of the polarizing beam splitter is at maximum. The alignment of parallelism and beam height is an iterative process and is limited by the perpendicularity of MA. The perpendicularity of MA is better than $90^{\circ}0'0'' \pm 0^{\circ}0'1''$ which corresponds to better than $5 \mu\text{rad}$.

Next, the reference beam (beamR) is coupled into the fiber of the measurement beam. The reference beam is at the right height and parallel to the base plate if the power measured at the output of the fiber of the measurement beam is at maximum.

When the other beam splitters and mirrors between the two fiber couplers have been bonded a realignment of the beams is still possible. A different laser wavelength must be used. The iodine-stabilized laser [84] used for the SPI offers a second laser wavelength of 532 nm generated by second-harmonic

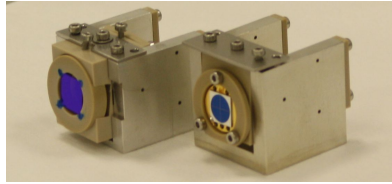


Figure 4.17.: A photograph of the QPD mounts used within the SPI. For both mounts the QPD is tilted by 8° upwards and can be aligned in height by M2 screws. The mount on the right hand side is used for dc position measurements on the remote tables. The mount on the left hand side is used at all interferometer outputs since it is equipped additionally with a rotatable and lockable thin film polarizer.

generation. The bonded mirrors become transmissive for this wavelength (75 % transmission). The optical components are oriented in such a way that the beam is not offset due to transmission.

4.11. Polarization control

When the reference and measurement beams of an interferometer are recombined only light of the same polarization contributes to the heterodyne beat note. Light of other polarization contributes only to the dc signal of the photodiode. A changing polarization of the laser beams results in a varying contrast and, behind a polarizing beam splitter, in laser amplitude noise. Such a change of polarization can be induced by mechanical or thermal stress on the fibers. The fibers of the SPI have a length of 30.5 m per arm. They each consist of three individual fibers connected via fiber-to-fiber couplers. Due to their length and routing they have a high exposure to environmental influences. Control of the polarization is required to minimize the aforementioned noise, and thus, ensure better sensitivity below a few tens of hertz [3, p.115], [89, p.55].

For polarization control of laser light four tools are used: polarization-maintaining optical fibers, wave-plates at the input of the fibers, polarizing beam splitters at the fiber outputs (see Chapter 6.3.2.3 on p. 90), and thin film polarizers in front of the interferometer QPDs.

The polarization-maintaining optical fiber is of PANDA type having a slow axis and a fast axis. The light is typically coupled into the slow axes, because of its higher robustness to external influences. Any linear polarized light which is guided off-axis has an elliptical polarization at the fiber output. With a polarimeter (SK9782-NIR by Schäfter & Kirchhoff) the extinction ratio at the

fiber output was measured. During these measurements the fiber length was changed by applying thermal and mechanical stress with cooling spray. The extinction ratio for both fibers was measured to be 16 dB.

It could be improved to 18 dB and 25 dB by matching the polarization axis of the light to the polarization-maintaining axis of the optical fiber by use of a wave-plate pair (QWP and HWP) in front of the fiber input. Behind the polarizing beam splitter located on the measurement bench the extinction ratio is 27 dB and 28 dB.

Residual p -polarized light is removed by placing thin film polarizers (color-Pol RVISIR CW02 by Codixx) in front of all interferometer photo diodes. A photograph of the photo diode with polarizer and mount is depicted in Figure 4.17. The thin film polarizer is rotatable and lockable. It has an extinction ratio of 1 to 10^6 . Within the mount the photo diode is tilted by 8° , so that any reflected light is directed upwards. This reduces stray light re-entering the interferometer.

4.12. Minimum contrast

Various noise sources, *e.g.* shot noise, electronic noise, *etc.*; contribute to the total noise of the interferometer which has to be below the aspired longitudinal path length noise of $100 \text{ pm}/\sqrt{\text{Hz}}$ at 10 mHz. The path length noise due to shot noise Δs_{shot} , electronic noise Δs_{el} , and relative power noise of the individual beams Δs_{pn} is proportional to $1/\sqrt{\eta_{\text{het}}}$ with η_{het} being the heterodyne efficiency of the interferometer. Thus, a minimum heterodyne efficiency exists which is necessary to measure below the SPI goal. It can be calculated using the equations presented in [90]

$$\Delta s_{\text{shot}} = \frac{\lambda}{2\pi} \sqrt{\frac{q_e(P_1 + P_2)}{\eta_{\text{PD}}\eta_{\text{het}}P_1P_2}} \quad (4.10)$$

$$\Delta s_{\text{el}} = \frac{\lambda}{\pi} \frac{n_{\text{el}}}{\eta_{\text{PD}}\sqrt{\eta_{\text{het}}P_1P_2}} \quad (4.11)$$

$$\Delta s_{\text{pn}} = \frac{\lambda}{2\pi} \frac{n_{\text{pn},1}P_1 + n_{\text{pn},2}P_2}{\sqrt{2\eta_{\text{het}}P_1P_2}} \quad (4.12)$$

Table 4.2 lists all variables and constants used in the equations. Further noise sources contribute to the total path length noise, namely path length noise due to laser frequency noise Δs_{freq} , thermo-optical noise within fused silicate Δs_{fs} , and thermo-elastic noise of Clearceram-Z HS Δs_{c}

Table 4.2.: Quantities for minimum contrast calculation. A star (*) remarks a measured value. The † remarks an approximated value which is three order of magnitudes larger than the electronic noise per photo diode segment for testing the LISA optical bench [90].

Quantity	Symbol	Value	Unit
Speed of light [91]	c	299792458	m/s
Thermo-optic coeff. of fused silica [73]	$\frac{dn_{fs}}{dT}$	$9.6 \cdot 10^{-6}$	1/K
Electronic noise per QPD segment†	n_{el}	$3.5 \cdot 10^{-9}$	A/ $\sqrt{\text{Hz}}$
Refractive index of fused silica [73]	n_{fs}	1.44963	1
Relative power noise of beam 1*	$n_{pn,1}$	0.0044	1/ $\sqrt{\text{Hz}}$
Relative power noise of beam 2*	$n_{pn,2}$	0.0147	1/ $\sqrt{\text{Hz}}$
Power of beam 1*	P_1	$8.8 \cdot 10^{-4}$	W
Power of beam 2*	P_2	$9.5 \cdot 10^{-4}$	W
Elementary charge [91]	q_e	$1.602 \cdot 10^{-19}$	As
CTE of Clearceram-Z HS [72]	α_c	$2 \cdot 10^{-8}$	1/K
CTE of fused silica [73]	α_{fs}	$5.1 \cdot 10^{-7}$	1/K
Laser frequency noise (<i>cf.</i> Figure 4.7)	Δf	$2 \cdot 10^2$	Hz/ $\sqrt{\text{Hz}}$
Optical path length difference	ΔL	0.1	m
Temperature noise [92]	ΔT	$1 \cdot 10^{-4}$	K/ $\sqrt{\text{Hz}}$
Photo diode efficiency [88]	η_{PD}	$2.3 \cdot 10^{-1}$	1
Laser wavelength [84]	λ	1064	nm

$$\Delta s_{\text{freq}} = \frac{\lambda}{c} |\Delta L| \Delta f \quad (4.13)$$

$$\Delta s_{fs} = \left| \Delta T \Delta L \left[\alpha_{fs} (n_{fs} - 1) + \frac{dn_{fs}}{dT} \right] \right| \quad (4.14)$$

$$\Delta s_c = |\Delta T \Delta L \alpha_c| \quad (4.15)$$

The total path length noise, Δs , of an interferometer is given by [90]

$$\Delta s = \sqrt{\Delta s_{\text{shot}}^2 + \Delta s_{el}^2 + \Delta s_{pn}^2 + \Delta s_{fs}^2 + \Delta s_c^2 + \Delta s_{\text{freq}}^2} \quad (4.16)$$

With Equations 4.11 to 4.16 the minimum heterodyne efficiency necessary to realize a path length noise below 100 pm/ $\sqrt{\text{Hz}}$ at 10 mHz was calculated. Even with a heterodyne efficiency of 1 this is not possible due to the high

relative power noise of the measured beams. In [92, p. 41] the relative intensity noise of an iodine-stabilized laser was stabilized to $3 \cdot 10^{-5} / \sqrt{\text{Hz}}$ at 10 mHz (out of loop measurement). For the in loop measurement $1.5 \cdot 10^{-6} / \sqrt{\text{Hz}}$ was detected at 10 mHz. Hence, an intensity noise of $3 \cdot 10^{-5} / \sqrt{\text{Hz}}$ was assumed for the calculation. With these values a heterodyne efficiency of 0.092 % is required to be able to sense $100 \text{ pm} / \sqrt{\text{Hz}}$. Using Equation 3.17 on p. 23 this can be converted to a contrast of 9.6 %.

4.13. Conclusion

Two measurement interferometers, each sensing the relative motion between the central table and one remote table, have been designed. This ensures that the SPI can be operated between two tables if needed. In order to minimize the complexity of control of the inter-table motion, the interferometers are designed to be as identical as possible. On all tables the optics of the SPI are located at (or close to) the table's central axis in order to minimize cross-coupling from rotational motion to longitudinal displacement. Curved mirrors on the remote tables are used to guarantee that the beam parameters of the measurement beam at the beam recombiner are the same as those of the reference beam, whose optical path is about 23 m shorter. First experiments using a test setup have shown that this approach is suitable to measure and distinguish longitudinal displacement, pitch, and yaw motions from each other. Additionally, two more interferometers, with no arm length mismatch, located only on the central table have been incorporated in the layout, to be used as reference and diagnostic tools.

The optics are bonded onto an ultra-low expansion base plate made of Clearceram-Z HS and a footprint of $250 \text{ mm} \times 250 \text{ mm}$ to enhance the mechanical and thermal stability of the SPI. This assures low maintenance, low mass of about 5 kg, and compatibility with ultra-high vacuum.

CHAPTER 5

Simulations

In this chapter the expected interferometer signals for the nominal setup of the SPI are presented. The dependency of the interferometer signals on misalignment of the two beams with respect to each other is investigated. From this study the coupling factors are computed. They are a measure how strong a beam misalignment of one degree of freedom couples into the various interferometer signals. The range of beam misalignment within which these coupling factors are valid is presented. The impact of the radius of curvature of the remote mirrors on the interferometer signals is investigated. Finally, the question is addressed whether a change of the installation order of the tables alters the interferometer signals of the SPI.

All these simulations were originally computed with the simulation tools `Optocad` [93] and `QPD.c` resulting in the nominal optical setup presented in Figure 4.14 on p. 45. At a later stage the results of these simulations were verified by the software tool `Ifocad` [94] which has been developed in the meantime. Whenever necessary, *e.g.* for the calculation of the signal range, the full nominal in-vacuum setup presented in Figure 4.14 on p. 45 was used for the simulations. For some calculations this was not necessary and a simplified setup (see Figure 5.1) was used, *e.g.* for simulations on the impact of the radius of curvature of the remote mirrors. The `Optocad` code of both setups can be found in Appendix A, p. 123. It includes the position of the optics as well as properties of the beams. The lengths of the various interferometer arms are displayed in Table A.1 on p. 127.

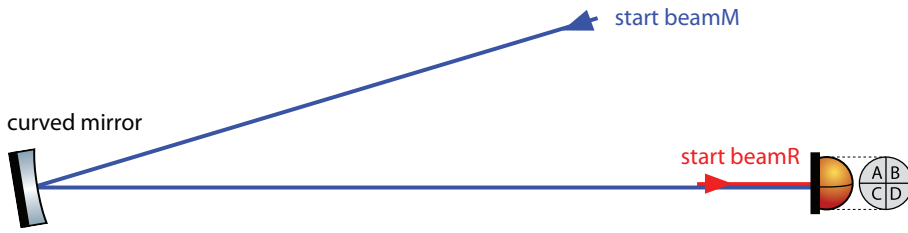


Figure 5.1.: Simplified optical setup used for simulations.

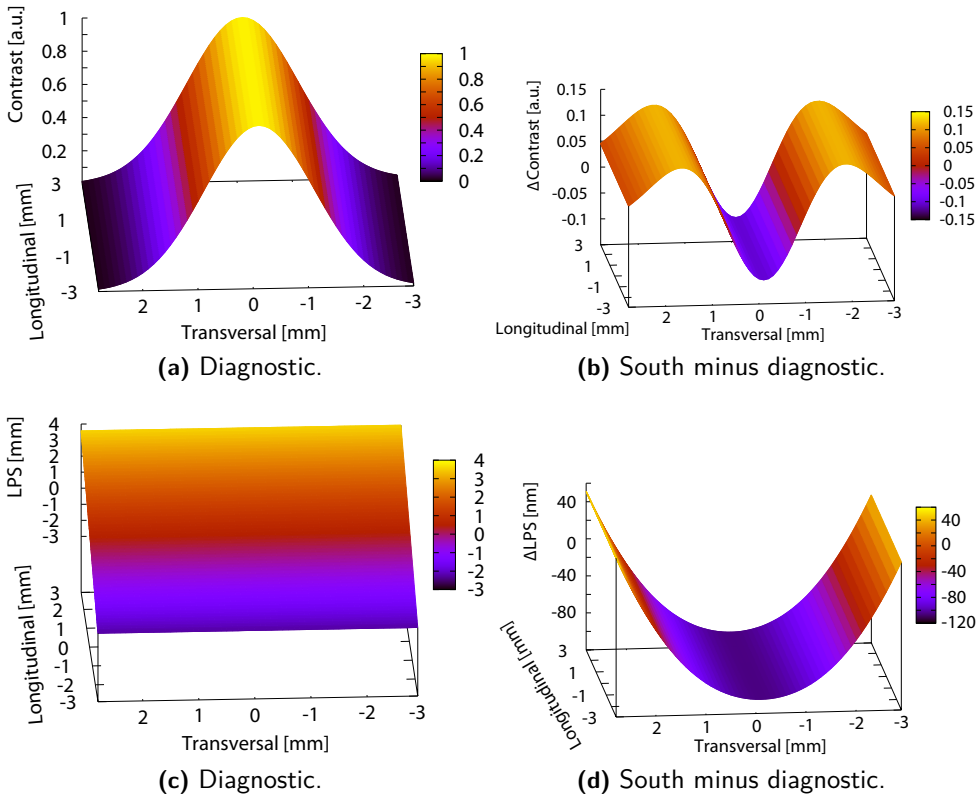


Figure 5.2.: Dependency of contrast [(a)–(b)] and, LPS signal [(c)–(d)] on the beam displacement in the horizontal plane. The first column shows the results for the diagnostic interferometer, the second column the difference of south interferometer and diagnostic interferometer. For the calculation of these graphs the measured beam parameters at the position of the photo diodes have been used.

5.1. Signal dependency on interferometer alignment

Interferometric signals depend on the alignment of the interferometer beams, their parameters, and power. The beam parameters of the SPI were designed to be able to realize an interferometric contrast of above 0.99; see Section 4.5 on p. 32. However, the actual beam parameters differ from their nominal values. Hence, during the alignment and assembly of the interferometers, the maximum possible contrast with the actual beam parameters for perfect beam alignment is worth knowing. Furthermore, it is of interest how misalignments of the beams change the output signals of the interferometer.

For this purpose the dependency of contrast, LPS signal, and DWS signal on the beam displacement in the horizontal plane was computed using the measured beam parameters (see Table 6.1 on p. 85 and Table 6.2 on p. 96), the according distances to the photo diodes, and identical beam powers. The simulation setup consisted only of the two beams and a photo diode. For all simulations the measurement beam remained well-aligned on the photo diode. For the first part of the simulations, the reference beam was displaced longitudinally and laterally, and the according interferometer signals were calculated. In the second part, the reference beam was misaligned in the transversal and yaw degree of freedom.

5.1.1. Misalignment in xy -direction

For the study of the misalignment in xy -direction, the reference beam was shifted in transversal and longitudinal direction relative to the measurement beam which remained well-aligned on the photo diode. The results are depicted in Figure 5.2. The first column of this figure shows the signals for the diagnostic interferometer which is an identical copy of the reference interferometer. The second column shows the difference between south and diagnostic interferometers. The representation of the south interferometer has been omitted, since from the figures no differences are observed between both interferometers.

Figure 5.2a and 5.2b show that as expected the interferometric contrast does not depend on the longitudinal beam alignment, but on the transversal beam displacement. Here a Gaussian dependency is observed. For an ideal alignment of the diagnostic interferometer a contrast of 0.99 is possible. For the south interferometer this number is reduced, only 0.88 are possible; see Figure 5.2b. The reason for this are the different beam parameters of the two beams, since measured beam parameters were used for this computation. For two perfectly aligned beams of equal power the contrast, c , depends on the

Rayleigh range, z_0 , and distance z between the position of the waist and the place of interference [95]

$$c = \frac{2\sqrt{z_{0,1} \cdot z_{0,2}}}{\sqrt{(z_1 - z_2)^2 + (z_{0,1} + z_{0,2})^2}} \quad (5.1)$$

Using this equation and the measured beam parameters (beam 1 being the reference beam and beam 2 being the measurement beam) the same contrast is calculated using the beam parameters shown in Table 6.1 and 6.2 (on p. 85 and 96) and the arm length of the interferometer; see Table A.1 on p. 127

$$c = \frac{2\sqrt{3.137 \text{ m} \cdot 4.124 \text{ m}}}{\sqrt{(0.03452 \text{ m} - 3.768 \text{ m})^2 + (3.137 \text{ m} + 4.124 \text{ m})^2}} = 0.88 \quad (5.2)$$

This analytic calculation confirms the numerical simulation result that with the existing beam parameters no contrast better than 0.88 can be realized.

Moreover, Figure 5.2b shows that for transversal displacements larger than ± 1 mm the contrast of the south interferometer is higher than of the diagnostic interferometer. So, the full width at half maximum of the contrast is wider for the south interferometer, because of the broader Gaussian profile of the measurement beam within the south interferometer.

The LPS signal for the diagnostic interferometer shows the expected behavior. A longitudinal shift of the reference beam couples 1:1 in a change of the LPS signal; see Figure 5.2c. Note that the constant offset has been subtracted from the LPS signal in this figure, such that the LPS signal for the unequal arm interferometer is zero in the well-aligned case. A misalignment in the transversal direction does not couple into the LPS signal. This is different for the south interferometer. Here transversal displacement contributes to the LPS signal. Again, the reason are the differently curved wavefronts of the two beams in the south interferometer. An intuitive explanation is given in Figure 5.3b. When both beams, the gray colored reference beam and the orange colored measurement beam, are well-aligned the LPS signal is zero. When the reference beam is laterally shifted, the LPS signal differs from zero. The change in the LPS signal follows the radius of the wavefront curvature of the gray colored beam. Therefore, the difference of the LPS signal of the south and diagnostic interferometer has this curved shape as depicted in Figure 5.3b. For comparison, Figure 5.3a shows two identically curved wavefronts: once aligned (again depicted in gray and orange) and transversally shifted (depicted in gray and blue) by the same amount as in Figure (b). Here no difference in the LPS signal can be observed. For a transversal displacement of $100 \mu\text{m}$ a change

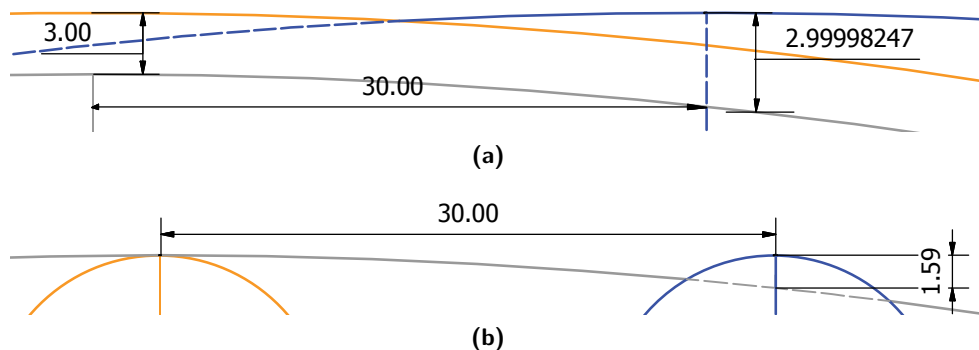


Figure 5.3.: Illustration of the LPS signal for aligned beams and beams which are laterally shifted with respect to each other. The gray colored beam is the beam with constant position. The orange colored beam has no lateral shift with respect to the gray colored beam. The blue colored beam is shifted by 30 (in arbitrary units). Figure (a) shows that for beams with identical radii of curvature, the LPS signal does not depend on the lateral shift of the beams relative to each other. In Figure (b) the two beams have differently curved wavefronts. Here, a transversal displacement results in a change of the LPS signal which changes with the radius of curvature of the constant, gray colored beams.

in the LPS signal of 147 pm is computed. For longitudinal misalignment the south and diagnostic interferometers show the same behavior.

5.1.2. Misalignment in the transversal and yaw degree of freedom

Next, the dependency of the interferometer signals on the beam misalignment in yaw and the transversal degrees of freedom are investigated. For this computation, the reference beam is rotated around its starting point.

Figure 5.4a shows that the interferometric contrast strongly depends on the angular misalignment. A beam rotated in yaw by 0.5 mrad in an otherwise well-aligned diagnostic interferometer results in a contrast of about 33%. However, the interferometric contrast is not concentric around the best aligned configuration. It is elliptic due to the different dependency on transversal and yaw alignment. This ellipse is rotated for the south interferometer; see Figure 5.4b. The reason for this is the differently curved wavefronts of the measurement beams in both interferometers, *cf.* see Table 6.1 on p. 85, Table 6.2 on p. 96, and Figure 6.15 on p. 98.

Both, transversal beam displacement and angular misalignment result to some extent in a variation of the LPS signal; see Figure 5.4c. Figure 5.5a shows in gray the measurement beam which remains at constant position and

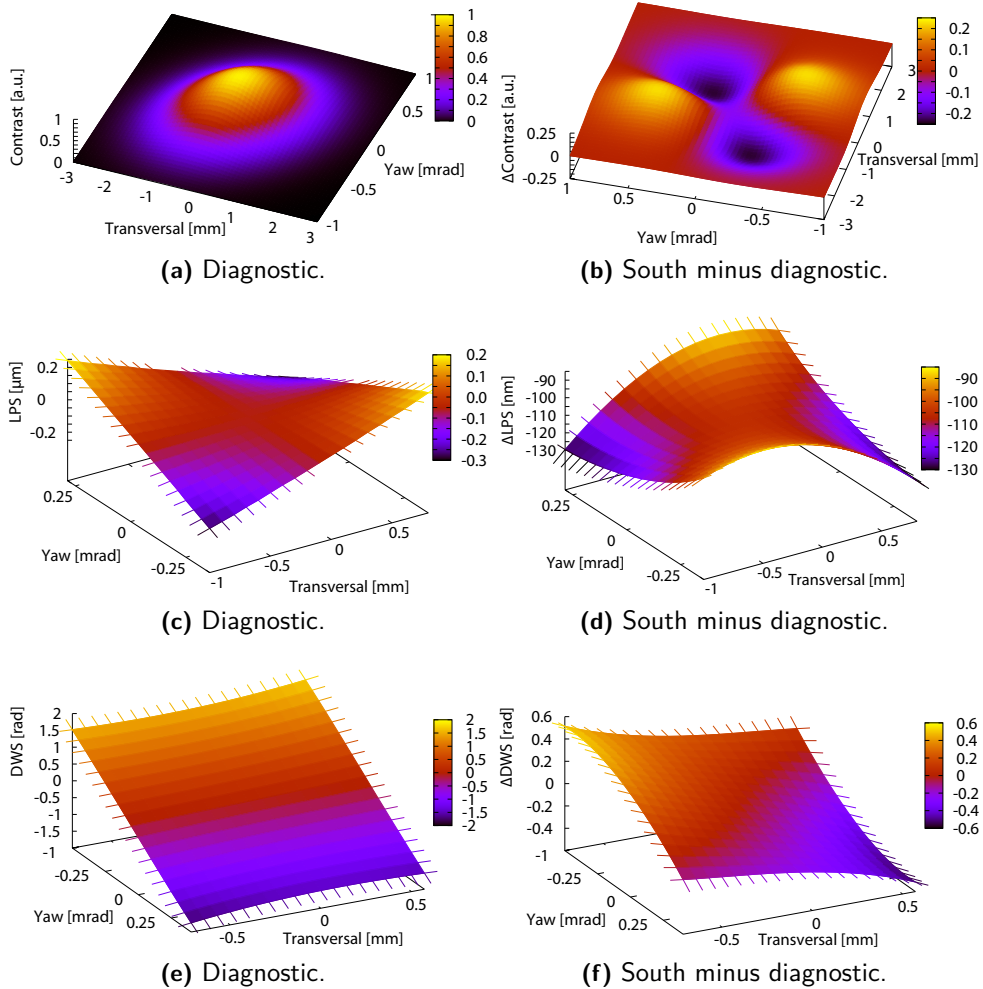


Figure 5.4.: Dependency of contrast [(a)–(b)], LPS signal [(c)–(d)], and DWS signal [(e)–(f)] on the beam misalignment in the transversal and yaw degree of freedom. The first column shows the results for the diagnostic interferometer, the second column the differential signal of south interferometer and diagnostic interferometer. For the calculation of these graphs the measured beam parameters at the position of the photo diodes have been used.

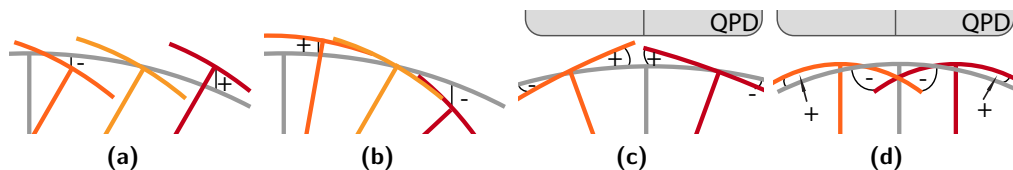


Figure 5.5.: The sketches show how a transversally displaced and/or tilted beam couples into the LPS signal [see (a)–(b)] and DWS signal [see (c), (d)]. The gray colored wavefront depicts the measurement beam which remains well-aligned onto the photo diode. The yellow, orange, and red colored wavefront refers to the reference beam for different misalignments.

angle for this consideration. The yellow colored reference beam is tilted with respect to the gray colored measurement beam. When this reference is laterally shifted to the right, see red colored beam in the same figure, the LPS signal is increased compared to the situation before (denoted by the plus sign). If the yellow beam is shifted in the opposite direction the LPS signal is decreased. Figure 5.5b illustrates again in gray the measurement beam being of constant position. In yellow, the reference beam is tilted by some amount. If the tilt angle is increased (the yellow colored beam is now at the position of the red colored beam), the LPS signal between the measurement and reference beams declines. When the tilt angle is minimized, the LPS signal rises. This explains the shape of the LPS signal for the diagnostic interferometer. The general shape is the same for the south interferometer; see Figure 5.4d, but the different curvatures of the wavefronts of the measurement beams of both interferometers result in different absolute numbers.

Figure 5.4e depicts the dependency of the DWS signal from the beam alignment for the diagnostic interferometer. An angular change between the two beams results in a different DWS signal whose sign indicates the direction of the angular misalignment. Figure 5.5c depicts this. First, let's assume the case of the gray colored reference beam and the red colored measurement beam. Over the entire surface of the left quadrants of the QPD, the red beams is ahead of the gray beam, resulting in a large positive phase signal. On the right quadrants of the QPD, at some positions the red colored beam arrives before the gray beam, at other positions it is *vice versa*. Thus, the phase difference between the two beams on the right segments is smaller than on the left segments. The opposite is detected in case of the orange and gray colored beams. Hence, a different tilt between two beams results in a different DWS signal with its sign indicating the direction of beam rotation. A transversal beam displacement results in a much smaller change of the DWS signal than

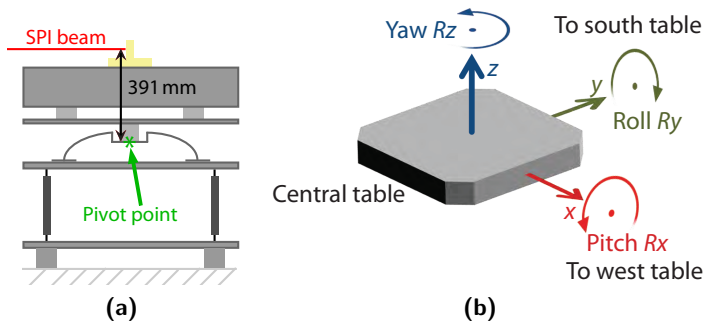


Figure 5.6.: (a) Simplified sketch of the table with the SPI on it. The table's pivot point is 391 mm below the beam axis of the SPI. (b) Coordinate system between the three tables.

a beam tilt. This is illustrated in Figure 5.5d.

The DWS signal of the south interferometer has a stronger dependency on beam displacement and misalignment in yaw; see Figure 5.4f. This is again due to its non-identical beam parameters.

So far, it was investigated how interferometer signals change for different relative beam alignments. Simple illustrations for the understanding of cross-coupling between the different degrees of freedom were presented. In the following the quantity of this cross-coupling is analyzed.

5.1.3. Coupling factors

The investigation of the interferometer signals due to misalignment of the measurement beam with respect to the reference beam is of interest as the remote mirrors of the SPI's south and west interferometers will move relative to the optics located on the central table induced by the residual motion between the tables. For an usage of the interferometers signals in a control loop to stabilize the relative inter-table motion, it is beneficial that the signals of the various degrees of freedom are well decoupled. This means that one signal monitors only the motion of one degree of freedom. Also the shape of them, *i.e.* linear, quadratic, *etc.*; matters. A linear signal with a zero-crossing at the nominal position is best suitable for control loop design. Linear coupling factors (here simply referred to as coupling factor) quantify this coupling. They are computed numerically using the equation [71, p.82]

$$k_{\text{dof}}^{\text{signal}} := \frac{\Delta \text{signal}}{\Delta \text{dof}} = \frac{\text{signal}(\text{dof}) - \text{signal}(\text{dof} + \epsilon)}{\epsilon} \quad (5.3)$$

In simple words a coupling factor is the slope of a signal over a degree of freedom (dof) for a small deviation from the nominal value.

For a correct determination of the coupling factors the position of the pivot point of the remote table with respect to the point of reflection on the remote mirror has to be known. In the vertical direction the pivot point of the table is about 391 mm below the beam axis of the SPI; see Figure 5.6a. This number is taken from the CAD drawings of the tables and the SPI. In the horizontal plane the rotation point should ideally be at the intersection of the diagonals of the square table. However, if the table is not well leveled the pivot point is off-centered. A leveling of the table is necessary any time some mass has been added, removed or shifted on the table. Typically the initial leveling is done by use of a machine spirit level with an accuracy of about 0.05 mm per m. Fine alignment is possible by usage of the LVDTs. When the SPI is in operation its interferometer signals can also be used for table alignment. The horizontal position of the pivot point will change anytime mass has been added, removed or shifted on the table. The offset in x and y of the pivot point can be calculated by use of this equation [48, p.151].

$$\begin{pmatrix} x \\ y \\ Rz \end{pmatrix} = \frac{1}{3} \begin{pmatrix} -2 & 1 & 1 \\ 0 & \sqrt{3} & -\sqrt{3} \\ 1/R & 1/R & 1/R \end{pmatrix} \begin{pmatrix} H1 \\ H2 \\ H3 \end{pmatrix} \quad (5.4)$$

Figure 5.6b depicts the used coordinate system. $H1$ to $H3$ are the signals of the horizontal LVDT sensors which are located equally distributed on a circle with radius R from the table center; see Section 2.2 on p. 12. R is 787 mm [48, p.107]. The horizontal LVDTs sense the displacement between spring box and ground. The values for $H1$ to $H3$ were measured for a well-aligned south interferometer set up on two well leveled tables resulting in an offset of the pivot point with respect to the intersection of the diagonals of the table in the horizontal plane of

$$\begin{pmatrix} x \\ y \\ Rz \end{pmatrix} = \begin{pmatrix} -1.098 \text{ mm} \\ +1.921 \text{ mm} \\ -0.694 \text{ mrad} \end{pmatrix} \quad (5.5)$$

The pivot point of the table is located 391 mm below the beam axis. It is -1.098 mm off-centered in the x and 1.921 mm in the y directions. The coupling factors for this configuration were computed. Table 5.1 shows the results and Table 5.2 shows the range within which these coupling factors are valid. This means, the range within the linear fit to the interferometer signal was within the errors of 1 %.

Table 5.1.: Coupling factors of south table motion to the south interferometer. The pivot point of the remote table is 391 mm below the beam axis of the SPI and -1.098 mm off-centered in x and 1.921 mm in y -direction. Figure 5.6b depicts the according coordinate system. Values with a star (*) are no linear coupling factors, but quadratic ones.

	LPS	DWS _h	DWS _v	DPS _h	DPS _v
	[mm/mm]	[mrad/mm]	[mrad/mm]	[a.u./mm]	[a.u./mm]
x	-6.032e-07	-596.105	0	1.418	0
y	-1.99986	-2.508	0	5.84e-05	0
z	-6.032e-07	*3.390e-05	-554.181	*3.840e-7	1.419
	[mm/mrad]	[mrad/mrad]	[mrad/mrad]	[a.u./mrad]	[a.u./mrad]
Rx	-0.782	-0.975	6616	0	17
Rz	-0.004	-6618	0	17	0

The results of Table 5.1 can be understood in three steps: first, the outcome for the various translational degrees of freedom is investigated, second a comparison with signals for an angular misalignment is done, and third the findings for the angular and translational degrees of freedom are compared.

First, the coupling factor to the LPS signal is maximum for a longitudinal change (y) of the inter-table distance. The coupling factors to horizontal changes (denoted by the subscript h), *i.e.* DWS_h, DPS_h, have the highest value for a lateral shift (x) of a table. The DWS and DPS signals of the vertical direction are biggest for a shift of a table in height (z). Thus, displacements in the three translational degrees of freedom can be well distinguished from each other.

Second, an angular table misalignment in pitch couples strongly to the vertical DWS and DPS signals whereas a table motion in yaw couples to the horizontal interferometer signals enabling a distinction of angular misalignment.

Third, the results for the rotational and translational degrees of freedom are compared with each other starting with the LPS signal. For this purpose, the calculated coupling factors are multiplied with the according amplitude spectral density of a damped table (in x , z , Rx , and Rz direction) to quantify the impact of coupling when the inter-table motion is not stabilized. In this way it is possible to express the effect of rotation to the LPS signal in terms of $m/\sqrt{\text{Hz}}$. For this purpose the table displacement due to seismic noise was measured with three horizontal and three vertical LVDTs in the various degrees

Table 5.2.: Range in which the signal response of the interferometers is linear to misalignment of the remote tables.

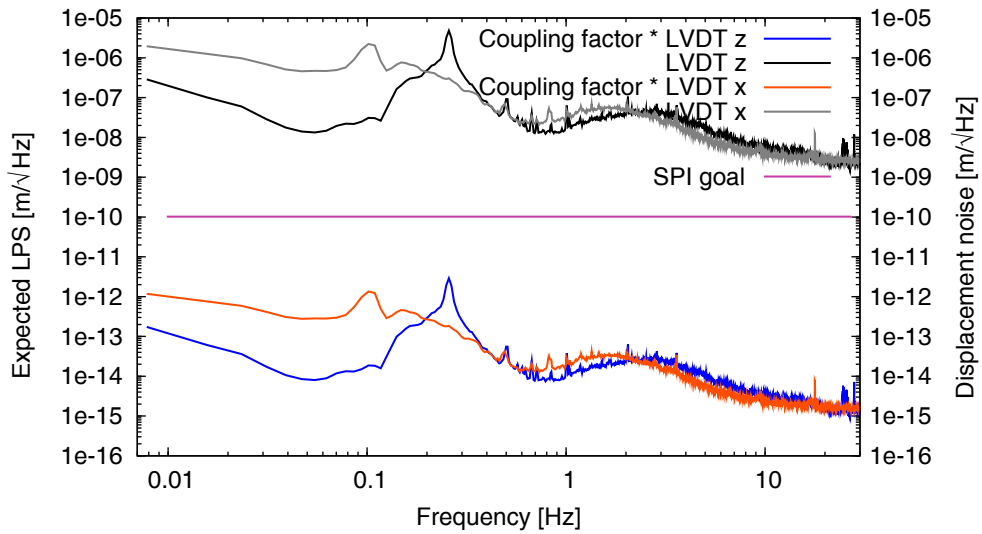
	LPS	DWS _h	DWS _v	DPS _h	DPS _v
	[mm]	[mm]	[mm]	[mm]	[mm]
x	0.03	0.39	–	0.20	–
y	100	100	–	8	–
z	0.024	–	0.15	–	0.18
	[μ rad]	[μ rad]	[μ rad]	[μ rad]	[μ rad]
Rx	–	–	23.5	–	15.5
Rz	–	17.0	–	15.5	–

of freedom. The measurement results are the gray and black colored graphs in Figure 5.7.

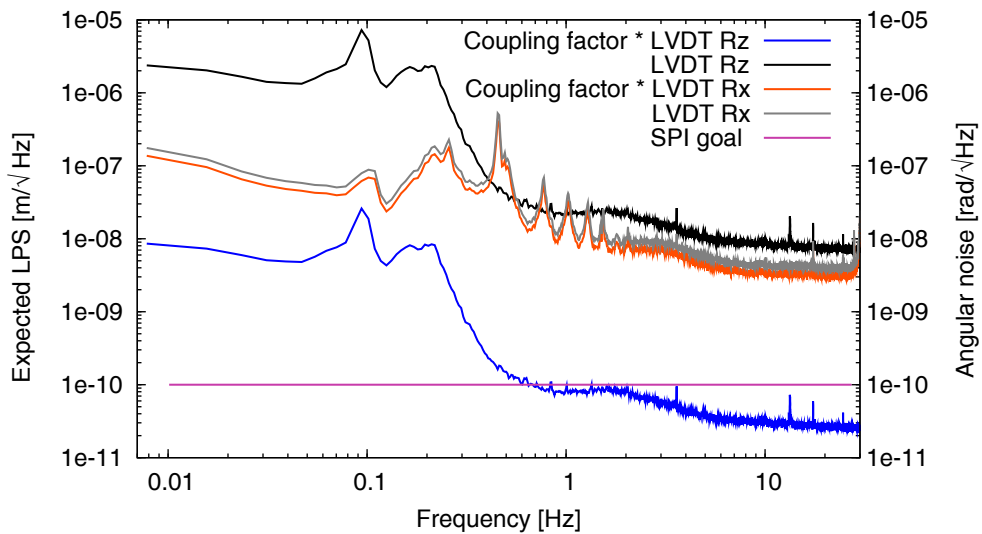
The expected LPS signal due to lateral displacement and shift in height is shown in the orange and blue lines in Figure 5.7a. This coupling is well below the SPI design goal (*cf.* Figure 1.2 on p. 4) for all frequencies of interest and will not limit the performance of the SPI.

This is different for the coupling from the table’s rotational motion to the LPS signal; see Figure 5.7b. The yaw motion is smaller than $100 \text{ pm}/\sqrt{\text{Hz}}$ for frequencies above 0.7 Hz. The pitch motion couples stronger into the LPS signal than the yaw motion. It is at least one order of magnitude above the design goal of the SPI for all frequencies of interest. This means, that the table’s rotational degrees of freedom have to be stabilized to be able to measure and stabilize a longitudinal inter-table motion of $100 \text{ pm}/\sqrt{\text{Hz}}$ for frequencies above 10 mHz. However, the actual measurement might differ from this result, because the pivot point of the table might be at a slightly different position by a few millimeters. Nevertheless, the coupling especially from the table’s pitch motion to the longitudinal path length signal needs to be taken into consideration when the measurement and stabilization of the longitudinal inter-table motion is limited.

The amplitude spectral densities in Figure 5.7 are also used to characterize whether the rotational or translational degree of freedom couples stronger to the DWS and DPS channels. For both signals and directions (vertical and horizontal), an angular table misalignment couples four times stronger than a shift in a translational degree of freedom. Hence, a distinction of the longitudinal and angular table misalignment is possible. A lateral change of a table can be monitored with a quadrant photo diode on the remote table(s).



(a) Translational degrees of freedom.



(b) Rotational degrees of freedom.

Figure 5.7.: The black and gray colored line show the table motion (displacement, pitch, and yaw) of the south table measured with the LVDTs. These spectra were multiplied with the coupling factor resulting in the expected path length noise (orange and blue colored curves). For Figure (a) the coupling factors from Table 5.1 were used, for Figure (b) the one of Table 5.1.

Table 5.3.: Heterodyne signal range of the remote interferometers when the remote table is shifted in one degree of freedom with respect to the central table while all other degrees of freedom remain constant. The first line states from which value on a heterodyne signal becomes available. The second and third lines show within which range a interferometric contrast larger than 50 % and 80 % can be monitored.

Contrast	Δx [mm]	Δy [m]	Δz [mm]	ΔRx [μ rad]	ΔRz [μ rad]
1 %	1.60	2.19	1.60	134.5	90.8
50 %	0.43	0.87	0.61	51.0	34.9
80 %	0.33	0.47	0.34	27.5	19.2

5.2. Signal range

The task of the SPI is to monitor the relative inter-table motion. In this section it is studied within which signal range the SPI provides information. Therefore, the interferometric contrast was computed while the remote mirrors were subsequently displaced in the various degrees of freedom; see Table 5.3. For the simulations the full optical setup presented in Figure 4.14 on p. 45 was used. Initially, the SPI was well aligned. Then, the remote mirrors were displaced in one degree of freedom with respect to the residual optics of the SPI which are located on the central table, while all other degrees of freedom remained unchanged. The interferometric contrast was calculated. When a contrast of 0.01 was computed the according displacement was defined as the maximum signal range, *e.g.* the maximum range of the SPI for lateral changes of the remote tables are 1.6 mm. This procedure was repeated for the various table degrees of freedom. The results are the same for the west and south interferometers and are summarized in Table 5.3. They are presented for an inter-table motion between the central and south tables in the coordinate system depicted in Figure 5.6b. In summary, the SPI has a signal range of about 2.2 m for longitudinal displacements, 1.6 mm for lateral displacements, and about 100 μ rad for the rotational degrees of freedom.

5.3. Impact of the radius of curvature

The measurement interferometers of the SPI use curved mirrors on the remote tables to shape the beams such that their beam parameters are identical at the beam recombiner. For the purchase of these curved mirrors it was investigated how much the radius of curvature can differ from its design value without

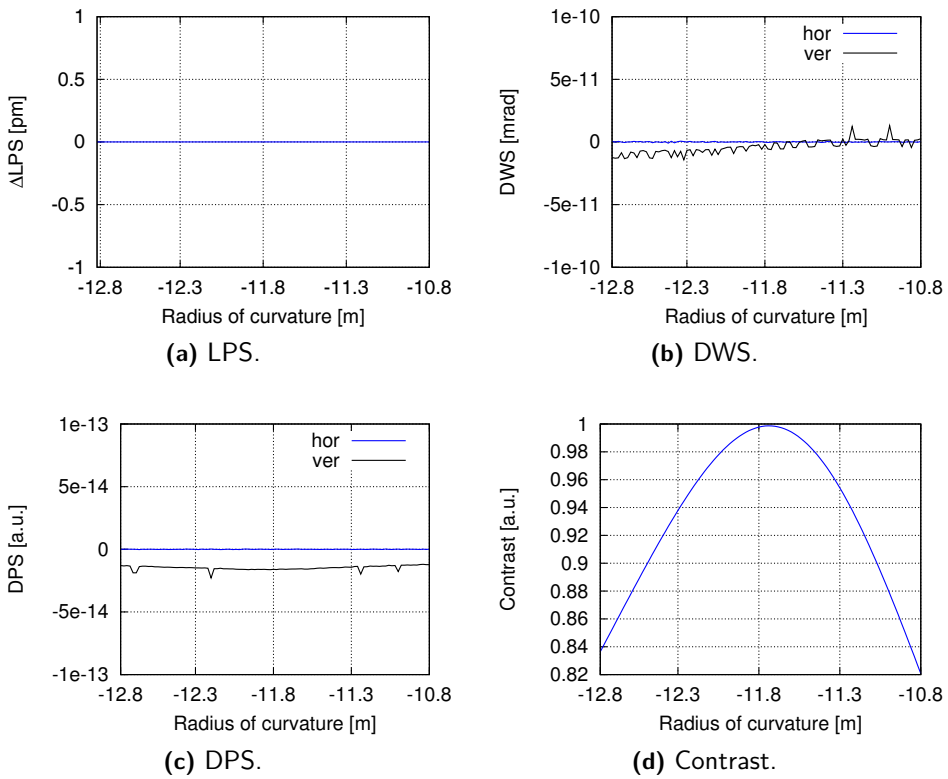


Figure 5.8.: Simulated interferometer signals in dependency on the remote mirror's radius of curvature. The dips, e.g. in Figure (a), are due to the numerical inaccuracy.

decreasing the interferometer performance.

For this purpose a well-aligned simplified setup as depicted in Figure 5.1 and design beam parameters (see Section 4.5 on p. 32) were used. The mirror's radius of curvature was changed from -10.8 m to -12.8 m while the interferometer remained aligned. Figure 5.8 shows the results. Only an influence on the interferometric contrast and none on other interferometric signals is found. For radii of (-11.8 ± 0.2) m a contrast larger than 0.99 can be realized. Including a safety margin, it was decided to order mirrors with a specification of a concave radius of curvature of (-11.8 ± 0.1) m.

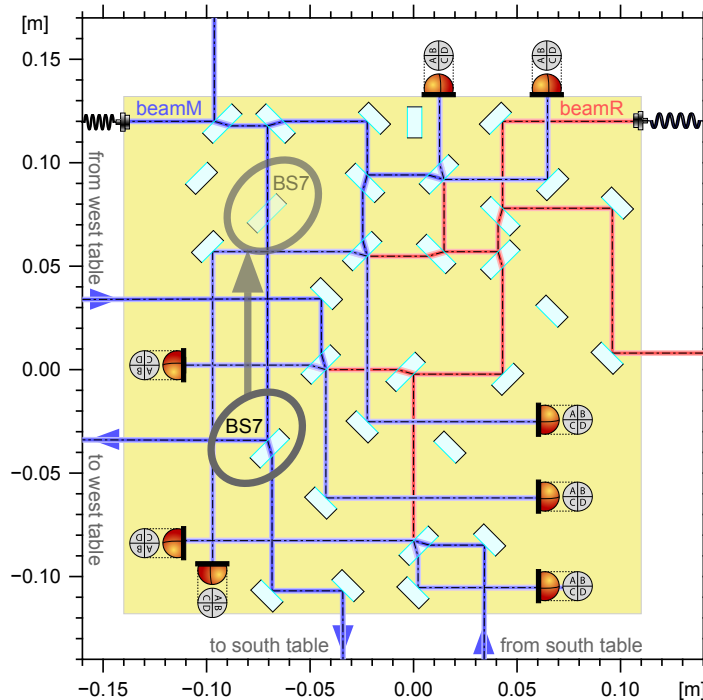


Figure 5.9.: Optical setup of the SPI optics on the central table. Beam splitter BS7 at its final position (see dark gray colored ellipse) splits the blue colored measurement beam in two beams. The beam in reflection is steered to the west table. The transmitted beam travels to the south table. Within the light gray ellipse the intermediate position of BS7 is depicted.

5.4. South interferometer

Originally, it was planned to install the west table as the second table after the central table. This was considered for the design of the interferometers of the SPI. The measurement beam is split into two paths by beam splitter BS7; see Figure 5.9. The reflected beam is steered to the west table, the transmitted beam propagates to the south table. The transmitted beam has a lateral offset with respect to the incoming beam due to different refractive indices of fused silica and vacuum and the angle of beam incidence. However, due to external circumstances the order of installation was changed and the south table was installed as second table. At this time the construction of the SPI was almost finished. As the time between the installation of the second and third tables is expected to be about a year, it was investigated how the south interferometer of the SPI can be commissioned without having the west table installed.

Table 5.4.: The difference of the south interferometer signals with beam splitter BS7 at its final, and intermediate positions. At the intermediate position BS7 is shifted northwards by 11 cm, rotated by 2° , and wedged by $2''$.

Contrast [%]	LPS [μm]	DWS _h [mrad]	DPS _h [a.u.]
2.050	-78.559	11.139	-0.170

The precision tools for the alignment and construction of the optical setup, *e.g.* CMM, CQP, that are available in the clean room are not good enough to steer the light to the 10 m apart table and still impinging a few millimeters off the tables center. At least one of the inter-table interferometers has to be assembled within the vacuum system using the 10 m long arm for *in situ* monitoring. For the other interferometer the mirror steering the light to the remote table can be attached in the clean room using the aforementioned tools, because the whole base plate can be rotated and thus be used for fine alignment. Hence, this approach is followed for the south interferometer.

Without the west table installed it is impossible to align BS7 with the required accuracy to the mid-position of the west table. Otherwise, the installation of BS7 cannot be omitted due to the induced lateral offset. For this reason BS7 is temporarily optically contacted¹ onto the base plate. Its intermediate position is about 11 cm northwards to minimize the risk of surface damage which may happen while removing the beam splitter. This removal and repositioning is necessary as soon as the west table is ready and the SPI's west interferometer installation starts.

A new position of beam splitter BS7 might result in different interferometer signals for the south interferometer. The differences for the output signals for a well aligned south interferometer with BS7 at its intermediate and final position are shown in Table 5.4. Besides a different y value for BS7 the intermediate position is rotated by 2° and the parallelism of front and rear surfaces of the beam splitter differs by $2''$. The point of reflection on the surface of the remote mirror is shifted by $60 \mu\text{m}$ resulting in a beam separation of $140 \mu\text{m}$ at the position of the photo diode. This change and the difference of the interferometer signals are small enough such that the alignment of the intermediate position of BS7 is relatively relaxed and can be changed to its final position without major changes in the alignment and control scheme of the south interferometer as soon as the west table will be installed.

¹Optical contacts are discussed further in Section 6.1.2 on p. 75.

5.5. Conclusion

In this chapter the beam alignment for the south and diagnostic interferometers was investigated for angular and transversal misalignments. It was shown that the interferometer signals are not fully decoupled and depend on the beam parameters. Simple pictures for the understanding were introduced. For example, how an angular misalignment of the two beams does not only result in a change in the DWS signal, but also to some extent to a different LPS signal. It was shown that the dependency of the interferometer signals is linear for interferometers with identical beam parameters such as the diagnostic interferometer. For the south interferometer the beams have different parameters. So, for the description of the dependency of the interferometer signals on the beam displacement higher orders are needed. A quantitative analysis of the cross-coupling has been performed computing coupling factors for the various table degrees of freedom. It will not be possible to monitor the LPS signal to $100 \text{ pm}/\sqrt{\text{Hz}}$ at 10 mHz without any additional stabilization of the table's rotational degrees of freedom, because the table's pitch motion couples to the LPS channel resulting in an LPS signal of $100 \text{ nm}/\sqrt{\text{Hz}}$ at 10 mHz.

Moreover, important information for the interferometer assembly were gained. First, the specification of the radius of curvature of the concave remote mirrors is $(11.8 \pm 0.1) \text{ m}$ which enables a contrast above 0.99 using design beam parameters for the initial beam. Second, due to the different beam parameters of the actual beams, a maximum contrast of the south interferometer is limited to 0.88 for ideal alignment. Third, the interferometer performance of the south mirror is not degraded by a retrofit of a beam splitter in its beam path which is necessary due to the changed order of installation of the tables.

This chapter gives a brief overview of different bonding techniques: hydroxide-catalysis bonding, optical contact, and UV cured epoxy bonding. This is followed by the description of the construction of the quasi-monolithic SPI including the retrofit of quasi-monolithic fiber injectors. The positioning accuracy of silicate bonded optical components is analyzed. From this suggestions for improvements of the construction of template bonded interferometers are deduced. This chapter closes with the description of the assembly of an interferometer with an arm length mismatch of about 23 m.

6.1. Bonding techniques

In the baseline design of the SPI all in-vacuum optical components have to be attached onto a base plate made of Clearceram-Z HS to realize a high mechanical stability and reduce the influence of thermal drifts. All mirrors and beam splitters are made of fused silica. At-first-glance three suitable possibilities arose to attach optical components to the base plate: the hydroxide-catalysis bonding technique, optical contacting, or the use of the UV cured epoxy Optocast 3553-LV-UTF.

6.1.1. Hydroxide-catalysis bonding

Hydroxide-catalysis bonding is a common technique to manufacture thermally and mechanically stable optical systems for space. A detailed investigation of characteristics of bonded components can be found in [74]. The bonding procedure itself is explained in great detail in [96]. For the sake of completeness

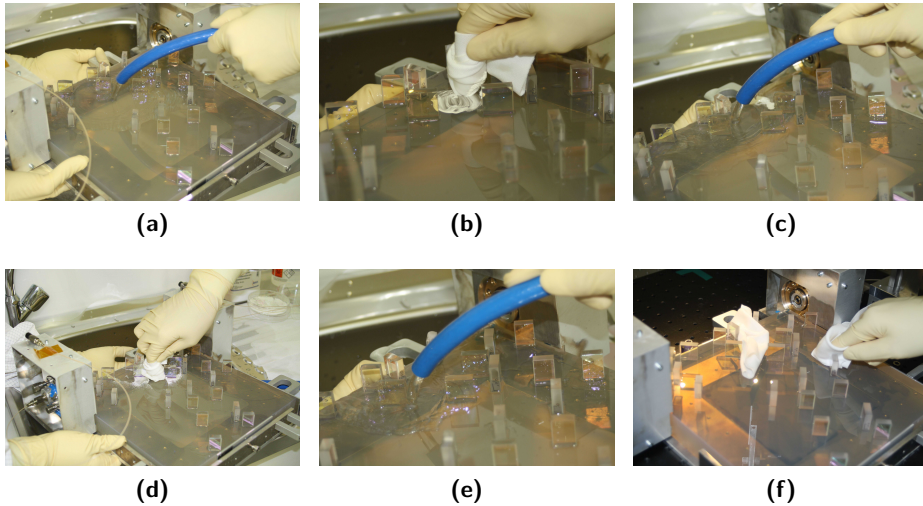


Figure 6.1.: Cleaning procedure of surfaces. (a) the surfaces are rinsed with deionized water, (b) polished with cerium(IV)oxide, and (c) again rinsed with deionized water. (d) sodium hydrogen carbonate is used to remove remaining particles. (e) after another rinsing with deionized water, (f) the cleaning is finished with several wipes with methanol.

of this thesis, a summary of hydroxide-catalysis bonding technique will be given.

Hydroxide-catalysis bonding can take place between two flat surfaces of materials which are able to form a silicate-like network. A prerequisite is a good overall flatness of the surfaces around $\lambda/10$ (with $\lambda=633$ nm). Hydroxide-catalysis bonding between these two materials happens in three steps [74]:

- 1. Hydration and etching** An alkaline bonding solution is placed on one of the to be bonded surfaces. The OH^- ions of the bonding solution etch the surfaces. Thus, the surfaces liberate silicate ions. These ions reduce the amount of OH^- ions in the bonding solution resulting in a dropping pH. The silicate ions form $\text{Si}(\text{OH})_4$ molecules.
- 2. Polymerization** $\text{Si}(\text{OH})_4$ molecules polymerize and form siloxane chains and water.
- 3. Dehydration** The water evaporates or migrates into the material and the two surfaces are rigidly connected by a 3D network of siloxane chains.

A precedent cleaning of the surfaces is required to enable the formation

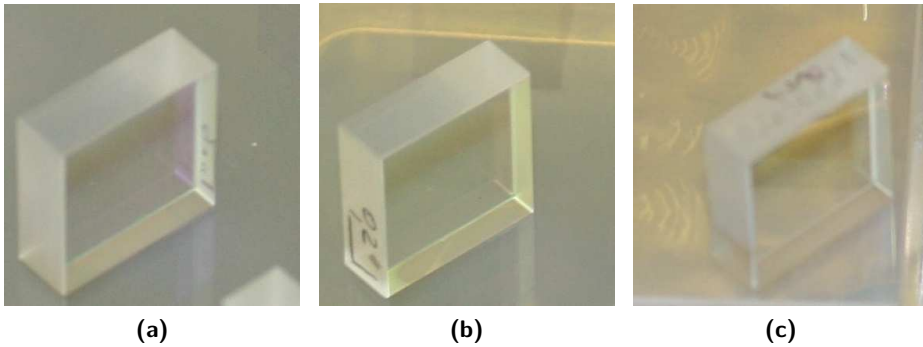


Figure 6.2.: These photographs show different types of bonding: (a) hydroxide-catalysis, (b) optical contact, and (c) Optocast 3553-LV-UTF. No visual difference between the various kinds of bonds can be observed.

of a quasi-monolithic¹ bond. The to-be-bonded surfaces have to be rinsed with deionized water; see Figure 6.1a. Next, the surfaces are polished with cerium(IV)oxide (particle diameter below $5\ \mu\text{m}$, purity of 99.9%); see Figure 6.1b. Followed by another rinsing with deionized water; see Figure 6.1c. Sodium hydrogen carbonate is used to remove remaining cerium particles, see Figure 6.1d. After another jetting with deionized water (see Figure 6.1e), the cleaning of the surfaces is finished by several wipes with methanol; see Figure 6.1f.

The bonding fluid consists of a sodium silicate solution (by Aldirch 338443) and deionized water in a ratio of 1:6. A bond between two cleaned and flat surfaces is formed when a bonding fluid amount of the order of $0.4\ \mu\text{l cm}^{-2}$ is applied and some pressure, *e.g.* due to gravity, is imposed in the direction of the normal vector of the surfaces. An example of a hydroxide-catalysis bonded beam splitter is shown in Figure 6.2a.

6.1.2. Optical contacts

Optical contact is another technique to attach glass plates to each other. A difference between hydroxide-catalysis bonding and optical contact is that the latter does not use any fluid. Optically contacted surfaces stick together due to van der Waals attraction. Thus, a condition for optical contacts are smooth and flat polished surfaces ($\lesssim \lambda/10$ with $\lambda=633\ \text{nm}$). The van der Waals po-

¹The bond is called quasi-monolithic because the optical components (material: fused silica) and the base plate (material: Clearceram-Z HS) are made of different materials.

tential per unit area between two facing solids with distance d is [97]

$$\tilde{w}(d) = -\frac{\pi\rho\rho' C}{12d^2} \quad (6.1)$$

where ρ is the number of particles per unit volume of solid one and ρ' is the number of particles per unit volume of solid two. C is the interaction constant. The strength of the optical contact which is the force per unit area is given by [97]

$$P(d) = \frac{\partial\tilde{w}(d)}{\partial d} = \frac{\pi\rho\rho' C}{6d^3}. \quad (6.2)$$

For fused silica the numerator is of the order of $0.2 \cdot 10^{-19}$ J [97] and a typical force is between $5 \cdot 10^5$ Pa and $20 \cdot 10^5$ Pa. This means, that optical contacts appear between distances d of 1.2 nm to 1.9 nm.

For optical contacts the same cleaning procedure is required as described in Figure 6.1. In the assembly, the only difference to a hydroxide-silicate bond is that no bonding fluid is applied to the surfaces. An optically contacted beam splitter is depicted in Figure 6.2b. In contrast to hydroxide-catalysis bonded components, optically contacted components can be disassembled by means of a mechanical impact, *e.g.* a careful stroke with a hammer, perpendicular to the normal vector of the optically contacted surfaces.

6.1.3. Optocast 3553-LV-UTF

The applicability of epoxy Optocast 3553-LV-UTF was investigated, due to the challenging alignment of the optics steering the outgoing and incoming beams to and from the remote tables to the beam recombiners. The advantage of using this particular epoxy is that it is UV-cured. This means as long as it is not exposed to UV light, the epoxy does not harden. This results in a practically infinite alignment time. Besides that, a very thin epoxy layer can be applied. This is of advantage as a very thin layer minimizes the chance of an angular misalignment in pitch of the glued optical component. Optocast 3553-LV-UTF has a very low residual outgassing and a CTE of $5.5 \cdot 10^{-5}$ K⁻¹ [98]. An epoxy of low CTE results in a small change of the position of the optical component when the temperature varies over time.

A small experiment was set up to test how reproducible thin epoxy layers can be produced. On several glass plates tiny drops of Optocast 3553-LV-UTF were deposit. A second plate was placed onto the glue and some pressure was applied to have a homogeneous layer of epoxy. Finally, the epoxy was cured with UV light. The thickness of the epoxy layers was measured with a CMM. Thicknesses of (11 ± 2) μm , (98 ± 20) μm , (79 ± 7) μm , and (37 ± 33) μm were

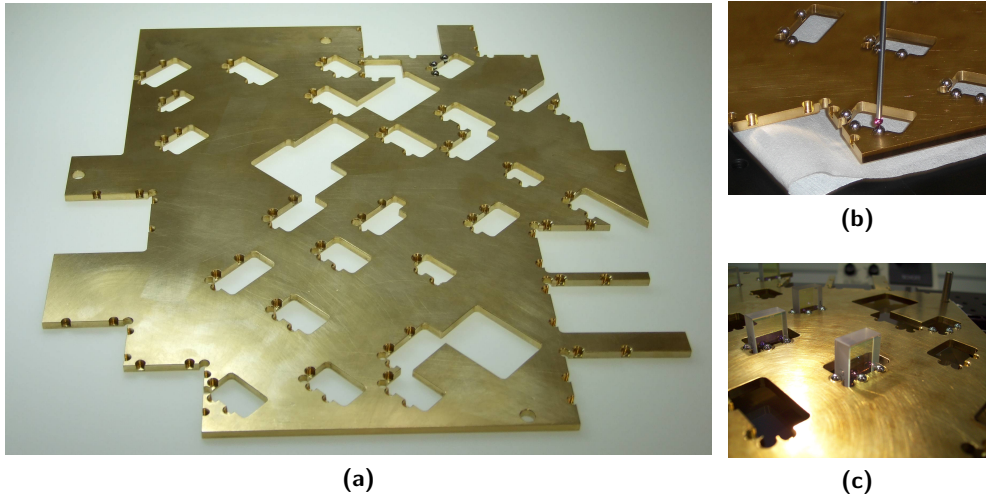


Figure 6.3.: All three photographs show the template used for bonding. (a) shows the whole template partly equipped with spheres. In (b) the position of a sphere is probed by the CMM. (c) depicts several mirrors just bonded by use of the template.

measured. A photograph of an optic glued with Optocast 3553-LV-UTF is shown in Figure 6.2c. No optical difference of the contacting surfaces can be seen when compared to the other two bonding techniques.

The technique of hydroxide-catalysis bonding has been chosen as a baseline design for the SPI because hydroxide-catalysis bonding has been proven to be successful for low frequency and low displacement noise interferometry [76; 74; 99]. Moreover, all three bonding techniques require the same precise preparation regarding component alignment. Just the cleaning of the surfaces is a bit relaxed when using Optocast 3553-LV-UTF. However, also in this case care has to be taken that no particle is between the surfaces which might result in an unwanted pitch angle between the bonded components. Optocast will be used to *in situ* set the last optical components while aligning the incoming beams from the remote tables.

6.2. Alignment and accuracy of non-critical components

The alignment of optical components¹ of the SPI was done in different ways depending on the required accuracy. Most substrate positions are relatively

¹For a more detailed description of the various alignment techniques the interested reader is referred to [3, p. 15-29].

relaxed. The alignment of, *e.g.* the beam recombiners, is more critical; see Section 6.4.2 on p. 93. The present section tackles the alignment of non-critical components using a template. The achieved accuracy is analyzed and recommendations for future template bonding are given.

A brass template has been designed and machined, see Figure 6.3a, according to the optical layout. Each optical component has a designated pocket housing three spheres which provide a reference for the position of an optical component. After manufacturing, a CMM was used to measure the component's position, see Figure 6.3b. The CMM type DEA GLOBAL Advantage which has a maximum permissible error for length measurement, MPE_E , of $(1.5 + 1.0 \times L / 333.0) \mu\text{m}$ with the currently measured length, L , in mm; has been used. The mean difference of the nominal value of each sphere and the measured value is $(0.095 \pm 0.059) \text{ mm}$ in the x -axis and $(-0.087 \pm 0.100) \text{ mm}$ in the y -axis. The largest differences are 0.206 mm in x and 0.282 mm in y .

These differences result in a different angle α , and x/y -coordinates of the bonded substrates. Figure 6.4 illustrates what is meant by α , x -, and y -coordinates. The difference between the nominal position of the substrate's corner and the substrate's corner according to the CMM measured template for each component is shown in blue in Figure 6.5b–6.5d. The graphs show that it is not possible to achieve sub-10 μm accuracy with the manufactured template. The mean values and standard deviations of $(-0.068 \pm 0.067) \text{ mm}$ in the x direction, $(0.074 \pm 0.098) \text{ mm}$ in the y direction, and $(-0.013 \pm 0.300)^\circ$ in the angle α make clear that these differences cannot be compensated by a different positioning of the template relative to the base plate.

MB1, MB2, and MB2 were the first bonded components. These mirrors were only used for the alignment of the template relative to the base plate. In the next step, MA and all mirrors that steer recombined light to photo diodes were bonded. The bonding template was aligned relative to the base plate by hand. During the bonding process the template was removed once. After that, the fiber injectors (adjustable optics holder AAH 5 axes by MICOS) were glued to the sides of the base plate. The fiber injectors were aligned

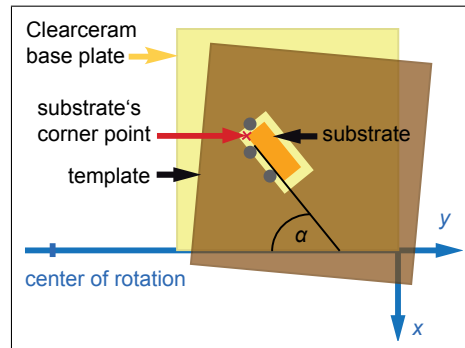
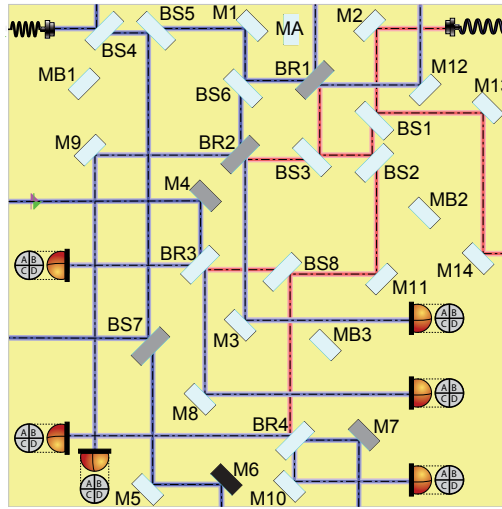


Figure 6.4.: The picture shows the coordinate system used. The corner point's x - and y -coordinates are the x and y values of the substrate.



(a) Optical layout of the central base plate.

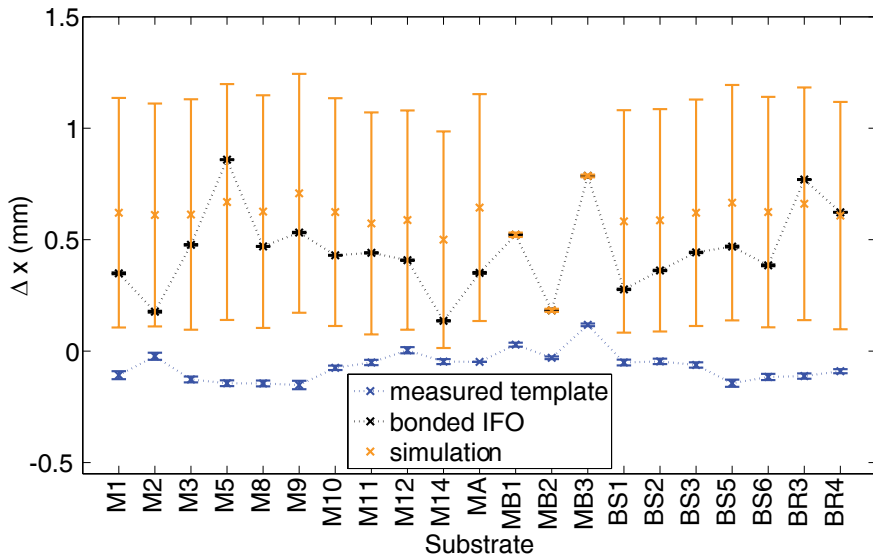
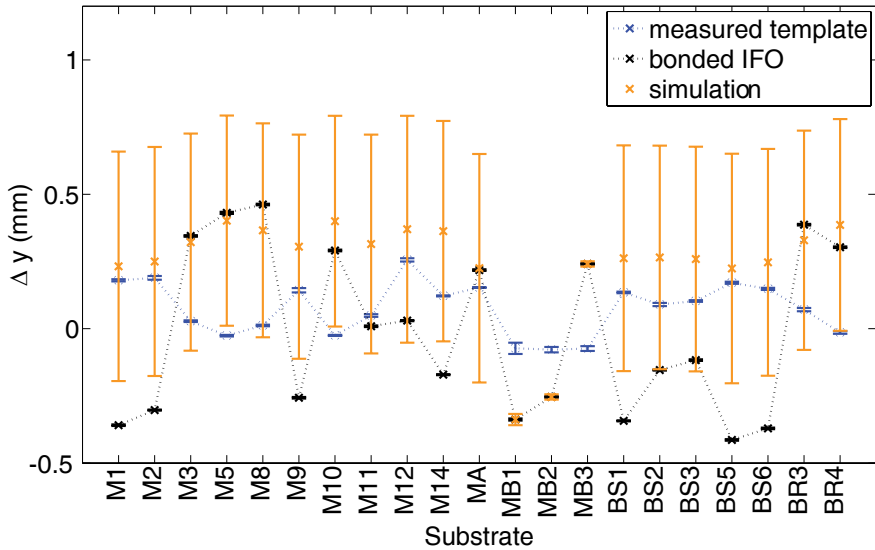
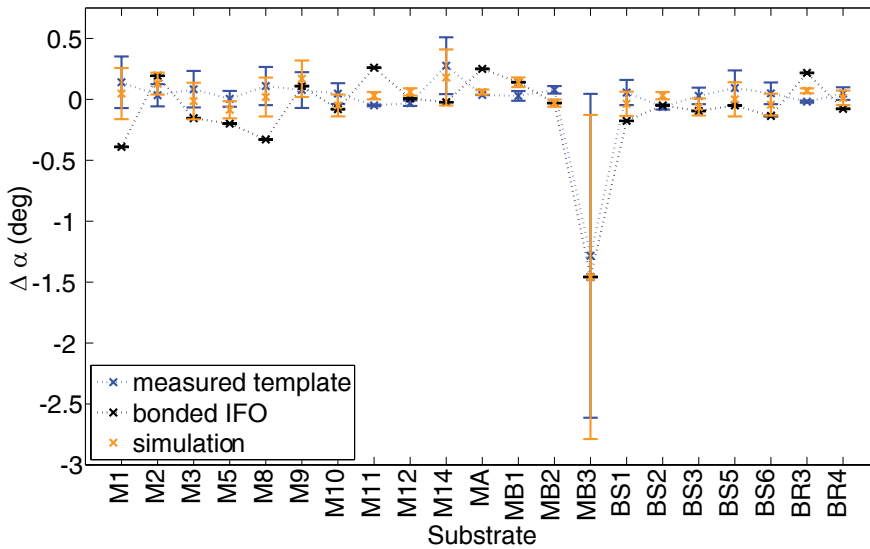
(b) Difference to design value in x for each substrate.

Figure 6.5.: (a) All dark gray colored optical components were aligned by use of light, the black mirror was bonded using a CMM and a bonding tool. All other optical components were bonded using a template. (b) The blue data points show the difference between the template's nominal value and the machined template. The black data points show the difference between the substrates nominal value and the actually bonded value. The orange points show the calculated substrate position when the machined template was aligned perfectly to the measured positions of the reference points MB1, MB2, and MB3. Some points are connected for improved display.



(c) Difference to design value in y for each substrate.



(d) Difference to design value in α for each substrate.

Figure 6.5.: (c)–(d) The blue data points show the difference between the template’s nominal value and the machined template. The black data points show the difference between the substrates nominal value and the actually bonded value. The orange points show the calculated substrate angle when the machined template was aligned perfectly to the measured position of the reference points MB1, MB2, and MB3. Some points are connected for improved display.

as described in Section 4.10 on p. 49 to the same height and parallel to the surface of the base plate.

All remaining non-crucial interferometer optics were bonded in a next bonding step, see Figure 6.3c. After all bonds were set, the corner point position as well as the angle of the substrates were measured with the CMM and compared to the design values. The result of this comparison are the black data points in Figure 6.5b–6.5d. A large discrepancy was measured between the bonded optical components (black data points) and the difference of the template’s design value and its measured values (blue data points).

Besides the imperfect machined template and imperfectly positioned reference points, the alignment of the template itself causes imperfection. Closer investigation showed that this is the dominating effect. An investigation of how reproducibly this can be done resulted in a deviation of the nominal position of the template relative to the Clearceram-Z HS base plate of (0.124 ± 0.100) mm in x , (0.160 ± 0.094) mm in y , and $(0.092 \pm 0.005)^\circ$ in angular directions.

To visualize that contribution, the machined template was aligned to the measured positions of the reference points in a simulation. Next, the template was slightly shifted within the measured placement reproducibility limits. The result is shown in the orange in Figure 6.5b–6.5d. For most substrates the black data points, *i.e.* deviation of a bonded substrate from its design value, are within the error bars of the orange data points. The remaining difference might be due to different reference spheres which were used for bonding. A different sphere can lead to an angular difference of about 0.02° .

The error bars of the template measurement and the measurement of the bonded interferometer take the measurement errors of the CMM into account according to Hernla (2007) [100]. The error bars of the other two data series incorporate the CMM measurement error of the template, interferometer, and template positioning measurements as well as the standard deviation of the reproducibility of template positioning. The last item gives, by far, the largest contribution to the mean quadratic error.

Hence, for future interferometers that will be bonded by use of a template and aiming for a better accuracy, the advice is to first, measure the template with a CMM and decide if its accuracy is acceptable. If the template can be used, the reference points should be bonded by use of an alignment tool and a CMM because the accuracy with an alignment tool is much better; *cf.* [3]. Next, the template should be aligned relative to the base plate by use of a CMM, not by hand as it was for this SPI experiment.

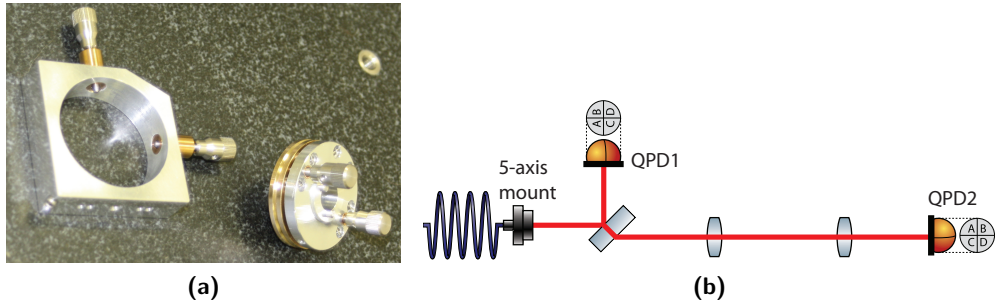


Figure 6.6.: (a) is a photograph of a MICOS AAH 5 Axes UHV mount. (b) shows a setup to measure pointing noise of the 5-axes mount.

6.3. Fiber injectors

At the beginning of the assembly of the SPI only standard, commercial (non-monolithic) fiber injectors were available. Quasi-monolithic fiber injectors cannot be bought off the shelf. Back then, some tools, *e.g.* a CQP [101], to build these injectors were not available at the AEI. Thus, an adjustable fiber injector mount (AAH 5 Axes UHV by MICOS [79], see Figure 6.6a) was chosen, which is compatible to the vacuum standard of the AEI 10 m prototype. So far, only a few bonded interferometers are equipped with monolithic fiber injectors, namely the two flight models and the Hannover model of the optical bench for LISA Pathfinder [102].

6.3.1. Commercial fiber injectors

Two commercial fiber injectors were aligned relative to each other as described in Section 4.10 on p. 49. Over the time the fiber injectors, especially the one of the reference beam, drifted. This was noticed when the first recombining beam splitter was about to be bonded, as the two beams were found to have a different height. Their coordinates and angles relative to the base plate have been measured by a CQP [103; 3] (see Figure 6.7) which was developed in the meantime. After propagating 0.7 m, the beam height of the measurement beam was 15.489 mm above the surface of the Clearceram base plate, whereas the reference beam had a height of 16.268 mm. This difference of 0.779 mm is too large to achieve a reasonable interferometric contrast with beam diameters of about 2 mm. The beam directions were measured to be $(-0.999991, -0.004152, -0.000069)$ for the measurement beam and $(0.999988, -0.004954, -0.000312)$ for the reference beam in the coordinate system depicted in Figure 6.4 on p. 78. Within several attempts to realign the 5-axes fiber mount of the reference

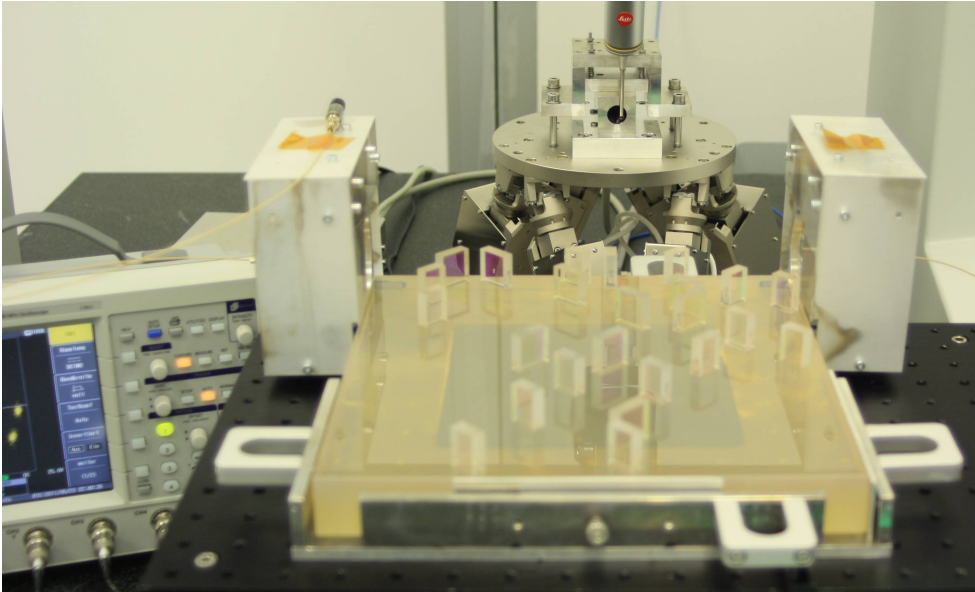
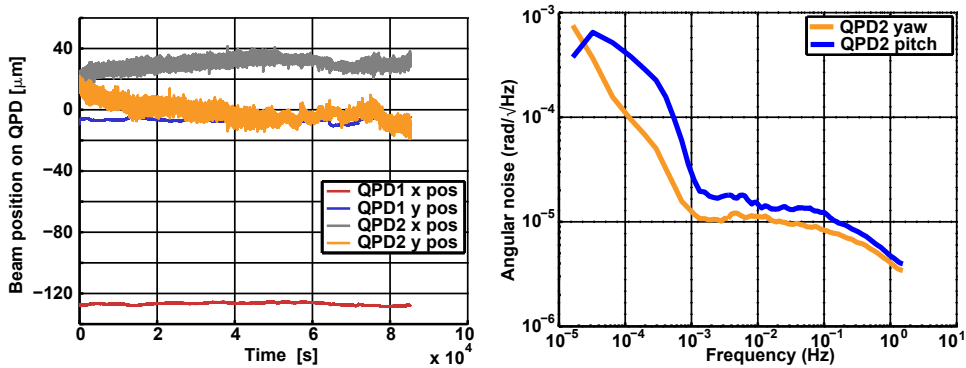


Figure 6.7.: Measurement of the beam direction using a CQP. The CQP is mounted onto a hexapod. With the hexapod the CQP is aligned relative to the beam such that the beam hits both QPDs at their center. Next the position of the CQP is measured with the CMM. It is also possible to put the CQP to a desired position and then align a beam onto the CQP.

beam such that it has the same height as the measurement beam and that it is parallel to the surface of the Clearceram base plate the aspired precision could not be achieved. Finally, the poor mounting construction of the inner part of the 5-axes mount was identified as the source of alignment error.

Beam pointing fluctuations An experiment has been set up to measure the amount of pointing noise of the 5-axes mounts. The optical layout is depicted in Figure 6.6b. The Gouy phase difference of 90° of both beams at the two QPDs results in a decoupled detection of angular and lateral beam shifts. The resulting coupling factors for beam angle rotation are 0.171 mrad^{-1} for QPD1 and -1.104 mrad^{-1} for QPD2. For this investigation the same QPDs and mounts have been used that will be used for the inter-table measurement, too. Thus the measured fluctuations are those of the system consisting of fiber injector and QPD.

Figure 6.8a shows the position of the beams on the QPD. For QPD1, sensitive for translational motion, the slopes are 25 pm/s for horizontal and -8 pm/s for vertical motion. This means that the 5-axes mount is stable in the trans-



(a) Beam position on quadrant photo diode QPD1 and QPD2. x is in horizontal and y in vertical direction with regard to the beam axis.

(b) Measured angular noise of a 5-axes mount.

Figure 6.8.: Beam fluctuations for the MICOS AAH 5 Axes UHV measured in air.

lational degree of freedom. All changes in position detected by QPD2 are due to angular noise of the 5-axes mount. A spectrum of this angular noise is shown in Figure 6.8b. The aspired angular noise for the SPI is $10 \text{ nrad}/\sqrt{\text{Hz}}$ at 10 mHz which is three orders of magnitude below the measured angular noise of the 5-axes mount. Since this noise is not necessarily common in both mounts (as the problem of different beam height showed), it was necessary to replace the 5-axes mounts by ultra-stable quasi-monolithic fiber injectors.

As mentioned before, in the meantime a CQP was built at the AEI Hannover [103] and a pair of quasi-monolithic fiber injectors for the SPI was constructed [104]. Hence, the central optical bench of the SPI was upgraded by replacing the commercial 5-axes mounts with the custom-made quasi-monolithic fiber injectors. These efforts are described in the following.

6.3.2. Retrofitting with quasi-monolithic fiber injectors

Quasi-monolithic fiber injectors have the advantage of a better stability in pointing noise and drift. Moreover, no realignment of these injectors is possible. On the one hand, this makes the initial injector alignment much more crucial. On the other hand it can be an advantage when realignment is not easily possible as in case of the SPI. Here, the central base plate will be positioned below the suspended beam splitter of the SQL interferometer (see Figure 4.2 on p. 29) and thus not easily accessible. Figure 6.9 shows a CAD drawing

Table 6.1.: Beam parameters of the quasi-monolithic fiber injectors [104]. w_0 is the waist of the beam. z_0 is the position of the waist. $z_0=0$ is the front face of the fiber injector. The positive axis points in the direction of beam propagation.

Beam	FIOS	Axis	$w_0[\mu\text{m}]$	$z_0[\text{cm}]$
Reference	2	V	1030.815	-28.653
Reference	2	W	1024.740	-4.805
Measurement	1	V	942.985	-110.440
Measurement	1	W	990.012	-44.985

of a quasi-monolithic fiber injector made of fused silica. These injectors were custom-made for the SPI according to the beam parameters presented in Section 4.5 on p. 32. The dimensions of a fiber injector assembly should not exceed $38\text{ mm} \times 35\text{ mm} \times 38\text{ mm}$ (length \times width \times height) to retrofit the injector to the existing SPI setup, see Figure 6.7. Two quasi-monolithic fiber injectors, whose design is based on the fiber injectors for LISA Pathfinder [105], have been built for the SPI and characterized within a Bachelor's thesis [104]. The according beam parameters are shown in Table 6.1. Their dimensions are $20\text{ mm} \times 26\text{ mm} \times 28\text{ mm}$ (length \times width \times height).

The fiber injectors are attached to the base plate via a post. This allows independent adjustment of the pitch (fiber injector to post) and yaw (post to SPI base plate) degrees of freedoms of the beam relative to the surface of the base plate; see Figure 6.9. The alignment in pitch is much more critical than the yaw alignment. In contrast to yaw, the pitch degree of freedom cannot be compensated by a different position of a subsequent mirror or beam splitter. This angular alignment work has been done within this PhD thesis and is described now.

6.3.2.1. Pitch and beam height alignment

It is advantageous to start with the pitch alignment of the quasi-monolithic fiber injectors and not with the yaw alignment. If one would start with the yaw alignment, the SPI base plate would need to be turned onto its side to use the gravitational force for alignment¹ risking a damage, *e.g.* break off parts of the optical components, of the almost fully assembled base plate. Thus, the first assembly step was the pitch alignment.

¹Further information is available later in this section.

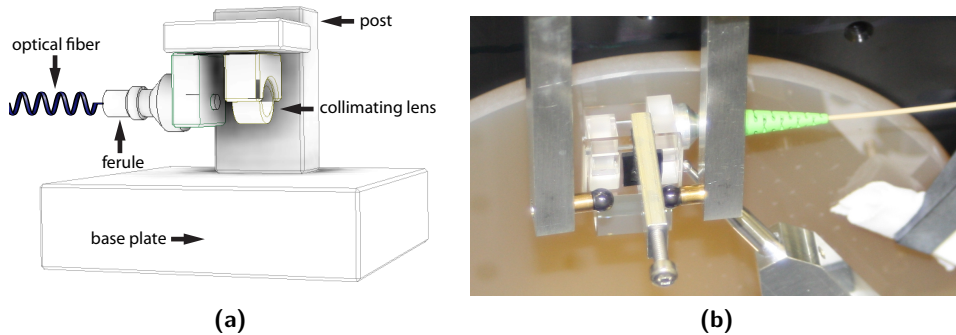


Figure 6.9.: (a) A CAD drawing of a quasi-monolithic fiber injector. It is made of fused silica and was assembled using silicate bonding, thus providing a mechanically stable fiber mount. (b) Alignment of the fiber injector onto its post. A small counterweight is attached to the fiber injector base plate to compensate the weight of the lens and fiber block.

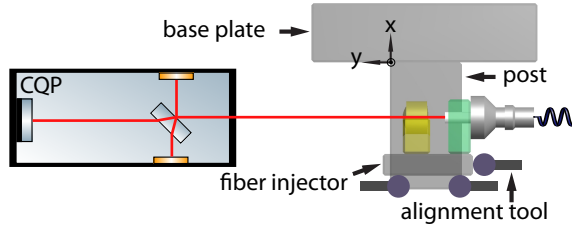
For this purpose, the post of a fiber injector was fixed in order to align a fiber injector relative to it. The easiest and best solution is to optically contact the post onto a round Zerodur base plate (\varnothing 150 mm) which was at hand.

With a quasi-monolithic setup the best alignment is possible if the normal vector of the to-be-connected surfaces is approximately along the direction of the gravitational force. Hence the whole setup (round base plate and post) is rotated by 90° , see Figure 6.9b. In this way, it is ensured that no gap is in between both surfaces. A counter weight needs to be attached to the fiber injector to not fall onto the heavier side equipped with fiber and lens; see Figure 6.9b.

A movable three point reference was used for the alignment of the fiber injector onto its post. It is a modified version of the alignment tool depicted in Figure 6.11. The tool incorporates three arms each carrying a sphere hanging from above over the base plate. As for the bonding template these spheres define the position of the optical component. Each sphere can be moved in longitudinal and transversal directions independently. Furthermore, all three spheres can be moved together in height, longitudinal, and transversal directions. A rotation around the center of a component is also possible.

In the modified version of the alignment tool, the third arm was replaced by a sphere touching the fiber injector from below. This modification was necessary neither block the outgoing beam nor to stand in the way of the fiber. Moreover, two manual alignment stages (M-SDS25 by Newport) responsible for the alignment perpendicular to the direction of the normal vector of the base plate (*cf.* Figure 6.9b) have been replaced by piezo motor driven linear

Figure 6.10: Top view of the height and pitch alignment setup of the quasi-monolithic fiber injector.



stages (Agilis LS 25) which provide a more accurate positioning of the two alignment spheres that are used for pitch alignment. Their inter-sphere distance is about 16 mm. The smallest step of the manual linear stage M-SDS25 would result in an angular change of 1.25 mrad which is too coarse. With the piezo motor driven linear stages angular changes of about 3 μ rad are in principle possible.

As illustrated in Figure 6.10 the fiber injector can only be pushed towards the base plate. The motion away from the base plate is realized by placing a fluid between the fiber injector and its post and putting the whole setup onto a breadboard with a slope of a few degrees. In this way the fiber injector is sliding on a liquid film towards the spheres of the alignment tool away from the base plate.

The outgoing beam of the fiber injector is monitored by a CQP which is placed on a hexapod (M-824.3VG by Physik Instrumente). With the CMM a coordinate system is constructed from three planes, namely the surface of the base plate, lower side of the post (the plane opposite to the surface carrying the fiber injector), and the post's front face pointing towards the CQP. This coordinate system is used as datum reference frame (see Appendix C.1 on p. 133). For its orientation see Figure 6.10. By use of a hexapod the CQP is orientated to the design values of the beam direction. For the fiber injector of the reference beam these values are (0,1,0) and (-15 mm, y , z) for the point on the front surface of the CQP where the beam enters the device. z is the distance between beam and post. It is a fixed value and cannot be changed. y is the distance between the front face of the post and the front face of the CQP. The larger this distance the smaller angular deviations can be monitored. However, the probing volume of the CMM is finite (0.7 m \times 1 m \times 0.5 m). During the height and pitch alignment the distance between CQP and post was 502 mm and 548 mm, respectively. The injector of the measurement beam is attached at its opposite side to the post. Hence, the design values for the beam directions are (0,1,0) and (15 mm, y , z).

When the best possible alignment of the fiber injectors onto the CQP was realized the fiber injectors were glued onto their post. It was observed that

removing the fiber injector and putting it back to its original position always resulted in a different position. Thus, during the alignment, the fiber injector was sitting on a tiny drop of Optocast 3553-LV-UTF (approximately 1 μl). This glue sets when exposed to UV light. The glue was cured using the UV light source Omnicure Series 1000 for 2 min with 100 % intensity at a distance of 3 cm to 5 cm. During the hardening process no change of the alignment was observed with the CQP.

The beam directions in parameter form before and after the curing were

$$\begin{aligned} &(-14.938978, 502.410753, 10.810653) + p \cdot (-0.000107, 0.999869, -0.016178) \\ &(14.834070, 548.179942, 28.576706) + p \cdot (-0.000128, 0.999783, 0.020848) \end{aligned}$$

with the scalar p . The first parameter form belongs to the reference beam, the second one to the measurement beam. This corresponds to an differential pitch of -0.474 mrad between reference beam and measurement beam. The best possible contrast within the reference and diagnostic interferometers with this differential pitch angle (ΔRx) is calculated using the equation [106]

$$c = \exp\left(-\frac{\Delta x^2 + \Delta z^2}{w_0^2}\right) \exp\left[-\frac{(\Delta Rx^2 + \Delta Rz^2) k^2 w_0^2}{8}\right] \quad (6.3)$$

and is 37.5 % assuming identical beam parameters (waist w_0 of 1 mm) and perfect alignment in yaw (ΔRz) and the lateral degrees of freedom (Δx , Δz). k is the wave number.

Challenges within the alignment process were the strong and changing torque due to the stiff fiber. The fiber of the quasi-monolithic fiber injectors is 0.5 m long and connected to an FC/FC-APC fiber connector. The fiber itself was randomly twisted which could not be fully bypassed. The fiber was suspended to the cross-beam of the alignment tool to be at the same height as the fiber injector. Anyhow, whenever the fiber injector was adjusted by the alignment tool the torque of the fiber changed. The heavier FC/FC-APC fiber connector acted as a fixed point. In future, it would be beneficial to use a longer at least 1 m long fiber instead of a 0.5 m to minimize the impact of the fiber connector. The torque can also be decreased by using a softer, more flexible fiber and by increasing the dimensions and thus the weight of the fiber injector base plate. This also reduces tipping of the fiber injector which was a problem especially during coarse alignment of the fiber injector. On a larger base plate the lens and fiber can be positioned such that the beam starting point is approximately in its center. Then the two spheres of the alignment tool can be located symmetrically around the starting point of the beam. This would ease the alignment of the translational degree of freedom. Having the small,

20 mm long base plates, the two spheres could not be placed symmetrically around that point. So, every change in translation resulted also in a change in rotation.

Before the installation of both fiber injectors to their final position onto the base plate of the SPI, the injectors were placed next to each other to measure again the differential pitch of their outgoing beams. This time this was done in the same datum reference frame. Already before the start of that measurement it was obvious that the differential pitch of both beams is larger than -0.474 mrad.

The so detected beam directions in parameter form are

$$\begin{aligned} &(178.288911, 319.420196, 14.588931) + p \cdot (0.062545, 0.998019, 0.006858) \\ &(176.536937, 319.291989, 13.811248) + p \cdot (0.084559, 0.996373, 0.009562) \end{aligned}$$

Again, the first direction belongs to the reference beam and the second one to the measurement beam. In this datum reference frame z denotes the beam height above the surface of the base plate. The y -axis points along the direction of beam propagation. This results in a differential pitch of -2.725 mrad which is about a factor of six higher than the value measured during the assembly of the fiber injectors onto their posts. With this differential pitch angle no interferometric contrast is possible (*cf.* Equation 6.3).

The reason for this discrepancy was identified to be the condition under which the used datum reference frame has been constructed during the injector assembly. A brief introduction to CMM probing strategy and datum reference frame is presented in Appendix C.1 on p. 133.

The datum reference frame for the assembly of the fiber injector onto the post was spanned from the subsequent planes: the surface of the round Zerodur base plate (\varnothing 150 mm) which has been probed first, next the lower plane of the post (28 mm \times 16 mm), and the front face of the post (28 mm \times 10 mm) have been probed. All planes were probed with nine points distributed in 3 \times 3 squares over roughly the whole area. The last plane is with a height of 10 mm relatively small. Almost always this geometric feature was not automatically recognized by the PC-DMIS software as a plane, but as a line. This indicates that the angular error of this plane is much higher than that of the plane for the round base plate surface. It is not easy to quantify this number. However, the experiment verified that using the datum reference frame constructed by the planes of the round base plate and the post always led to a difference in pitch of about -0.5 mrad; whereas a datum reference frame built from three planes of the 250 mm \times 250 mm \times 30 mm base plate of the SPI resulted in a differential pitch of about -2.7 mrad. Planes of the SPI base plate were always automatically recognized as planes. Thus, the recommendation is to adapt

the C code of the CQP such that it does not require a coordinate system of the workpiece, but just one plane to only measure the pitch angle between the beam and the large surface onto which the post of the fiber is contacted. This will reduce the error in the pitch measurement.

6.3.2.2. Yaw alignment

The positioning of the fiber injector (the assembly of fiber injector and post is from now on just called fiber injector) onto the base plate is relatively uncritical compared to the alignment of the pitch degree of freedom. At the time of the retrofit of the fiber injectors no beam recombiners have been bonded yet. Thus, at a later stage small misalignments in the yaw degree of freedom of the beam can be compensated by the beam recombiners. The impact of the location of the waist on the interferometer signals such as contrast, is negligible within the possible position range of the fiber injectors, *e.g.* the difference in contrast is below 1‰.

The alignment tool was used to position the fiber injectors onto the base plate. For the alignment different diagnostic techniques have been used. On the one hand the outgoing beam of the fiber injector has been monitored with the CQP. For the reference beam the beam reflected by BS3 and for the measurement beam the beam reflected by BS4 (see Figure 6.5a on p. 79) have been observed. The CQP has been moved to the design position of the according beams. The fiber injector has been adjusted such that the injected beam hits the CQP best. On the other hand the beam spot on each optical component was checked with a viewing card in parallel. When both conditions were met the fiber injectors were optically contacted onto the base plate.

6.3.2.3. Additional polarization beam splitter

Only light of the same polarization contributes to the interference signal. Thus, it is beneficial to ensure that solely light of the desired polarization (*s*-polarized light) travels within the interferometer. The quasi-monolithic fiber injectors do not include a beam polarizer. Due to their required small dimensions it was not feasible to incorporate a beam polarizer. Hence, additional polarizing beam splitters had to be incorporated to the experimental setup of the SPI.

For the reference beam it was feasible in terms of space to use a polarizing beam splitter in reflection and right after the fiber injector by a slight modification of the setup. The fiber injector was rotated by 90° and slightly shifted southwards. In case of the measurement beam this was not possible without blocking the incoming beam from the west table. Thus, two beam polarizer were placed in transmission in the beam path. All polarizing beam splitters

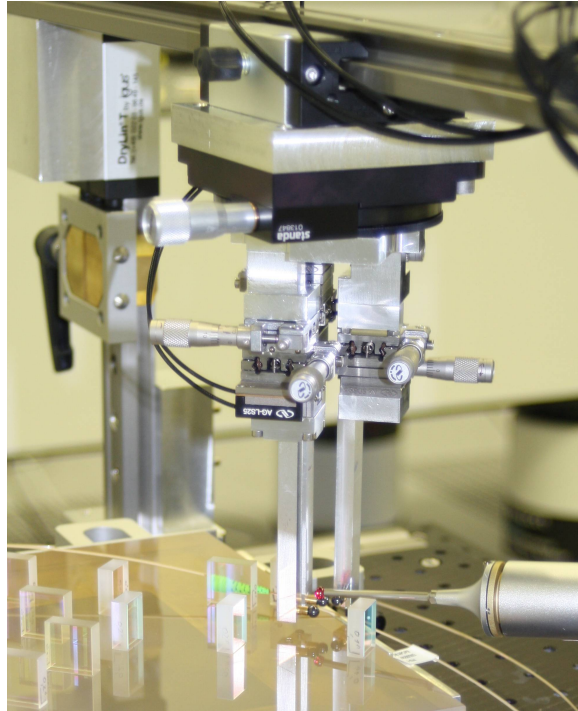


Figure 6.11: This photograph shows the alignment tool while the position of one of its spheres is probed by the CMM.

should not introduce any additional difference in the pitch degree of freedom of the two beams. Thus, out of 40 polarization beam splitters the three resulting in the smallest differential pitch of the beams have been chosen. For this purpose a beam splitter was intermediately placed at the position of BR1. The CQP monitored the differential pitch between the measurement and reference beams and was placed in the reflection port of BR1 for the measurement beam. The datum reference frame for the CQP was constructed from three planes of the SPI base plate. In this way three polarization beam splitters have been picked. For the modified layout including polarizing optics see Figure 6.12.

6.4. Alignment of critical components

The alignment of beam recombiner and optics steering the beams towards the remote tables is critical. The realized accuracy using a template (see Section 6.2, p. 77) is not sufficient. Thus two different ways each utilizing an alignment tool (see Figure 6.11) were used. One option uses the CMM, the other one employs light.

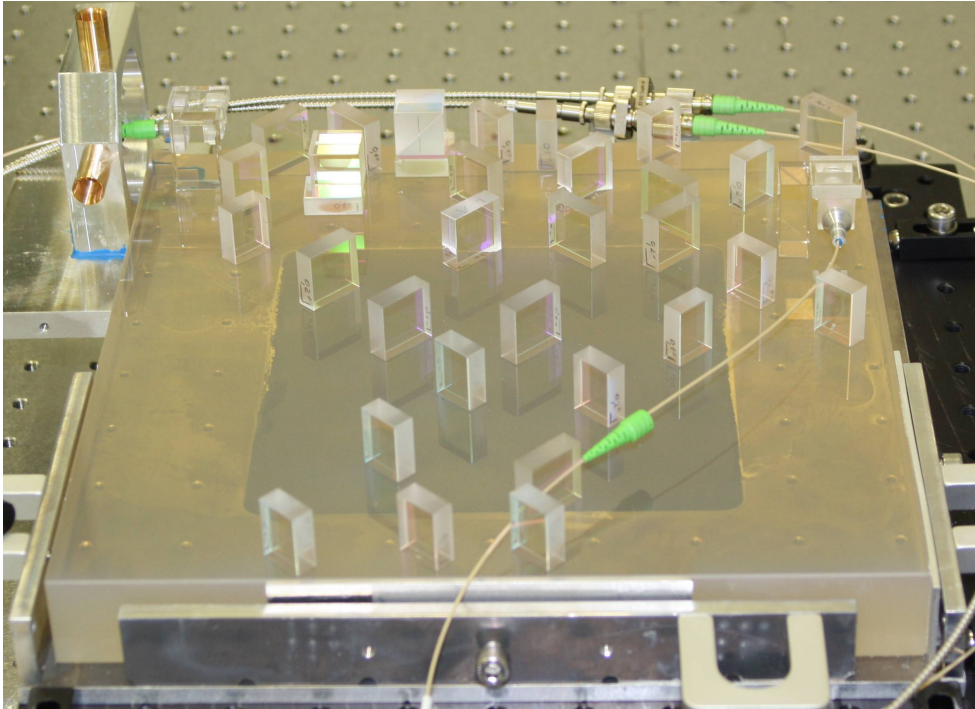


Figure 6.12.: The base plate before leaving the clean room. The setup is almost finished; only the recombing mirrors steering the light from the remote table towards the last beam splitter are missing. They will be attached online inside the vacuum system of the AEI 10 m prototype.

6.4.1. Coordinate measurement machine aided alignment

Optics M6 and BS7 (see Figure 6.5a) steer the light towards the remote tables. The CMM and an alignment tool (see Figure 6.11) were used for their adjustment. Each of the three arms of the alignment tool bears a sphere made of silicon mono-nitride. The arms are attached to two micro-meter stages. The spheres define the position of the optical component. The position of each sphere was probed with the CMM and adjusted by the micro-meter stages. This was done in an iterative process for all three spheres until they were at their design positions. Next, the optics were optically contacted onto the base plate.

6.4.2. Alignment of recombining beam splitters

For this stage of the alignment, the reference and measurement beams were injected onto the Clearceram-Z HS base plate. The recombining beam splitters BR1 and BR2 were placed with a tiny drop of Optocast 3553-LV-UTF (approximately 1 μ l) onto the base plate allowing pre-alignment of BR1 and BR2. The alignment tool depicted in Figure 6.11 was used for the alignment. Both beams were adjusted to overlap at the beam recombiner (near field) and at a point in the far field. In parallel, the interfered light was detected on a photo diode and BR1 as well BR2 were aligned such that the contrast was at its maximum. Finally, the beam splitters were bonded in position by exposure to UV light (light source: Omnicure Series 1000, 2 min, 100 % intensity, distance 3 cm to 5 cm). For BR1 the contrast is 14 % and for BR2 the contrast is 33 %. For BR1 this is 53 % of the maximum achievable contrast with the measured beam coordinates. For BR2 this value was 82 %.

The alignment was limited by the residual angle in pitch of the two beams. To slightly compensate this angle both beam combiners were glued (instead of hydroxide catalysis bonded or optically contacted) onto the base plate allowing a small adaptation of the pitch angle for the reflected beam. However, these contrast values are above the required level of 9.6 % determined in Section 4.12 on p. 52.

6.4.3. Construction of the south interferometer

For the alignment of the south interferometer¹ a slightly modified *in situ* method of alignment of the beam recombiners (see Section 6.4.2) was used. In contrast to the reference and diagnostic interferometers, the last bonded optical component of the south interferometer was not a recombining beam splitter, but a mirror, M7, (see Figure 6.5a on p. 79) steering the incoming light from the south table to a beam recombiner. CMM aided alignment is too inaccurate to position both mirrors steering the outgoing and incoming light to/from the south table well enough such that the remote mirror is still located on the table's center. Thus, M7 was aligned and bonded to the base plate within the vacuum system of the prototype using the 23 m long arm. The alignment tool was used to do this. During the adjustment of M7 some force is applied to the central table. Thus, the central table has to be mechanically clamped, otherwise the table would move and change its alignment every time

¹At the time of writing of this thesis the assembly of the west table has not started. Thus the assembly of the west interferometer could not be finished within this thesis. However, the alignment procedure of the west interferometer will be similar to that of the south interferometer.

some force is applied. Clamping means that the table cannot move in any degree of freedom. The south table on the other hand remained free utilizing its good isolation performance.

The initial step was to adjust the tables relative to each other. For the SPI they have to be of the same height. The tables have to be parallel with reference to the ground to minimize cross-coupling from the vertical to horizontal degree of freedom in the mirror suspensions that will be placed on top of both tables.

First, the central table was clamped such that all actuators are at mid-range. With a 2-axes machine spirit level of a precision of 0.05 mm/m the parallelism was measured. The position of the clamped table was modified until the table was parallel within measurement precision.

Next, the height of both tables was measured with an hose filled with isopropanol. The inter-table height was different by 11 mm with all actuators of both tables mid-range. This result was confirmed by a measurement using a laser spirit level with a precision of ± 0.1 mm/m[107]. The south table was shimmed by 11 mm and leveled by changing the distribution of masses on its top.

The base plate depicted in Figure 6.12 was placed at its design position on the central table marked by scratch marks and rotated in yaw such that the outgoing beam hits the remote mirror in this horizontal center. This base plate was shimmed (shim thickness 100 μm) at two points to adjust the measurement beam parallel to the table top. Next, the vertical clamping of the central table was slightly modified in pitch such that the outgoing beam hits the remote mirror at its vertical center. The south table pitch alignment was done by actuation of the LVDT resulting in a measurement beam parallel to and of the same height as the reference beam.

Now, the alignment of mirror M7 started; see Figure 6.13. Again, the mirror was placed onto a tiny drop of Optocast 3553-LV-UTF and the alignment tool was used. The recombined beam was monitored by two methods: first, in the reflection port for the measurement beam of beam recombiner BR4 the beams were detected with a wincam (DAT-WinCamD-UCD23 by Laser2000); second, in the transmission port for the measurement of BR4 the overlap of both beams was monitored with a viewing card at the beam recombiner (near field) and 6 m away from it. With the wincam an easier beam alignment in the (or close to) near field was realized. Before the curing, the wincam was also used to ensure that no glue is smeared over the mirror coating. Monitoring the beams at a distance of 6 m was an excellent tool to detect small misalignments in yaw. In contrast to the bonding conducted in the clean room it was not possible to angle the base plate such that the mirror floats against the spheres

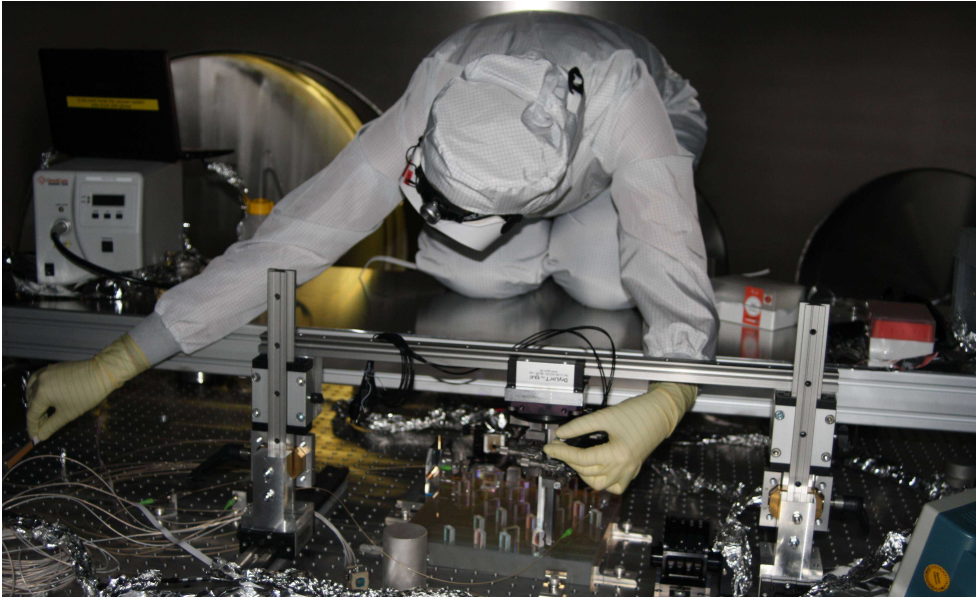


Figure 6.13.: Alignment of the mirror M7 inside the vacuum system.

of the bonding tool. The ranges of the table actuators are not large enough to change the pitch of the central and south tables ending up with both tables in one plane. Therefore, mirror M7 was pushed by hand against the spheres of the alignment tool. After the best position of M7 has been found it was not possible to remove M7 and replace it back to its original position resulting with the same contrast. Thus, optical contacting and hydroxide-catalysis bonding technique could not be used to attach M7 to the base plate. During the alignment of M7 the best contrast was 36 %. For 2 min 100 % intensity of the UV light source Omnicure Series 1000 at a distance of 3 cm were irradiated onto the glue to cure it and finalize the construction of the south interferometer.

6.5. Characterization of the optical bench

The optical bench was characterized in terms of interferometric arm length mismatch and beam parameters. This work is presented here.

6.5.1. Arm length of the interferometers

The arm length mismatch of the different interferometers was calculated by using the results of the CMM probing the individual optical components and

Table 6.2.: Measurement beam parameter of the south interferometers. w_0 is the waist of the beam. z_0 is the position of the waist. $z_0=0$ is on the front face of the beam recombiner. The positive axis points in the direction of beam propagation.

Interferometer	Beam	Axis	$w_0[\mu\text{m}]$	$z_0[\text{cm}]$
South	Measurement	V	1181.843	415.191
South	Measurement	W	1066.250	438.069

the software tool *Optocad*. The armlength mismatch of the reference interferometer is 65.0 mm. For the diagnostic interferometer this value is 62.5 mm. The reason for this arm length mismatch is not due to inaccurate bonding of the optical components, but to the retrofit of the fiber injectors and the resulting changes in the optical setup. For the “old“ conventional fiber injector configuration, the arm length mismatch is 1.0 mm for the reference interferometer and -1.5 mm for the diagnostic interferometer. This is similar to the realized arm length difference achieved with adjustable bonding using a CMM and a bonding tool; *cf.* [3, p.118]. Hence, with template bonding about the same arm length mismatches are realized as with adjustable bonding. The arm length mismatch of the south interferometer was measured to be about 23.26 m.

6.5.2. Beam profile, radius of curvature, and contrast

The interfered beams were monitored with a wincam (Strahlanalysesystem-DAT-WinCamD-UCD23) to visualize the alignment quality of the interfered beams. The measurements were performed at the positions of the photo diodes (QPDD2, QPDR1, QPDS2). The results are presented in Figure 6.14. Figure 6.14d and 6.14e underline the differential beam angles in pitch. The interfered beams of the south interferometer have a Gaussian profile of 78 % whereas the interferometric contrast was just 35 % (with equal laser powers of the individual beams and the same polarization). The contrast depends on the radius of curvature of the remote mirror; see Section 5.3, p. 67. Thus, the measurement beam going to the remote mirror and the incoming beam were measured at several positions with the wincam. The according beam parameters were calculated with *JamMt*. Table 6.2 shows the results for the incoming beam. With *Optocad* the mirror’s radius of curvature was determined to be -12.3 m in the sagittal plane and -12.2 m in the tangential plane. In case of

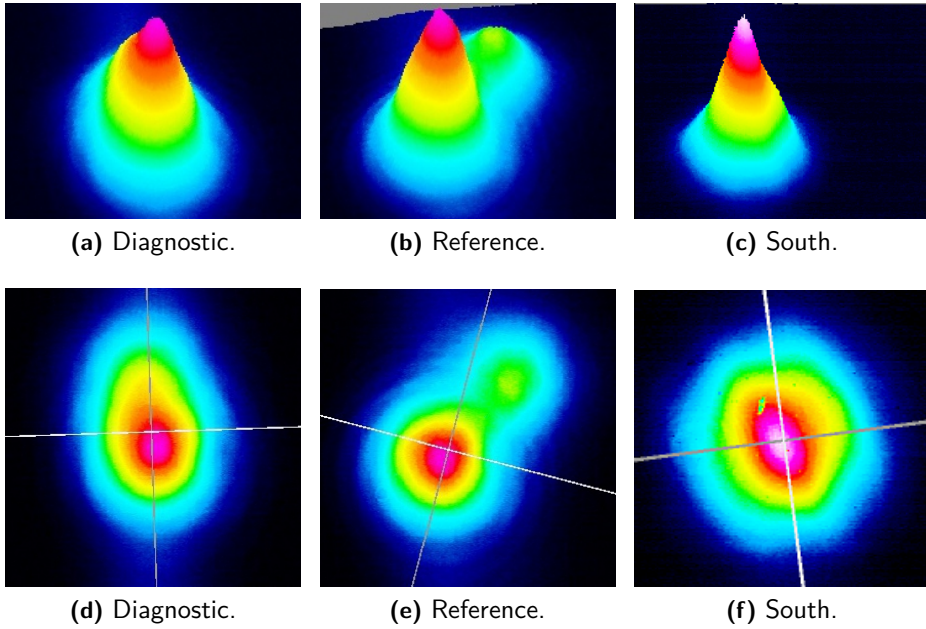


Figure 6.14.: Beam profile of the interfered beams of the three different interferometers. The first line shows a 3-dimensional view, the second line the according top view. A difference in height can be seen in the vertical axis, a difference in yaw alignment on the horizontal axis.

perfect alignment and design beam parameters this results in a 6% drop of contrast; see Figure 5.8, p. 68. However, so far the south interferometer could not be aligned to a contrast better than 53%. Besides the alignment quality, the interferometric contrast is a function of the beam parameters. For two perfectly aligned beams of equal power the contrast, c , depends on the Rayleigh range and distance between the position of the waist and the place of interference; see Equation 5.1 on p. 58.

Thus, the contrast can be calculated from the measured beam radius, waist, and radius of the wavefront curvature.

With a Shack-Hartmann wavefront sensor (Thorlabs WFS150, micro lens array MLA150M-7AR) the curvature of the wavefronts of individual beams was measured. The measurement software fits a set of Zernike functions to the wavefront. The radius of curvature of a wavefront is calculated based on the fifth Zernike term. Figure 6.15 shows the wavefront, the radius of the wavefront is displayed in the captions. Using these numbers and Equation 5.1, the contrast for well aligned diagnostic and reference interferometers

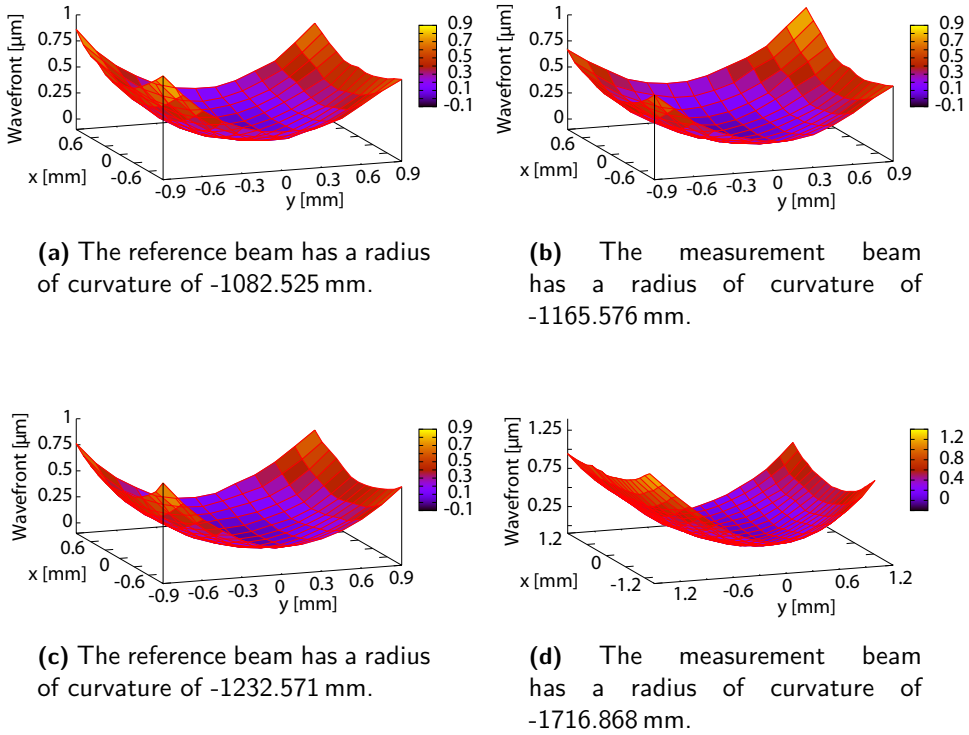


Figure 6.15.: Wavefront measurements of the individual beams of the diagnostic [(a)-(b)] and south [(c)-(d)] interferometers. The distance between beam recombiner and Shack-Hartmann wavefront sensor was 476 mm for the diagnostic interferometer and 878 mm for the south interferometer.

was calculated to be 99.7%. This number is backed by a measurement in [104, p.35]. Here an interferometric contrast of 97% was realized using the quasi-monolithic fiber injectors of the SPI and adjustable optical mounts for beam alignment. For the south interferometer the maximum achievable contrast is 90.3% with the measured beam parameters.

6.6. Conclusion

The construction and bonding accuracy of quasi-monolithic interferometers was presented. The bonding accuracy for template bonding was (-0.068 ± 0.067) mm in the x direction, (0.074 ± 0.098) mm in the y direction, and $(-0.013 \pm 0.300)^\circ$ in the angle. For comparison the accuracy using an align-

ment tool and a CMM is $\pm 10\ \mu\text{m}$ for position and $\pm 0.010^\circ$ or $\pm 0.023^\circ$ in angle depending on the component size [3, p. 99-100]. However, the realized interferometric arm length mismatches are approximately equal (1.0 mm and 1.5 mm *vs.* 0.5 mm and 1.5 mm). The advantage of a template is that more than one optical component can be bonded per bonding session, making the process considerably faster. A good compromise is to use a CMM-based milling machine for manufacturing the template. Such a milling machine provides a higher machine accuracy than the machine used to manufacture the template used in this experiment. The machined template should be measured by a CMM to decide if it is suitable for the bonding task. Next, the reference points should be aligned and bonded by use of a CMM and a bonding tool. The template can be used to place all non-crucial optical components, but the alignment of the template relative to the base plate should be controlled by a CMM for both repeatability and accuracy.

Quasi-monolithic fiber injectors were aligned in five degrees of freedom (expect for roll around the beam axis) and retrofit to an almost fully assembled base plate. Improvements for the construction and alignment of the next fiber injectors were presented. The first – to the author’s knowledge – fully bonded inter-table interferometer has been assembled with an contrast of 53 %.

Within this chapter the phase measurement system is characterized. This is followed by the determination of the sensitivity of the SPI. Methods for improvements are introduced. Next, measurements between the central and south table are presented and their longitudinal inter-table motion is stabilized.

7.1. Sensitivity of the phase meter

Before the start of the inter-table measurements the phase measurement system must be characterized. For this purpose its noise performance was investigated with electronic signals. A function generator was connected via a resistive splitter ($4.7\text{ k}\Omega$) to the input channels of the phase meter. The output of the function generator was a sine wave at the heterodyne frequency of 15773.423 Hz and an offset voltage of 1.1 V . Different signal amplitudes were used for this test: 900 mV , corresponding to an interferometric contrast of 0.81 , and 50 mV corresponding to a contrast of 0.045 . The phase meter was read out via different methods: first, slow readout via EPP, and second, fast readout via PMI and CDS.

The equivalent path length noise of the phase meter using EPP readout is for all frequencies well below the desired $100\text{ pm}/\sqrt{\text{Hz}}$; see the black colored line in Figure 7.1. The sensitivity was not degraded by using the PMI and CDS for readout; see the blue colored curve. Even for a small signal amplitude (orange curve) corresponding to an interferometric contrast of only 0.045 , the noise of the phase meter allows the measurement of $100\text{ pm}/\sqrt{\text{Hz}}$ for all frequencies of interest.

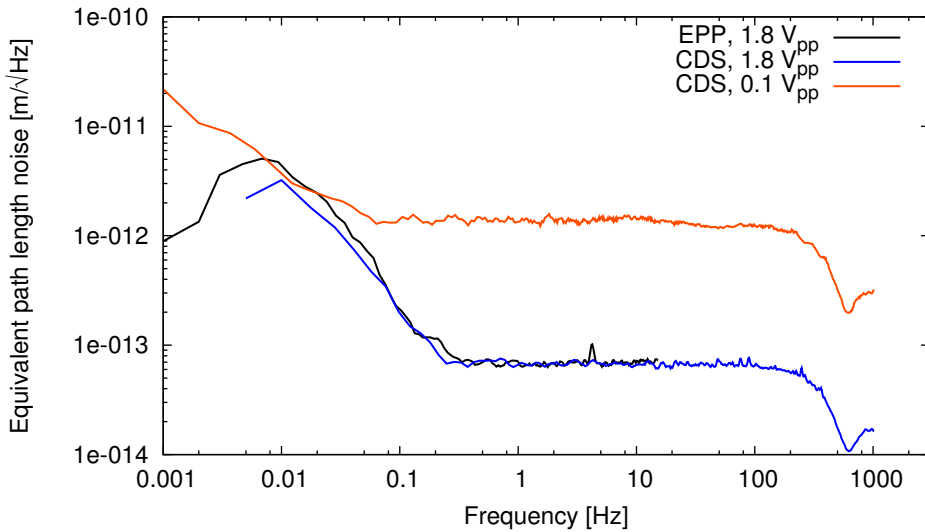


Figure 7.1.: Phase meter noise, expressed in equivalent path length noise, of the difference of two phase meter channels for different readout ports and signal levels. The displayed curve was taken from the channels with the highest noise relative to each other. For all curves a function generator and a resistive splitter were connected to the input channels of the phase meter. For readout via EPP the bin number was 500, for CDS readout the bin number was 25. An offset voltage of 1.1 V and a heterodyne frequency 15773.423 Hz were used for all measurements.

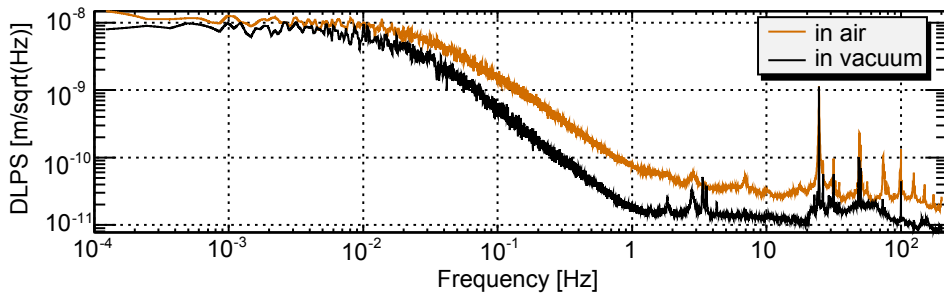


Figure 7.2.: Longitudinal path length difference of the diagnostic and reference interferometers which is twice the displacement noise. One measurement (brown colored curve) has been performed in a vented, but closed vacuum system. The other one (black curve) was in a vacuum environment of 10⁻² mbar.

7.2. Sensitivity of the SPI

The sensitivity of the SPI is given by the difference of the longitudinal path length signal of the two local interferometers, the diagnostic and reference interferometers, confined on the central table. This is referred to as the path length noise of the diagnostic interferometer. It differs from the path length noise measured by the south (minus reference) interferometer by a different response to laser frequency noise and that it does not measure any inter-table motion. Thus, the diagnostic interferometer is a good measure for the noise floor for SPI signals.

A spectral density of the diagnostic interferometer's path length noise is depicted in Figure 7.2. A measurement inside a closed, but vented vacuum system is shown in orange. For all frequencies above 0.5 Hz the diagnostic interferometer fulfills the requirement on the displacement noise. When the vacuum system is evacuated to 10^{-2} mbar the sensitivity is further increased. Here, from 0.2 Hz to higher frequencies the displacement noise is below $100 \text{ pm}/\sqrt{\text{Hz}}$.

The path length noise is not improved by the same amount at all frequencies. This is a sign of another noise source dominating the performance of the interferometers. A likely candidate is the optical path length difference noise, as the curves show a shoulder shape which is typical for this type of noise.

Optical path length difference noise [77; 108] is caused by additional optical sidebands that are imposed on the interferometer beams by the AOMs on the modulation bench. These optical sidebands are created by electrical sidebands in the RF driving signal applied to the AOMs. The optical sidebands generate a spurious beat signal at the photo diode leading to sideband induced noise. This is not canceled by the subtraction of the signals from two interferometers to derive a length measurement. It can be reduced by active stabilization [108, p.63]. The path length signal of the reference interferometer is compared with an electronic reference signal which originates from the same clock that the phase meter is locked to. The differential signal is used to actuate on a piezo glued to a mirror which is on the modulation bench in one interferometer arm. A detailed description of the optical path length difference noise is provided in [109; 85, p. 75-119]. Currently, it is not expected that the measurement of the relative inter-table motion will be limited by this noise source. The initial performance of the south interferometer will be dominated by the coupling of the motion of other degrees of freedom into path length signal of the south interferometer; see Section 7.3.1 on p. 106. Thus, the next experimental steps are the sensing and stabilization of the inter-table displacement.

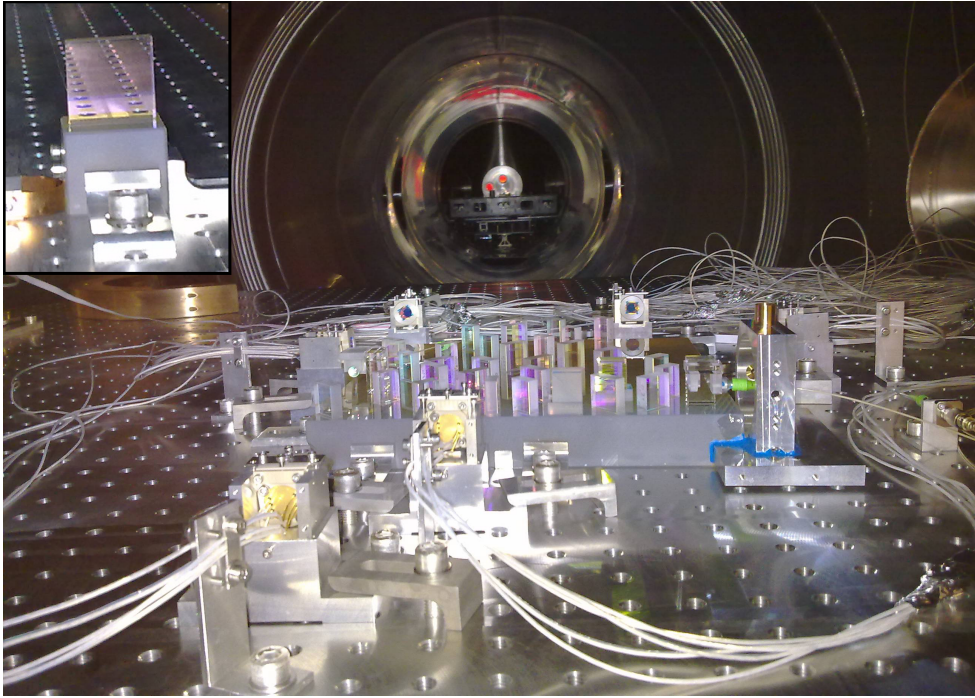


Figure 7.3.: This photograph shows the south arm of the SPI looking from the central table to the south tank. The upper left inset shows the curved mirror on the south table.

7.3. Measurement of seismic motion

The SPI is designed to measure the inter-table motion of two seismically isolated optical tables; see Figure 7.3. For the final construction step of the south interferometer the central table was clamped, *i.e.* the isolation stages were mechanically locked. Thus, the central table was no longer isolated from seismic noise. The south table was free, *i.e.* it is seismically isolated from ground motion above its natural frequencies. An inter-table measurement between a clamped table and a free one corresponds to a measurement of the seismic motion of the clamped table.

The inter-table displacement between the south and central tables measured in a vacuum environment of 10^{-2} mbar is depicted in dark blue in Figure 7.4. At low frequencies it is at least two orders of magnitude above the displacement detected by the diagnostic interferometer (orange colored curve) located only on the central table. The south interferometer senses the horizontal ground motion. The ground motion in y direction, *i.e.* along the south arm, is mea-

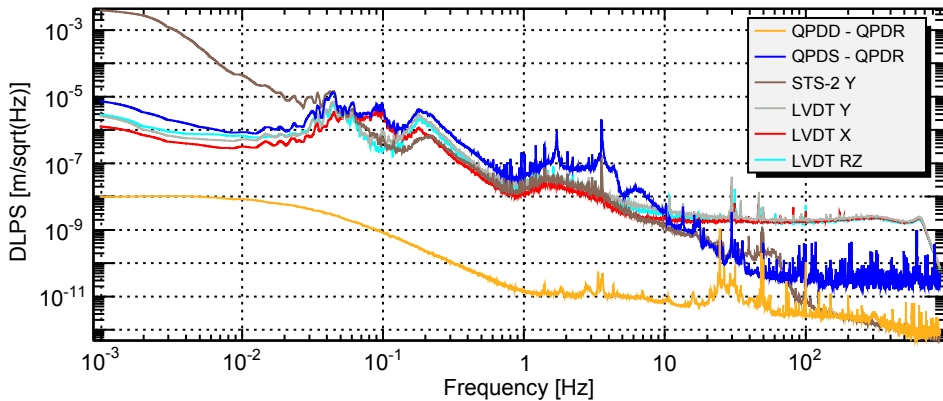


Figure 7.4.: Displacement signal of the inter-table motion with the south table free and the central table clamped. The sensed displacement by the SPI is depicted in the dark blue line. For comparison the measured path length noise of the diagnostic interferometer, being confined on the central table only, is plotted in orange. The inter-table interferometer measures the horizontal seismic motion of the ground. The output of the seismometer measuring the displacement along the south interferometer arm is plotted in brown. The horizontal LVDT signals are also displayed.

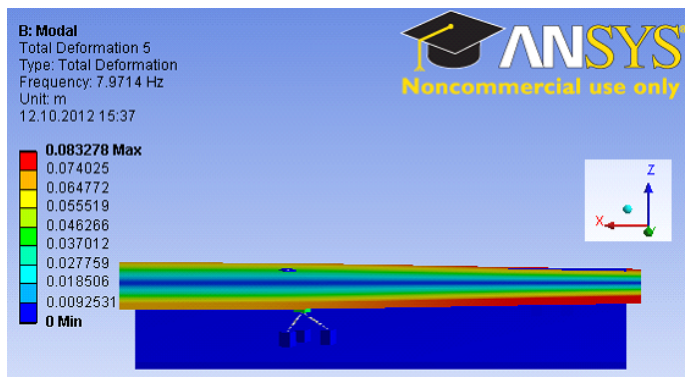


Figure 7.5.: Finite element simulation of an optical table sitting on Fluorel pads which are placed on top of the seismic attenuation system. For this simulation the seismic isolation was clamped, the configuration of the central table. The figure shows the fundamental pitch resonance mode about 8 Hz due to Fluorel between the table and the SAS. This simulation was kindly provided by Gerald Bergmann.

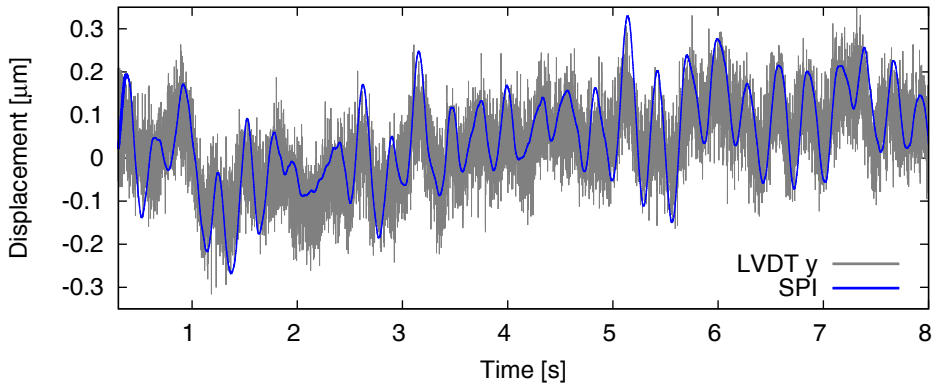


Figure 7.6.: Time series of SPI length and LVDT Y signal. For both signals the mean value was subtracted for better illustration.

sured by the STS-2 seismometer [110] and is depicted in brown. The measured peak around 0.15 Hz is the microseismic peak [11, p.129]. The peaks between 1 Hz and 10 Hz are due to human activity. It is likely that the peak around 8 Hz corresponds to eigenfrequencies of the table due to the Fluorel pads which are between the optical table and its seismic attenuation system; see Figure 7.5. The peak at 0.1 Hz is due to a lateral displacement of the table as this signal is also sensed by the LVDT in x direction. During the measurement it was not possible to monitor the resonances on the table top by an independent witness channel, because all LVDTs and seismometers are located within the SAS. Subsequently, a horizontal geophone was placed on top of each table with its sensing axes aligned along the y axis; see Section 7.3.2.

The time series of the longitudinal displacement signal detected by the SPI and the south table's LVDTs are depicted in Figure 7.6. For both curves the mean value has been removed. Both graphs are in phase, of the same sign, and are of about the same amplitude which confirms the good calibration of the LVDT sensor signals.

7.3.1. Measurement of coupling factors

In order to diagonalize the servo system the coupling factors between the signal applied to the LVDT and the signal sensed by the SPI are of interest for all degrees of freedom. For the determination of the coupling factors the south table was displaced in one degree of freedom by applying a slow excitation signal to the LVDTs slowly enough not to excite any eigenfrequencies of the

Table 7.1.: Measured coupling factors for the south interferometer. The coupling factor designed to be the strongest for the excited degree of freedom is colored in orange.

	DLPS	DWS _h	DWS _v	DPS _h	DPS _v
	$\left[\frac{\mu\text{m}}{\mu\text{m}}\right]$	$\left[\frac{\text{rad}}{\mu\text{m}}\right]$	$\left[\frac{\text{rad}}{\mu\text{m}}\right]$	$\left[\frac{\mu\text{m}}{\mu\text{m}}\right]$	$\left[\frac{\mu\text{m}}{\mu\text{m}}\right]$
x	0.60	0.03	0.01	-7.62	-0.76
y	1.94	–	–	-6.93	-1.12
z	–	–	0.00	–	1.65
	$\left[\frac{\mu\text{m}}{\mu\text{rad}}\right]$	$\left[\frac{\text{rad}}{\mu\text{rad}}\right]$	$\left[\frac{\text{rad}}{\mu\text{rad}}\right]$	$\left[\frac{\mu\text{m}}{\mu\text{rad}}\right]$	$\left[\frac{\mu\text{m}}{\mu\text{rad}}\right]$
Rx	-1.22	–	0.04	–	-10.55
Ry	–	–	0.00	–	-0.51
Rz	3.74	0.21	0.02	-10.00	-4.09

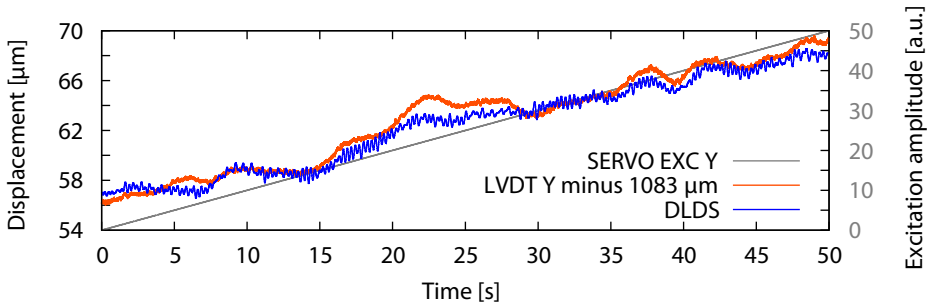


Figure 7.7.: Measurement of the coupling factor from y direction to the DLDS signal. A linear excitation (gray colored line) in y direction was applied to the horizontal LVDTs. The resulting displacement of the LVDTs in y direction is depicted in orange. The displacement signal detected by the SPI is shown in blue. For the determination of the coupling factor a line was fitted to both displacement curves and the slope of the SPI signal was divided by the slope of the LVDT signal. For a better display of the graphs an offset of 1083 μm was subtracted from the LVDT signal.

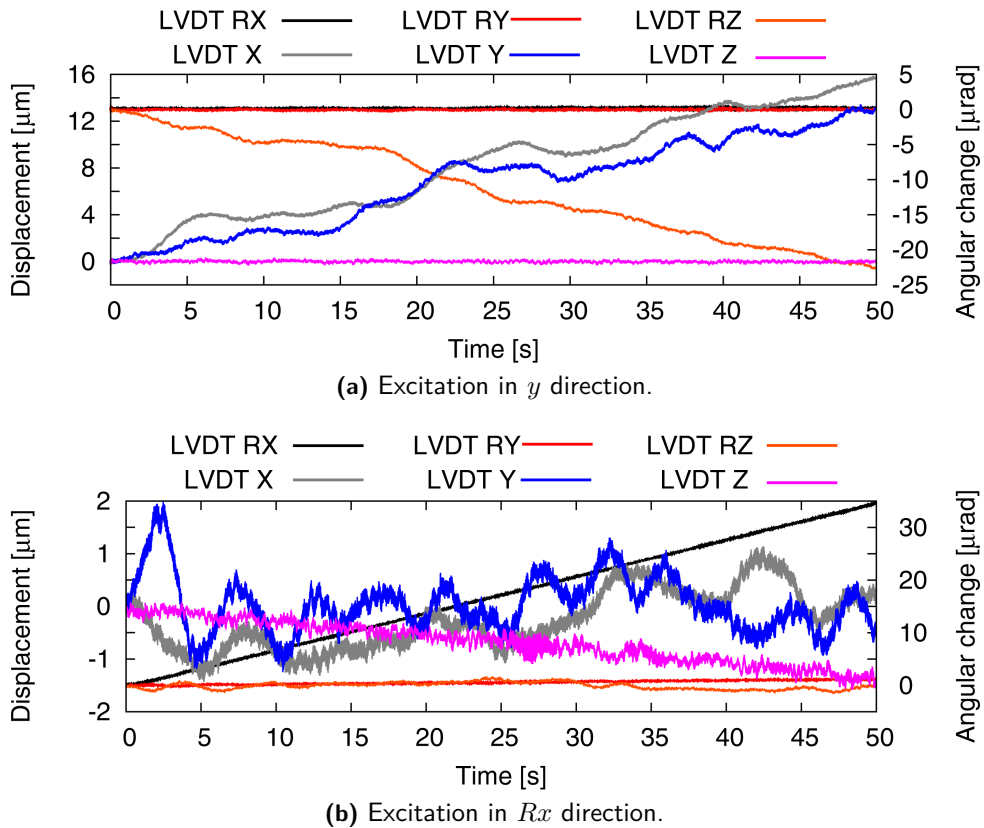


Figure 7.8.: Sensed signals of the LVDTs in the south table when an excitation in y direction [Figure (a)] or Rx [Figure (b)] is applied. The LVDTs labeled with R belong to a change in angle. The horizontal LVDTs (X, Y, RZ) are located on a circle with radius 787 mm from the table center. The radius for the vertical LVDTs (RX, RY, Z) is 525 mm. Hence, 1 μrad is of order 1 μm . Figure (a) shows that an excitation in y results in a motion in all horizontal degrees of freedom. The vertical degrees of freedom are better decoupled; see Figure (b). Here the change in the desired degree of freedom is at least an order of magnitude larger than the change in all other degrees of freedom.

table¹. In parallel the inter-table motion was monitored with the SPI. An exemplary measurement of a coupling factor is depicted in Figure 7.7. For the calculation of the coupling factor a linear function was fitted to the detected SPI and LVDTs signals. Their slopes were divided by each other. Table 7.1 summarizes the most important numbers. A dash (–) denotes that the SPI’s or LVDT’s signal had no linear slope. In orange the coupling factors are highlighted which are designed to measure the according displacement/angular misalignment. The coupling factor from longitudinal displacement to the SPI’s DLPS signal is with 1.94 in good agreement with the simulated values of 1.99986; *cf.* Table 5.1 on p. 64. Furthermore, this shows the good calibration of the LVDT sensor signals.

The coupling factor from a rotation around R_x (pitch) to the longitudinal length signal differs by a factor of 1.5 from the simulated value for which the table’s pivot point was only estimated; see Section 5.1.3 on p. 62. The coupling factor for the yaw (R_z) degree of freedom to the length signal is three orders of magnitude larger than the computed value. The reason for this may be that the LVDT actuators are not well diagonalized such that no pure rotation in yaw is realized but instead a combined table motion consisting of a rotation around the R_z axis and a displacement y direction. The matrix diagonalization of the LVDT actuators has to be improved in future.

The measurements of the coupling factors showed that the LVDTs in the vertical plane are much better decoupled than the LVDTs in the horizontal plane; see Figure 7.8a and Figure 7.8b. For example, for the measurement presented in Figure 7.7 an excitation in y direction was applied. This resulted in a change of the table position in x , y , and R_z by approximately the same amount; see Figure 7.8a. In future, the decoupling of the horizontal LVDTs has to be improved to enable a good operation of the inter-table stabilization. Nevertheless, an attempt was made to stabilize the longitudinal relative inter-table motion.

7.3.2. Inter-table distance stabilization

For the stabilization of the relative longitudinal inter-table displacement a control loop is required. The length signal of the SPI’s south interferometer is used as a sensor and the three horizontal voice-coil actuators in the south table serve as actuators. For two reasons the feedback is currently only applied to the south table: firstly, the central table is still clamped and thus, its actuators cannot be used. Second, in the beginning it is easier to regard one (the central) table as reference and to act only on the remote table. The dynamic range of

¹This measurement was performed by Sina Köhlenbeck.

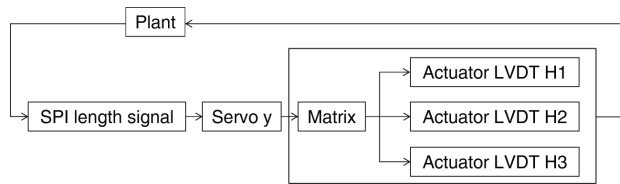


Figure 7.9.: Sketch of the relative longitudinal inter-table control. The SPI length signal senses the inter-table displacement. Within the servo for the y direction a feedback signal is generated which is multiplied by a matrix so that three feedback signals for the three horizontal LVDT actuators are created.

the actuators is large enough to allow this simplification. At a later stage it will be beneficial to split the feedback signal and to actuate on both tables. This minimizes the chance of railing an actuator of a table.

The structure of the control model for the stabilization of the relative longitudinal inter-table motion is depicted in Figure 7.9. Since no single LVDT actuator designated for the y direction exists (see Figure 2.7 on p. 15), the feedback is applied to all three horizontal actuators. The design of the servo is presented in Figure 7.10.

Figure 7.11 shows the displacement noise when the relative longitudinal motion between the central and south stables is stabilized using the SPI length signal as a sensor. The other five degrees of freedom of the south table were kept constant at their position using the LVDTs as sensor and actuator. The stabilized SPI length signal (blue colored curve) is at low frequencies well below the measured inter-table motion in the non-stabilized case; see red colored curve. As the central table is still clamped, *i.e.* it follows the ground motion. Hence, the south table is now forced to follow the ground motion. This can be seen in the black colored curve in Figure 7.11 which shows the seismic motion of the ground along the south arm measured by the Streckeisen seismometer STS-2 [110]. In case of one table being clamped, the LVDT signal (green colored curve) of the free table serves as a measure of the relative inter-table motion assuming that both tables are exposed to the same ground motion. From 0.5 Hz to 3 Hz both signals are of the same value as the SPI signal. For lower frequencies the LVDTs appear to be a more suitable sensor than the STS-2 seismometer. For frequencies above 3 Hz neither the STS-2 nor the LVDT is a good sensor for the inter-table motion. Here, the combined signal of the two horizontal geophones is a better measurement tool; see gray curve. A geophone (L-4C from Mark Products [111]) is placed on the top and close to the center of each table. They are sensitive for displacements along the south arm. Their signals have been subtracted from each other and

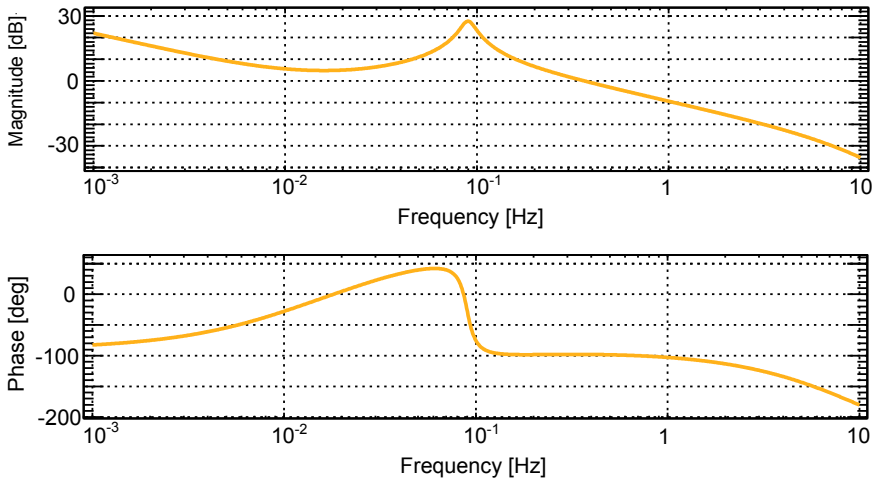


Figure 7.10.: Modeled open loop transfer function and the according phase of the whole loop consisting of servo and plant of the y direction. The servo has an open loop gain of 26.5 dB at 0.09 Hz and 22 dB at 0.001 Hz. It consists of a filter to damp the tables fundamental resonance at 0.09 Hz and an integrator used to keep the table at the set point. The damping filter has a zero at 0.01 Hz, two poles at 10 Hz, and a gain of 8 dB. The integrator has a zero at 0.03 Hz, a pole at 0 Hz, and a gain of -30 dB.

Fourier transformed. Since the geophones and the SPI are both placed on the table tops, both devices monitor besides the pure longitudinal length signal a contribution which is due to coupling from other degrees of freedom. For example, the peak around 8 Hz is likely to be due to a pitch motion of the table caused by the fundamental modes of Fluorel pads supporting the optical table; see Figure 7.5. The peak at 13 Hz is from a horizontal resonance of the spring box [48, p.116]. For frequencies below 1 Hz the tilt motion of the table couples much stronger into the geophone signal than above 1 Hz. Hence, below 1 Hz the geophone signal (gray curve in Figure 7.11) may be dominated by this coupling from tilt motion and thus, cannot be used as an independent witness sensor below 1 Hz. Above 35 Hz the geophone signals are not useful.

7.4. Measurements between seismically isolated tables

The stabilization of the longitudinal inter-table motion with the central table being clamped was successfully demonstrated. Next, the central table was freed to first, measure and second, stabilize the relative displacement between two seismically isolated platforms.

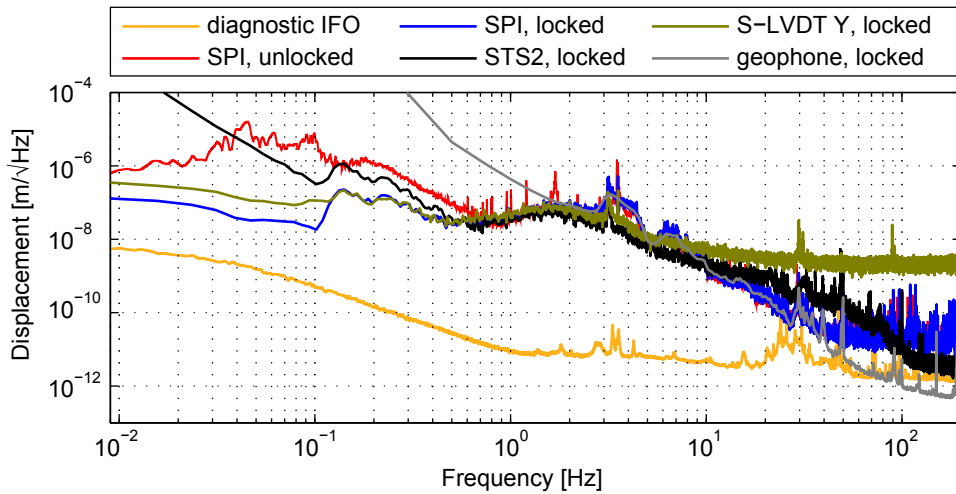


Figure 7.11.: Displacement noise measured between the south and clamped central table when the relative longitudinal motion is not stabilized (red colored curve) and stabilized using the SPI length signal. The in-loop measured length signal of the SPI is depicted in blue. An out-of-loop signal is provided by the combined signal of two horizontal geophones placed on top of each table; see gray colored line. The green colored line is the signal in longitudinal direction sensed by the south table's horizontal LVDTs. The black colored curve shows the signal of the seismometer STS-2 along the south arm. The STS-2 is placed outside of the vacuum system, on the ground next to the central tank. The orange colored curve depicts the displacement noise of the diagnostic interferometer which is equivalent to the sensing noise of the SPI. The inter-table displacement could be suppressed at all frequencies below 1 Hz by using the SPI signals as a sensor.

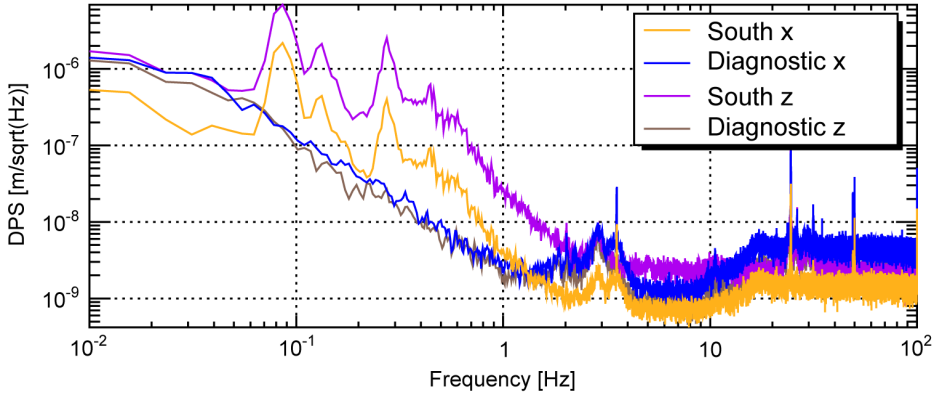


Figure 7.12.: Angular displacement noise of the south and diagnostic interferometers measured in a closed, but vented vacuum system. The differential power sensing (DPS) signals monitor the displacement of the beam centroid in the vertical (z) and horizontal (x) axes.

The relative angular displacement of the two tables is depicted in Figure 7.12 (yellow and violet colored curves). The differential power sensing (DPS) signals monitor the position of the beam centroid on a quadrant photo diode on the central table. These signals provide information on the relative angular misalignment of the tables. They have a broader measurement range than the DWS signals. A DPS signal of $0.12 \mu\text{m}/\sqrt{\text{Hz}}$ corresponds to $10 \text{ nrad}/\sqrt{\text{Hz}}$ which is the angular noise design goal of the SPI for all frequencies above 10 mHz. This goal is already met without any stabilization for all frequencies above 0.3 Hz for the pitch motion and above 0.7 Hz for misalignments in the yaw degree of freedom. The misalignment in pitch is a factor of five above the motion in yaw.

The longitudinal inter-table displacement between the two seismically isolated tables is depicted in the red colored curve of Figure 7.13. At all frequencies the measured displacement is (as expected) smaller than in the configuration with the central table being clamped (see red colored curve in Figure 7.11 on p. 112) since both tables are isolated from seismic motion. As the signal is no longer dominated by ground motion the resonance frequency of the inverted pendulum is detected at 0.1 Hz [48, p.75].

The combined signal of the geophones which are placed close to the center and on the top of each table matches the SPI signal only above 10 Hz. For lower frequencies their signal might be dominated by coupling from tilt motion because on the one hand the pure longitudinal motion is in this configuration

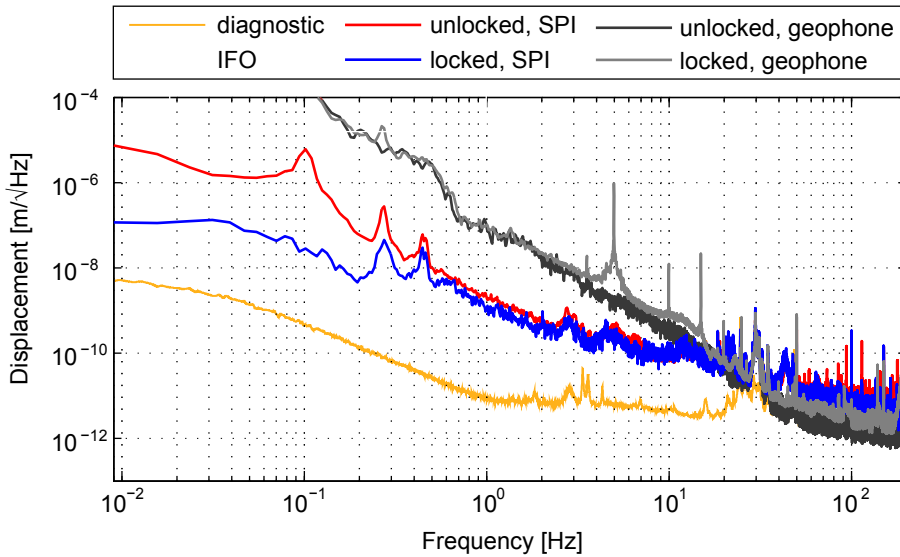


Figure 7.13.: Displacement noise measured between two seismically isolated (free) tables. The red colored curve shows the longitudinal inter-table motion sensed by the SPI without stabilizing this displacement. The combined signal of the geophones (dark gray colored curve) which are on top of each table senses this motion, too. For frequencies below 10 Hz it may be dominated by tilt coupling into longitudinal displacement. This effect dominates the geophone signals such that they do not match the SPI readout. The SPI displacement signal was used to stabilize the relative longitudinal motion of the two tables (see blue colored curve). The orange colored curve shows the SPI sensing noise. The inter-table displacement is suppressed at all frequencies below 1 Hz by using the SPI signals as a sensor.

with a free, seismically isolated table smaller than with one clamped table. On the other hand, the pivot point (see Figure 5.6a on p. 62) of a free table is further away from the table top resulting in a longer lever arm. Thus, the tilt motion may dominate the geophone signals. Hence, they cannot be used as independent witness sensor of the longitudinal inter-table displacement below 10 Hz.

The same control loop as described previously was used to stabilize the displacement between the two seismically isolated tables. The longitudinal displacement was reduced for all frequencies below a few hertz; see blue colored curve. At 0.1 Hz the longitudinal inter-table motion was reduced by two orders of magnitude which is best suppression of the longitudinal inter-table motion. The performance is not yet limited by the sensing of the SPI; *cf.* orange colored

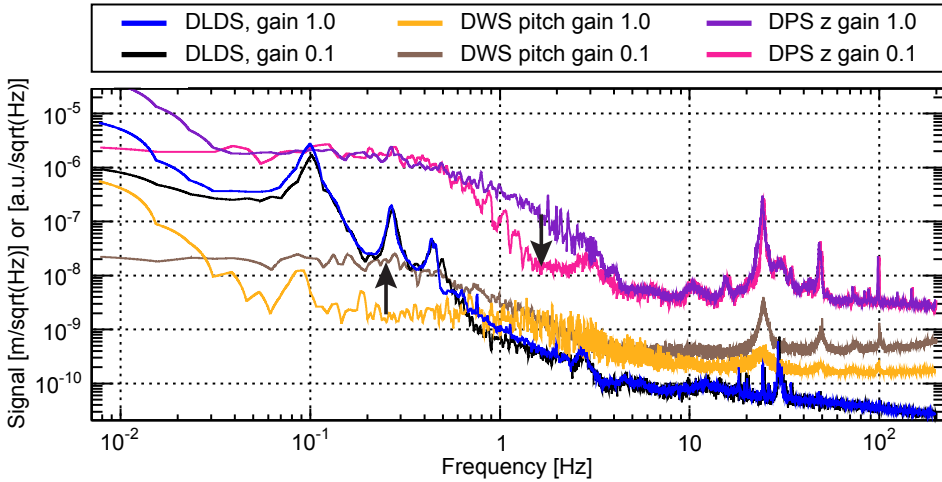


Figure 7.14.: Impact of servo gain on open-loop SPI signals of the south interferometer. DLDS denotes the longitudinal displacement signal. DPS z is the position of the beam centroid on the quadrant photo diode in vertical direction. The DWS signals are in arbitrary units of $\text{a.u.}/\sqrt{\text{Hz}}$. The displacement and DPS signals are in units of $\text{m}/\sqrt{\text{Hz}}$. As indicated by the arrows, the servo gains have to be carefully optimized to improve the measured displacement.

curve in Figure 7.2 on p. 102. Furthermore, the performance is not yet limited by laser frequency noise of the free-running laser. The expected path length noise due to laser frequency noise is $100 \text{ nm}/\sqrt{\text{Hz}}$ at 0.01 Hz and $1 \text{ nm}/\sqrt{\text{Hz}}$ at 10 Hz for an interferometer with 23 m arm length mismatch and laser frequency noise of a free-running laser of $10 \text{ kHz}/\sqrt{\text{Hz}}/f$. Although the curve of the stabilized inter-table displacement is close to that limitation, a measurement with active stabilization of the laser frequency confirmed that this is currently not the dominating noise source.

It is very likely that angular motion of the table couples into the length signal. The contribution of the angular motion to the length signal can be calculated by multiplying the coupling factor from angular motion to the SPI length signal (about $-10 \mu\text{m}/\mu\text{rad}$ for pitch and yaw; see Table 7.1 on p. 107) with the measured DPS signals (see Figure 7.12 on p. 113). The results are far above the detected longitudinal displacement signal. This might be due to two reasons: first, the south interferometer might have been aligned differently compared to the configuration when the coupling factors were determined. Second, the coupling of angular table motion to the length signal of the SPI can be different when both tables are free in contrast to the case when one table is free and the other is clamped. The coupling might also be much more

complex such that it is not sufficiently described by only one linear coupling factor. In the future, this coupling must be studied in more detail to further improve the suppression of the inter-table motion.

One possibility to further minimize the longitudinal relative motion between the tables is to implement the stabilization of the angular degrees of freedom. It is expected that a reduction of the angular motion will further reduce the relative longitudinal table displacement.

Another tool to improve the suppression of the inter-table motion is to optimize the servo gains, because an excessive servo gain induces additional noise in the interferometer. Figure 7.14 shows an example how the interferometer signals in an open-loop measurement are effected by the servo gain. On the one hand, the noise in the DPS signal in the vertical directions (z) could be reduced at frequencies of a few hertz by reducing the servo gain by a factor of ten. On the other hand, the noise of the DWS pitch signal is increased at all frequencies by decreasing the gain. The displacement signal is slightly improved with a lower gain. This example shows, that the servo gains have to be carefully adapted to optimize the sensitivity of all interferometer signals.

7.5. Conclusion

In this chapter, the phase measurement system was characterized and qualified using electronic signals. Its equivalent path length noise is well below the requirement of $100 \text{ pm}/\sqrt{\text{Hz}}$ at all frequencies and for all interferometric contrasts above 0.045. The sensitivity of the SPI was presented which is currently $10 \text{ nm}/\sqrt{\text{Hz}}$ at 10 mHz for longitudinal displacement. The design goal of $100 \text{ pm}/\sqrt{\text{Hz}}$ is met for frequencies above 0.5 Hz for operation in air and above 0.2 Hz for operation in a vacuum environment of 10^{-2} mbar.

The longitudinal inter-table motion was measured and stabilized in two configurations both with a free, seismically isolated south table. In the first configuration, the central table was clamped such that the seismic isolation stages were mechanically locked and the table followed the ground motion. In the second arrangement, the central table was free, *i.e.* seismically isolated.

With the central table being clamped, the open-loop measurement showed that the SPI's longitudinal displacement signal nicely follows the seismic motion. By closing the loop, the south table was forced to follow the ground motion and thus suppressing the relative inter-table motion for frequencies below a few hertz. It was demonstrated that the SPI's length signal and the signal of the LVDT actuators along the south arm (y direction) are of the same sign, amplitude, and phase. However, while actuating on the LVDTs in the y direction the cross-coupling to the other horizontal degrees of freedom

(x and Rz) are about the same amount as the coupling to the y direction. In the future, this will need to be minimized to improve the stabilization of the various degrees of freedom.

The longitudinal displacement between two seismically isolated tables was measured by the SPI. This signal was used to stabilize the tables with respect to each other reducing the residual inter-table motion for all frequencies below 1 Hz. For frequencies below 0.2 Hz this motion was suppressed by more than one order of magnitude. This performance is yet not limited by the sensor—the SPI—itself. It seems to be gain limited and the angular degrees of freedom have to be stabilized to minimize cross-coupling to the longitudinal displacement signal.

Thesis conclusion and outlook

This thesis introduced, from concept to operation, a suspension platform interferometer (SPI), which will be able to measure and subsequently stabilize the relative inter-table motion between three platforms separated by about 11 m in the longitudinal and angular degrees of freedom. The SPI consists of four heterodyne Mach-Zehnder interferometers whose signals are used to create a single inertially-quiet rigid platform via feedback to the table's actuators.

Within this thesis the optical layout of the SPI has been designed considering the minimization of cross-coupling of angular motion into the longitudinal displacement signal. Simulations of interferometer alignment including cross-coupling of the tables' different degrees of freedom to the interferometer signals were presented.

The interferometer optics were bonded on an ultra-low expansion base plate with a footprint of 250 mm \times 250 mm using the technique of hydroxide-catalysis bonding. The positioning accuracy of the silicate bonded components was analyzed and error sources were identified. The setup was retrofitted with quasi-monolithic fiber injectors resulting in a fully quasi-monolithic setup made only out of glass. So far, three out of four interferometers are fully operational. The fourth interferometer will be operational after the installation of the west table.

The sensitivity of the SPI is currently 10 nm/ $\sqrt{\text{Hz}}$ at 10 mHz for longitudinal displacement improving to 20 pm/ $\sqrt{\text{Hz}}$ at 1 Hz. The design goal of 100 pm/ $\sqrt{\text{Hz}}$ is met for frequencies above 0.5 Hz for operation in air and above 0.2 Hz for operation in a vacuum environment of 10^{-2} mbar. For all frequencies below 1 Hz a suppression of the longitudinal inter-table motion of more than 3 dB was achieved and below 0.2 Hz of more than 20 dB. So far, the best

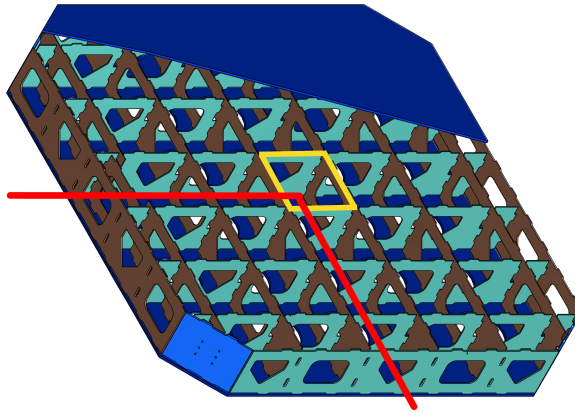


Figure 8.1.: The suggested position of an improved SPI would be inside the center of the optical table (marked with a yellow frame). One segment has the dimensions of $250\text{ mm} \times 250\text{ mm}$. The beam (depicted in red) could propagate through the holes in the reinforcement structure. The SPI could be accessed by a cut-out of the top plate of the optical table which would be bolted down to the reinforcement structure.

reduction of 46 dB of the longitudinal displacement was measured at 0.1 Hz.

Next steps are the optimization of the servo gains and diagonalization of the matrix transforming a signal in the horizontal plane of the prototype's coordinate system (which is also used by the SPI) to the coordinate system of the three horizontal LVDTs (see Figure 7.9 on p. 110). This will reduce the cross-coupling within the horizontal degrees of freedom. Moreover, the stabilization of the angular inter-table motion has to be implemented. At some point, the task of actuation should be assigned to both tables to minimize the inertial motion. Furthermore, active stabilization of the optical path length difference noise must be implemented to further increase the sensitivity of all SPI interferometers at frequencies below 1 Hz. This work has already started. When the west table is installed, the assembly of the SPI's west interferometer can be finalized and the control scheme of the south arm can be also implemented for the west arm.

In retrospect and with the knowledge that quasi-monolithic fiber injectors are used, *i.e.* no re-alignment of the local interferometers is necessary, it would have been beneficial to place the SPI not on the table tops but inside the optical tables; see Figure 8.1. This would decrease the height between the beam axis of the SPI and the pivot point of the table from 391 mm to 147 mm. This would significantly lower the coupling from pitch motion to the longitudinal path length signal. It would also be advantageous for all other experiments

to be performed within the AEI 10 m prototype because more space would be available on top of the central table as it would avoid all restrictions on placing optical components and routing beams on the table top.

A strong suppression of the longitudinal inter-table displacement has been demonstrated. The SPI is a great tool to minimize the residual relative motion between the seismically isolated platforms and will allow the AEI 10 m prototype to realize its goal of providing an ultra-low displacement noise facility for various kinds of experiments.

 Nominal optical setup

A.1. Optocad file of the simplified setup

This is the Optocad file of the simplified optical layout of the SPI which has been used for various simulations; see Chapter 5, p. 55. The dimensions are in meters and degrees. A sketch of this simplified setup is depicted in Figure 5.1, p. 56.

```

! Reference beam
b x=-0.319184, y=0.00094558, w=0.00105111, ag=-0.169738,
  c=-0.0141253, p=1
! Measurement beam
b x=0.277175, y=0.0695709, w=0.00105111, ag=-179.83, c=-0.0141253,
  p=1
! Refractive index of the remote mirror substrate
x n=1, rix=(/1.44963/)
! Remote mirror
d srt, x=-11.6033, y=0.0343749, rd=0.015, ag=-180, c=-0.0845309,
  r=0.98, t=0.02, m=1
+ t, dx=0.007, da=180, c=0, r=0, t=1
! Photo diode
c d, x=0, y=0, rd=0.007, ag=-0.169738
  
```

A.2. Optocad file of the full setup

The Optocad file shows the design position, dimensions, and parameters of the beams and optical components of the SPI. These have been used for simulations (see Chapter 5, p. 55) and to construct the SPI. All dimensions are

in meters. All angles are in degrees. A graphical output of this Optocad file is depicted in Figure 4.15, p. 48.

! Reference beam

b x=0.10873005, y=0.12, w=0.00105, z=0.15, ag=180.0, p=1.

! Measurement beam

b x=-0.14126996, y=0.12, w=0.00105, z=0.15, ag=0.0, p=1.

x n=1, rix=(/1.44963000/)

! Beam recombiner

d {srt}, x=0.01473403, y=0.09191255, rd=0.01, ag=135.0, c=0.0,
 r=0.49, t=0.49, m=1 #BR1
 + {t}, dx=0.007, da=180.0, c=0.0, r=0.01, t=0.98

d {srt}, x=-0.02236252, y=0.05481600, rd=0.01, ag=135.0, c=0.0,
 r=0.49, t=0.49, m=1 #BR2
 + {t}, dx=0.007, da=180.0, c=0.0, r=0.01, t=0.98

d {srt}, x=-0.04236237, y=0.0, rd=0.01, ag=135.0, c=0.0, r=0.49,
 t=0.49, m=1 #BR3
 + {t}, dx=0.007, da=180.0, c=0.0, r=0.01, t=0.98

d {srt}, x=-0.0, y=-0.08263731, rd=0.01, ag=-45.0, c=0.0, r=0.49,
 t=0.49, m=1 #BR4
 + {t}, dx=0.007, da=180.0, c=0.0, r=0.01, t=0.98

! Beam splitter

d {srt}, x=0.04439741, y=0.07661712, rd=0.01, ag=-135.0, c=0.0,
 r=0.49, t=0.49, m=1 #BS1
 + {t}, dx=0.007, da=180.0, c=0.0, r=0.01, t=0.98

d {srt}, x=0.03944767, y=0.05561710, rd=0.01, ag=-45.0, c=0.0,
 r=0.49, t=0.49, m=1 #BS2
 + {t}, dx=0.007, da=180.0, c=0.0, r=0.01, t=0.98

d {srt}, x=0.01335115, y=0.05838286, rd=0.01, ag=-135.0, c=0.0,
 r=0.49, t=0.49, m=1 #BS3
 + {t}, dx=0.007, da=180.0, c=0.0, r=0.01, t=0.98

d {srt}, x=-0.09488708, y=0.12138288, rd=0.01, ag=-45.0, c=0.0,
 r=0.49, t=0.49, m=1 #BS4
 + {t}, dx=0.007, da=180.0, c=0.0, r=0.01, t=0.98

d {srt}, x=-0.06917157, y=0.11643313, rd=0.01, ag=45.0, c=0.0,
 r=0.49, t=0.49, m=1 #BS5
 + {t}, dx=0.007, da=180.0, c=0.0, r=0.01, t=0.98

```
d {srt}, x=-0.02097964, y=0.09271366, rd=0.01, ag=-135.0, c=0.0,
  r=0.49, t=0.49, m=1 #BS6
+ {t}, dx=0.007, da=180.0, c=0.0, r=0.01, t=0.98
```

```
d {srt}, x=-0.07193668, y=-0.03556215, rd=0.01, ag=-45.084572,
  c=0.0, r=0.49, t=0.49, m=1 #BS7
+ {t}, dx=0.007, da=180.0, c=0.0, r=0.01, t=0.98
```

```
d {srt}, x=-0.00138288, y=-0.00356686, rd=0.01, ag=135.0, c=0.0,
  r=0.49, t=0.49, m=1 #BS8
+ {t}, dx=0.007, da=180.0, c=0.0, r=0.01, t=0.98
```

! Mirrors

```
d r, x=-0.02136252, y=0.119, rd=0.00750, ag=45.0, c=0.0, r=1, t=0,
  m=1 #M1
+ d, dx=0.007, da=180.0, c=0.0, r=0, t=0
```

```
d r, x=0.04201454, y=0.119, rd=0.00750, ag=135.0, c=0.0, r=1, t=0,
  m=1 #M2
+ d, dx=0.007, da=180.0, c=0.0, r=0, t=0
```

```
d r, x=-0.02236252, y=-0.02518400, rd=0.0075, ag=-135.0, c=0.0,
  r=1, t=0, m=1 #M3
+ d, dx=0.007, da=180.0, c=0.0, r=0, t=0
```

```
d r, x=-0.04454636, y=0.03426077, rd=0.0075, ag=45.084572, c=0.0,
  r=1, t=0, m=1 #M4
+ d, dx=0.007, da=180.0, c=0.0, r=0, t=0
```

```
d r, x=-0.06837649, y=-0.10689736, rd=0.0075, ag=-135.0, c=0.0,
  r=1, t=0, m=1 #M5
+ d, dx=0.007, da=180.0, c=0.0, r=0, t=0
```

```
d r, x=-0.03419639, y=-0.10689736, rd=0.0075, ag=45.084869, c=0.0,
  r=1, t=0, m=1 #M6
+ d, dx=0.007, da=180.0, c=0.0, r=0, t=0
```

```
d r, x=0.03426179, y=-0.08482130, rd=0.0075, ag=44.915131, c=0.0,
  r=1, t=0, m=1 #M7
+ d, dx=0.007, da=180.0, c=0.0, r=0, t=0
```

```
d r, x=-0.04236237, y=-0.06200000, rd=0.0075, ag=-135.0, c=0.0,
  r=1, t=0, m=1 #M8
+ d, dx=0.007, da=180.0, c=0.0, r=0, t=0
```

```
d r, x=-0.09707803, y=0.05699998, rd=0.0075, ag=135.0, c=0.0, r=1,
  t=0, m=1 #M9
+ d, dx=0.007, da=180.0, c=0.0, r=0, t=0
```

Appendix A. Nominal optical setup

```
d r, x=0.00218399, y=-0.10535281, rd=0.0075, ag=-135.0, c=0.0,
  r=1, t=0, m=1 #M10
+ d, dx=0.007, da=180.0, c=0.0, r=0, t=0

d r, x=0.04301453, y=-0.00218398, rd=0.0075, ag=-45.0, c=0.0, r=1,
  t=0, m=1 #M11
+ d, dx=0.007, da=180.0, c=0.0, r=0, t=0

d r, x=0.06473403, y=0.09191255, rd=0.0075, ag=-45.0, c=0.0, r=1,
  t=0, m=1 #M12
+ d, dx=0.007, da=180.0, c=0.0, r=0, t=0

d r, x=0.09601453, y=0.078, rd=0.0075, ag=45.0, c=0.0, r=1, t=0,
  m=1 #M13
+ d, dx=0.007, da=180.0, c=0.0, r=0, t=0

d r, x=0.09601453, y=0.008, rd=0.0075, ag=-135.0, c=0.0, r=1, t=0,
  m=1 #M14
+ d, dx=0.007, da=180.0, c=0.0, r=0, t=0

! Remote mirrors
d r, x=-11.65, y=0.0, rd=0.015, ag=-180.0, c=-0.0845309, r=1, t=0,
  m=1 #MW
+ d, dx=0.007, da=180.0, c=0.0, r=0, t=0

d r, x=0.0, y=-11.65, rd=0.015, ag=-90.0, c=-0.0845309, r=1, t=0,
  m=1 #MS
+ d, dx=0.007, da=180.0, c=0.0, r=0, t=0

! Alignment mirror
d srt, x=-0.003, y=0.1195, rd=0.00750, ag=0.0, #MA
+ t, dx=0.007

! MB are mirrors to align the bonding template
! no beam hits these mirrors
d r, x=-0.10495, y=0.0949497, rd=0.00750, ag=-45.0, #MB1
+ d, dx=0.007

d r, x=0.0643431, y=0.0257574, rd=0.00750, ag=-45.0, #MB2
+ d, dx=0.007

d r, x=0.0150503, y=-0.0399497, rd=0.00750, ag=-45.0, #MB3
+ d, dx=0.007
```

Table A.1.: Nominal optical arm length of SPI interferometers. The distance is computed from beam start to the beam recombiner.

Interferometer	Beam	Length [mm]
Diagnostic	Reference	199.726
Diagnostic	Measurement	199.726
Reference	Reference	193.633
Reference	Measurement	193.633
South	Reference	319.185
South	Measurement	23483.976
West	Reference	285.002
West	Measurement	23449.794

A.3. Interferometer arm length

The optical path length of the individual interferometer arms is displayed in Table A.1.

IFOCAD coordinates of the bonded setup

Appendix B summarizes the dimensions of the footprint of all bonded and optically contacted optical components. It also lists the position of the center and the normal vector of their primary surface. The outer dimensions of each substrate have been measured with a CMM as described in Chapter 6, p. 73. The CMM output for the angular alignment of a component is the angle between a front surface of a component and a plane of the base plate. This value needs to be converted into a normal vector of the front surface of the optical component to be able to use the simulation tool IFOCAD. The beam coordinates of the measurement beam (bm) and the reference beam (br) have been determined using a CQP. The output of the CMM as well as the CQP output has been transferred into the coordinate system of the AEI 10m prototype. The origin of this coordinate system is the midpoint of the surface of the optical table inside the central tank. With the x -axis pointing Eastwards and the y -direction pointing Northwards. For the sake of completeness the beam parameters of the fiber injector optical subassembly (FIOS) are mentioned here. They have been built and characterized within a bachelor thesis[104].

```
// Beam waist size and waist position in mm
bm.set_qt_waist_rad(0.942985, -1104.4); // FIOS1
bm.set_qs_waist_rad(0.990012, -449.85);
br.set_qt_waist_rad(1.030815, -286.53); // FIOS2
br.set_qs_waist_rad(1.024740, -48.05);

// Beam direction
br.set_direction_xyz( 0.00000, .999869, 0.000107);
bm.set_direction_xyz(0.99998, -0.00592, 0.001054);
```

```

// Polarising beam splitter
Beamsplitter pbs;
pbs.set_thickness(7.327);
pbs.set_substrate_radius(10.061);
pbs.set_center_xyz(96.15,118.464,0);
pbs.set_nv_xyz(-1,-.99391,0);

// Mirrors
Beamsplitter m1;
m1.set_thickness(7.559);
m1.set_substrate_radius(7.542);
m1.set_center_xyz(-21.011,119.282,0);
m1.set_nv_xyz(-1,-.986478,0);

Beamsplitter m2;
m2.set_thickness(7.108);
m2.set_substrate_radius(7.5795);
m2.set_center_xyz(42.452,119.189,0);
m2.set_nv_xyz(.99334,-1,0);

Beamsplitter m3;
m3.set_thickness(7.492);
m3.set_substrate_radius(7.7695);
m3.set_center_xyz(-22.236,-24.565,0);
m3.set_nv_xyz(1,.99783,0);

Beamsplitter m5;
m5.set_thickness(7.272);
m5.set_substrate_radius(7.7925);
m5.set_center_xyz(-68.443,-106.149,0);
m5.set_nv_xyz(1,.99501,0);

Beamsplitter m6;
m6.set_thickness(7.319);
m6.set_substrate_radius(7.544);
m6.set_center_xyz(-34.442,-109.507,0);
m6.set_nv_xyz(-.927665,-1,0);

Beamsplitter m8;
m8.set_thickness(7.767);
m8.set_substrate_radius(7.784);
m8.set_center_xyz(-42.313,-61.341,0);
m8.set_nv_xyz(1,.99811,0);

Beamsplitter m9;
m9.set_thickness(7.220);
m9.set_substrate_radius(7.5375);
m9.set_center_xyz(-96.673,57.401,0);
m9.set_nv_xyz(.99625,-1,0);

```

```
Beamsplitter m10;
m10.set_thickness(7.124);
m10.set_substrate_radius(7.635);
m10.set_center_xyz(2.067,-105.058,0);
m10.set_nv_xyz(1,.99272,0);
```

```
Beamsplitter m11;
m11.set_thickness(7.5455);
m11.set_substrate_radius(7.5455);
m11.set_center_xyz(43.061,-1.735,0);
m11.set_nv_xyz(-.990966,1,0);
```

```
Beamsplitter m12;
m12.set_thickness(7.559);
m12.set_substrate_radius(7.559);
m12.set_center_xyz(67.747,92.361,0);
m12.set_nv_xyz(-.999755,1,0);
```

```
Beamsplitter m14;
m14.set_thickness(7.544);
m14.set_substrate_radius(7.544);
m14.set_center_xyz(96.342,8.234,0);
m14.set_nv_xyz(1,.99917,0);
```

```
// Only AR coated substrates
```

```
Beamsplitter bs1;
bs1.set_thickness(7.173);
bs1.set_substrate_radius(10.0035);
bs1.set_center_xyz(44.832,76.959,0);
bs1.set_nv_xyz(1,0.99383,0);
```

```
Beamsplitter bs4;
bs4.set_thickness(7.153);
bs4.set_substrate_radius(10.233);
bs4.set_center_xyz(-93.868,122.043,0);
bs4.set_nv_xyz(-1,.999097,0);
```

```
// 50/50 Beam splitter
```

```
Beamsplitter bs2;
bs2.set_thickness(7.222);
bs2.set_substrate_radius(10.076);
bs2.set_center_xyz(39.65,56.039,0);
bs2.set_nv_xyz(-1,0.998256,0);
```

```
Beamsplitter bs3;
bs3.set_thickness(7.240);
bs3.set_substrate_radius(10.1525);
bs3.set_center_xyz(13.678,58.741,0);
bs3.set_nv_xyz(1,0.99623,0);
```

```
Beamsplitter bs5;  
bs5.set_thickness(7.324);  
bs5.set_substrate_radius(10.064);  
bs5.set_center_xyz(-68.719,116.851,0);  
bs5.set_nv_xyz(-1,-0.998256,0);
```

```
Beamsplitter bs6;  
bs6.set_thickness(7.095);  
bs6.set_substrate_radius(10.064);  
bs6.set_center_xyz(-20.524,93.054,0);  
bs6.set_nv_xyz(1,0.99525,0);
```

```
Beamsplitter bs7;  
bs7.set_thickness(7.170);  
bs7.set_substrate_radius(10.0555);  
bs7.set_center_xyz(-71.925,35.262,0);  
bs7.set_nv_xyz(-1,.981462,0);
```

```
// Beam recombiner
```

```
Beamsplitter br1;  
br1.set_thickness(7.075);  
br1.set_substrate_radius(10.0435);  
br1.set_center_xyz(16.637,92.087,0);  
br1.set_nv_xyz(.99866,-1,0);
```

```
Beamsplitter br2;  
br2.set_thickness(7.280);  
br2.set_substrate_radius(10.096);  
br2.set_center_xyz(-21.045,53.245,0);  
br2.set_nv_xyz(.992576,-1,0);
```

```
Beamsplitter br3;  
br3.set_thickness(7.859);  
br3.set_substrate_radius(10.149);  
br3.set_center_xyz(-42.087,0.257,0);  
br3.set_nv_xyz(.99626,-1,0);
```

```
Beamsplitter br4;  
br4.set_thickness(7.648);  
br4.set_substrate_radius(10.0595);  
br4.set_center_xyz(-0.27,-81.962,0);  
br4.set_nv_xyz(-1,.99728,0);
```

Coordinate measurement machine

C.1. Background information

CMM probing strategy The required number of probing points depends on the geometric feature, which are planes, circles, *etc.*; of the workpiece under investigation. It is sufficient to probe with three points to identify a geometric feature as a plane. For several reasons it is beneficial to use more points than this minimum number of three. Within the CMM software PC-DMIS (used version 4.3) a least square fit is performed to calculate the according geometric feature. Not only a higher number of probing points minimizes the uncertainty of the calculated plane also the distribution of the probing points is important. Effects like surface roughness cancel out if the probing points are distributed over the whole plane. Furthermore, the angle of the plane within space can be determined more precise (using the same number of probing points) when a larger area is probed. For a plane the recommendations are to probe 9 points and to segment the plane in 3×3 squares. Within each square one point should be probed [112, p. 26].

Datum reference frame The CMM provides its own so-called machine coordinate system. If a measurement is started the coordinates of the probe points are taken within this machine coordinate system. Sometimes it is not useful to use this machine coordinate system, but a coordinate system which is fixed to a workpiece. Such a system is called datum reference frame. It is set up by probing three individual, mutually perpendicular geometric features of the workpiece [113]. In case of the SPI three planes have been used at all instances. The intersection point of all three planes defines the origin of the

datum reference frame. The coordinate axes are generated by the intersection of two planes. The resulting coordinate system is a Cartesian one. Thus the intersection line of the planes are slightly corrected in direction to end up with coordinate axes mutually perpendicular to each other.

C.2. Settings

Table C.1.: Measuring conditions and specifications of the coordinate measurement machine Global advantage. These values were used to calculate the errors of the CMM aided measurements presented in chapter 6 section 6.2.

Parameter	Symbol	Value
Linear encoder		Lida 48 by Heidenhain
CTE of linear encoder	α_m	$\approx 10 \cdot 10^{-6} \text{ K}^{-1}$
Mean temperature of the linear encoder	T_m	20.5 °C
Deviation from mean temperature	δT_m	0.5 K
Stylus (length times ball diameter)		30 mm × 5 mm
Calibration uncertainty of requalification sphere	U_c	0.2 μm
Volumetric length measuring error	MPE_E	$(A + L [\text{mm}]/K) \mu\text{m}^a$
	A	1.5 μm
	K	333
CTE of Clearceram [®] -Z HS	α_w	$0.02 \cdot 10^{-6} \text{ K}^{-1}$
CTE of brass	α_w	$19.7 \cdot 10^{-6} \text{ K}^{-1}$
Mean temperature of the work piece	T_w	20.5 °C
Deviation from mean temperature	δT_w	0.5 K

^a L is the current measuring length.

C.3. Error analysis of CMM measurements

The error of a CMM measurement is not only given by the volumetric length measurement error MPE_E . The uncertainty of the measurement depends on, e.g. environmental conditions, the type of measured element, e.g. cone, plane,

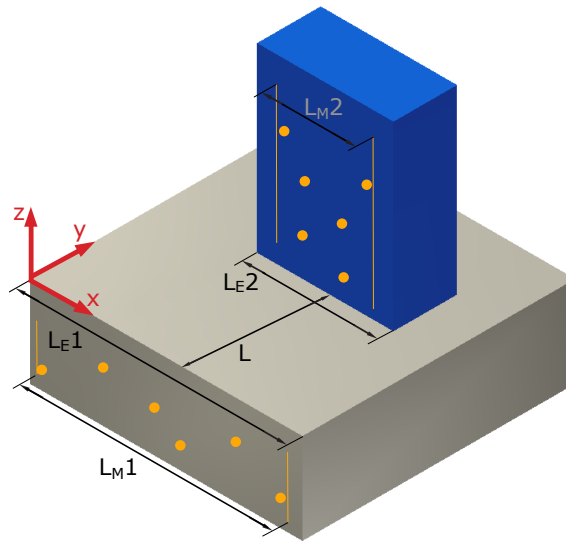


Figure C.1.: A mirror is bonded onto a base plate. An error analysis of the distance between the base plate's and the mirror's front surface should be done. L is the nominal length or y coordinate between both surfaces. L_M is the measured length at the element whereas L_E is the total length of the element. Orange points indicate positions where the CMM stylus has probed the mirror.

point, etc. and the number of measured points during the measurement of the work piece and of the calibration of the stylus.

Within the assembly process of the SPI, the CMM was used to measure distances, positions and diameters. In the following, I will summarize how an error analysis for those types of measurement was done. The following tables combine the information given in table 3.9, 8.1–8.4 and 8.6 in book [100].

Table C.2.: Error analysis for distance and position measurement with CMM. The formulae in this table can be used if the distance or position has been derived from the measurement of two planes. Just replace the numbers in blue with the numbers of the current CMM measurement. The error of the measurement is then a straightforward calculation. If other elements were measured, the distribution might be different (see table 3.9 in [100] for the appropriate distribution factor). This table is continued in table C.2.

Parameter	Symbol	Number of measurement points	Standard deviation	Distribution	Sensitivity coefficient	Uncertainty contribution
		n_i	s_i	b_i	c_i	$u_i(y)$ [μm]
Coordinate of first element	X_1	6	A/3	$\sqrt{1/n_i}$	1.0	$s_i \cdot b_i \cdot c_i$
Angular deviation of first element	W_1	6	A/3	$\sqrt{\frac{12 \cdot (n_i - 1)}{n_i \cdot (n_i + 1)}}$	$\frac{L_{E1}}{2 * L_{M1}}$	$s_i \cdot b_i \cdot c_i$
Deviation of stylus radius	ΔR_{T1}	25	A/3	$\sqrt{4/n_i}$	1.0	$s_i \cdot b_i \cdot c_i$
Coordinate of second element	X_2	6	A/3	$\sqrt{1/n_i}$	1.0	$s_i \cdot b_i \cdot c_i$
Angular deviation of second element	W_2	6	A/3	$\sqrt{\frac{12 \cdot (n_i - 1)}{n_i \cdot (n_i + 1)}}$	$\frac{L_{E2}}{2 * L_{M2}}$	$s_i \cdot b_i \cdot c_i$
Diameter deviation of qualification sphere	ΔD_c		U_c	0.5	0.5	$s_i \cdot b_i \cdot c_i$
Estimated correction of geometry deviation of the CMM	ΔL_{KMG}		$\sqrt{\frac{L_E^2 + l^2}{K}}$	a		
CTE deviation of the linear encoder	$\Delta L\alpha_m$		$\alpha_m/5$	0.58	$\frac{L \cdot (T_m - 20^\circ\text{C})}{1000}$	$s_i \cdot b_i \cdot c_i$
CTE deviation of the work piece	$\Delta L\alpha_w$		$\alpha_w/5$	0.58	$\frac{L \cdot (T_w - 20^\circ\text{C})}{1000}$	$s_i \cdot b_i \cdot c_i$
Temperature deviation of the linear encoder	$\Delta T\alpha_m$		δT_m	0.58	$\frac{L \cdot \alpha_m}{1000}$	$s_i \cdot b_i \cdot c_i$
Temperature deviation of the work piece	$\Delta T\alpha_w$		δT_w	0.58	$\frac{L \cdot \alpha_w}{1000}$	$s_i \cdot b_i \cdot c_i$

^a l is the largest value of L_{E1} and L_{E2} perpendicular to the direction of interest, i.e. the $L_{E,X}$ with $X = 1$ or $X = 2$ in x-direction if interested in y-position.

Table C.2.: Continuation of the table on p. 136.

Parameter	Symbol	Formula
Standard deviation	$u(y)$	$\sqrt{\sum_{i=1}^N u_i^2(y)}$
Degree of freedom	ν	$u^4(y) / \sum_{i=1}^N \frac{u_i^4(y)}{(n_i - p_i) \cdot m_i}$ ^{a b}
Extension factor	k	2^c
Temperature compensation	ΔL_T	$L \cdot [-\alpha_w \cdot (t_w - 20^\circ\text{C}) + \alpha_m \cdot (t_m - 20^\circ\text{C})]$
Extended measurement uncertainty	U	$k \cdot u(y) + L_T$

^a $\Delta D_C, \Delta L_{KMG}, \Delta \alpha_m, \Delta \alpha_w, \Delta T_m, \Delta T_w$ do not contribute to the calculation of the degree of freedom.

^b m_i is the number of measurements, p_i is the number of free parameters of the measured element. p_i is 1 for a point, 2 for a line, 3 for a plane and circle, 4 for a sphere, 5 for a cylinder and 6 for a cone.

^cLook at a table of Student's t-distribution to figured out the k factor for the according degree of freedom ν , often $k = 2$ is a good estimation.

C.3.1. Distance and position measurement

This example calculates the error of a distance measurement between two planes, namely a mirror mirror surface and a plane of a base plate (see Figure C.1). Three different ways exists to determine the distance: (i) to measure one point on each surface, (ii) to measure several points along a line on each surface and (iii) to measure with several surface points on the planes. The last approach has the smallest error and is used in this example. The resulting distance is the distance between the geometric centre of both planes. The stylus has been calibrated at the qualification sphere with 25 measurement points (see 3rd column and 3rd line in table C.2). Each of the two planes have been probed with 6 measurement points (see 3rd column table C.2 line 1–2 and 3–4.). The standard deviation, distribution and sensitivity coefficients can be calculated from the formulae given in column 4–6. These formulae hold for all error analysis of distance and position measurements derived from the measurement of two planes. Table C.2 is the continuation of table C.2 and is general error analysis.

C.3.2. Diameter measurement

Table C.3 and C.3 can be used to calculate the error of a diameter measurement of a circle, sphere, hemisphere, cone and cylinder.

Table C.3.: Error analysis for diameter measurement with CMM. The formulae in this table can be used to analyze the error of diameter measurements for circles, spheres, hemispheres, cones and cylinders. Just replace the numbers in blue with the numbers of the current CMM measurement. The error of the measurement is then a straightforward calculation. This table is continued in table C.3.

Parameter	Symbol	Number of measurement points	Standard deviation	Distribution	Sensitivity coefficient	Uncertainty contribution
		n_i	s_i	b_i	c_i	$u_i(y)$ [μm]
Diameter of the element	D_w	10	A/3	$\sqrt{4/n_i^a}$	1.0	$s_i \cdot b_i \cdot c_i$
Deviation of stylus radius during calibration at qualified sphere	ΔD_T	25	A/3	$\sqrt{4/n_i^b}$	1.0	$s_i \cdot b_i \cdot c_i$
Deviation of calibrated qualification sphere	ΔD_c		U_c	0.5	1.0	$s_i \cdot b_i \cdot c_i$
Estimated correction of geometry deviation of the CMM	ΔL_{KMG}		$\frac{\sqrt{D^2+L^2}}{K}$	0.5	1.0	$s_i \cdot b_i \cdot c_i$
CTE deviation of the linear encoder	$\Delta L\alpha_m$		$\alpha_m/5$	0.58	$\frac{D \cdot (T_m - 20^\circ\text{C})}{1000}$	$s_i \cdot b_i \cdot c_i$
CTE deviation of the work piece	$\Delta L\alpha_w$		$\alpha_w/5$	0.58	$\frac{D \cdot (T_w - 20^\circ\text{C})}{1000}$	$s_i \cdot b_i \cdot c_i$
Temperature deviation of the linear encoder	$\Delta T\alpha_m$		δT_m	0.58	$\frac{D \cdot \alpha_m}{1000}$	$s_i \cdot b_i \cdot c_i$
Temperature deviation of the work piece	$\Delta T\alpha_w$		δT_w	0.58	$\frac{D \cdot \alpha_m}{1000}$	$s_i \cdot b_i \cdot c_i$

^a $b_i = 1.5\sqrt{4/n_i}$ in case of a hemisphere, $b_i = 1$ for $n_i = 5$ and $n_i = 6$.

^b $b_i = 1.5\sqrt{4/n_i}$ in case of a hemisphere, $b_i = 1$ for $n_i = 5$ and $n_i = 6$.

^c l is the height of a cylinder or cone, i.e. $l = 0$ in case of a circle, sphere or hemisphere.

Table C.3.: Continuation of the table on p. 138.

Parameter	Symbol	Formula
Standard deviation	$u(y)$	$\sqrt{\sum_{i=1}^N u_i^2(y)}$
Degree of freedom	ν	$u^4(y) / \sum_{i=1}^N \frac{u_i^4(y)}{(n_i - p_i) \cdot m_i} ab$
Extension factor	k	2^c
Temperature compensation	ΔL_T	$L \cdot [-\alpha_w \cdot (t_w - 20^\circ\text{C}) + \alpha_m \cdot (t_m - 20^\circ\text{C})]$
Extended measurement uncertainty	U	$k \cdot u(y) + L_T$

^aOnly D_w and ΔD_T contribute to the calculation of the degree of freedom.

^b m_i is the number of measurements, p_i is the number of free parameters of the measured element. p_i is 1 for a point, 2 for a line, 3 for a plane and circle, 4 for a sphere, 5 for a cylinder and 6 for a cone.

^cLook at a table of Student's t-distribution to figured out the k factor for the according degree of freedom ν , often $k = 2$ is a good estimation.

Re-use of a Zerodur base plate

Two Michelson interferometers were bonded on a $\varnothing = 150$ mm disc of Zerodur in September 2004; see Figure D.1a. The disc has a total flatness of $\lambda/10$ as required for silicate bonding, but the surface is kept rough with a peak-to-valley roughness of $5\ \mu\text{m}$ [114, p.35]. One of the Michelson interferometers consisting of two mirrors and one beam splitter of the size of $20\ \text{mm} \times 20\ \text{mm} \times 5\ \text{mm}$ has the bonding surface ($20\ \text{mm} \times 5\ \text{mm}$) smooth polished, the components of the second interferometer have also rough surfaces.

Former results already showed that polished/rough bonds have ten-times lower shear-test results than polished/polish bonds. Also it was observed over the years, that the bonding surface of polished/rough bonds degraded from clear to milky which was taken as an indication that the bond was loosing.

For re-using the disc, it was decided to de-bond the components, if possible. After 5 h in an ultra-sonic bath filled with a 10 % solution of Decan 90 cleaner all optical components were detached from the Zerodur surface; see Figure D.1b. The base plate showed some minor marks at the position of former optics. For comparison, the attempt to separate polished/polished optical components with a footprint of $30\ \text{mm} \times 8\ \text{mm}$ which were bonded in fall 2004 under the same conditions failed; see Figure D.2. Even after one day in the ultra-sonic bath the components remained bonded. Thus, the bonding strength of polished/rough bonds is less than the bonding strength of polished/polished bonds. The gap between the two surfaces might have been too large at some points between the rough base plate and the components to form the bond. This resulted in a reduced bonding strength [115]. Such the use of rough/polished and rough/rough surfaces is not recommended. If an optical setup requires a high mechanical stability with the possibility of re-using the

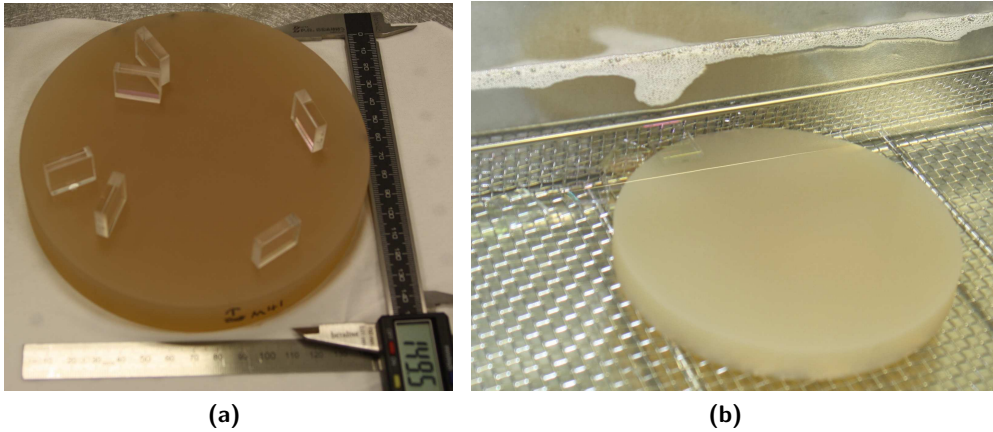


Figure D.1.: The rough Zerodur base plate with bonded components (a) and inside the ultra-sonic bath (b) after a 5 h lasting bath. The detached components are in the upper left part of Figure (b).

base plate the technique of optical contacting is recommended, because the optical coatings are not damaged during the disassembly process.

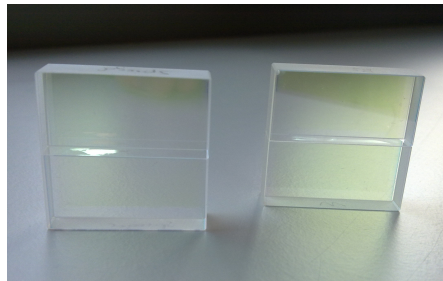


Figure D.2.: Polished/polished bonded components. Even though the bond was not formed over the entire area (see marks at bonding surface) the bond was strong enough such that the components could not be separated within an ultra-sonic bath.

References

- [1] G. M. HARRY AND THE LIGO SCIENTIFIC COLLABORATION. **Advanced LIGO: the next generation of gravitational wave detectors**. *Classical and Quantum Gravity*, **27**(8):084006, 2010. xvii, 12
- [2] S. M. ASTON. *Optical read-out techniques for the control of test-masses in gravitational wave observatories*. PhD thesis, University of Birmingham, 2011. xvii, 16
- [3] M. DEHNE. *Construction and noise behaviour of ultra-stable optical systems for space interferometers*. PhD thesis, Leibniz Universität Hannover, 2012. xviii, 29, 32, 51, 77, 81, 82, 96, 99
- [4] G. CELLA, R. DESALVO, V. SANNIBALE, H. TARIQ, N. VIBOUD, AND A. TAKAMORI. **Seismic attenuation performance of the first prototype of a geometric anti-spring filter**. *Nuclear Instruments and Methods in Physics Research Section A: Accelerators, Spectrometers, Detectors and Associated Equipment*, **487**(3):652–660, 2002. xviii, 13
- [5] A. STOCHINO ET AL. **The Seismic Attenuation System (SAS) for the Advanced LIGO gravitational wave interferometric detectors**. *Nuclear Instruments and Methods in Physics Research Section A: Accelerators, Spectrometers, Detectors and Associated Equipment*, **598**(3):737–753, 2009. xviii, 12
- [6] **KAGRA webpage**, May 2013. xviii
- [7] K. DANZMANN. **LISA – An ESA cornerstone mission for the detection and observation of gravitational waves**. *Advances in Space Research*, **32**(7):1233–1242, 2003. Fundamental Physics in Space. xix

- [8] P. MCNAMARA, S. VITALE, K. DANZMANN, AND ON BEHALF OF THE LISA PATHFINDER SCIENCE WORKING TEAM. **LISA Pathfinder**. *Classical and Quantum Gravity*, **25**(11):114034, 2008. xix, 21
- [9] A. EINSTEIN. **Die Grundlage der allgemeinen Relativitätstheorie**. *Annalen der Physik*, **49**:769, 1916. 1
- [10] A. EINSTEIN. **Über Gravitationswellen**. *Akademie-Vorträge: Sitzungsberichte der Königlich Preußischen Akademie der Wissenschaften*, page 135, 1914-1932. 1
- [11] P. R. SAULSON. *Fundamentals of interferometric gravitational wave detectors*. World Scientific Publishing Co. Pte. Ltd., 1994. 1, 8, 106
- [12] R. WEISS. **Electromagnetically coupled broadband gravitational antenna**. LIGO Document P720002-01-R, 1972. 1
- [13] H GROTE AND THE LIGO SCIENTIFIC COLLABORATION. **The GEO 600 status**. *Classical and Quantum Gravity*, **27**(8):084003, 2010. 1
- [14] B. P. ABBOTT ET AL. **LIGO: the Laser Interferometer Gravitational-Wave Observatory**. *Reports on Progress in Physics*, **72**(7):076901, 2009. 1
- [15] T. ACCADIA ET AL. **Status of the Virgo project**. *Classical and Quantum Gravity*, **28**(11):114002, 2011. 1
- [16] K. DANZMANN ET AL. **LISA (Laser Interferometer Space Antenna). Proposal for a Laser-Interferometric Gravitational Wave Detector in Space**. Technical report, Report MPQ 177, 1993. 1
- [17] O. JENNRICH ET AL. **NGO assessment study report (Yellow Book)**. ESA/SRE(2011)19, 2011. 1
- [18] S. KAWAMURA ET AL. **The Japanese space gravitational wave antenna: DECIGO**. *Classical and Quantum Gravity*, **28**(9):094011, 2011. 1
- [19] C. CUTLER AND J. HARMS. **Big bang observer and the neutron-star- binary subtraction problem**. *Phys. Rev. D*, **73**:042001, 2006. 1

-
- [20] J. HARMS, C. MAHRDT, M. OTTO, AND M. PRIESS. **Subtraction-noise projection in gravitational-wave detector networks**. *Phys. Rev. D*, **77**:123010, 2008. 1
- [21] B. ABBOTT ET AL. **% bf Detector description and performance for the first coincidence observations between LIGO and GEO**. *Nuclear Instruments and Methods in Physics Research Section A: Accelerators, Spectrometers, Detectors and Associated Equipment*, **517**(1–3):154–179, 2004. 1
- [22] J. ABADIE ET AL. **All-sky search for gravitational-wave bursts in the first joint LIGO-GEO-Virgo run**. *Phys. Rev. D*, **81**(10):102001, May 2010. 1
- [23] B. ABBOTT ET AL. **Search for gravitational-wave bursts in LIGO’s third science run**. *Classical and Quantum Gravity*, **23**(8):S29, 2006. 1
- [24] H. LÜCK ET AL. **The upgrade of GEO 600**. *Journal of Physics: Conference Series*, **228**(1):012012, 2010. 1
- [25] G. M. HARRY AND THE LIGO SCIENTIFIC COLLABORATION. **Advanced LIGO: the next generation of gravitational wave detectors**. *Classical and Quantum Gravity*, **27**(8):084006, 2010. 1
- [26] N. A. LOCKERBIE, L. CARBONE, B. SHAPIRO, K. V. TOKMAKOV, A. BELL, AND K. A. STRAIN. *Classical and Quantum Gravity*, **28**(245001), 2011. 1
- [27] R. L. WARD ET AL. **dc readout experiment at the Caltech 40m prototype interferometer**. *Classical and Quantum Gravity*, **25**(11):114030, 2008. 2
- [28] S. MIYOKI ET AL. **Status of the CLIO project**. *Classical and Quantum Gravity*, **21**(5):S1173, 2004. 2
- [29] M. P. EDGAR ET AL. **Experimental demonstration of a suspended diffractively coupled optical cavity**. *Opt. Lett.*, **34**(20):3184–3186, Oct 2009. 2
- [30] K. KURODA AND THE LCGT COLLABORATION. **Status of LCGT**. *Classical and Quantum Gravity*, **27**(8):084004, 2010. 2

- [31] R. W. P. DREVER. **Outline of a proposed design for a first receiver for installation in the long-baseline facilities, of Fabry-Perot type**. LIGO Document T870001-00-R, 1987. 2, 19
- [32] R. W. P. DREVER AND S. J. AUGST. **Extension of gravity-wave interferometer operation to low frequencies**. *Classical and Quantum Gravity*, **19**:2005, 2002. 2
- [33] Y. ASO, M. ANDO, K. KAWABE, S. OTSUKA, AND K. TSUBONO. **Stabilization of a Fabry-Perot interferometer using a suspension-point interferometer**. *Physics Letters A*, **327**(1):1–8, 2004. 3, 19
- [34] A. WANNER ET AL. **Seismic attenuation system for the AEI 10 meter prototype**. *Classical and Quantum Gravity*, **29**:245007, 2012. 3, 14
- [35] N. A. ROBERTSON, G. CAGNOLI, D. R. M. CROOKS, E. ELLIFFE, J. E. FALLER, P. FRITSCHER, S. GOSLER, A. GRANT, A. HEPTONSTALL, J. HOUGH, H. LUCK, R. MITTLEMAN, M. PERREUR-LLOYD, M. V. PLISSI, S. ROWAN, D. H. SHOEMAKER, P. H. SNEDDON, K. A. STRAIN, C. I. TORRIE, H. WARD, AND P. WILLEMS. **Quadruple suspension design for Advanced LIGO**. *Classical and Quantum Gravity*, **19**(15):4043–4058, 2002. 3
- [36] FOR THE LSC LSC ADVANCED DETECTOR COMMITTEE. **LSC Instrument Science White Paper 2010**. LIGO Document T1000416-v3, 2010. 3
- [37] Y. ASO. *Active Vibration Isolation for a Laser Interferometric Gravitational Wave Detector using a Suspension Point Interferometer*. PhD thesis, University of Tokyo, 2006. 3
- [38] K. DAHL, A. BERTOLINI, M. BORN, Y. CHEN, D. GERING, S. GOSSLER, C. GRÄF, G. HEINZEL, S. HILD, F. KAWAZOE, O. KRANZ, G. KÜHN, H. LÜCK, K. MOSSAVI, R. SCHNABEL, K. SOMIYA, K. A. STRAIN, J. R. TAYLOR, A. WANNER, T. WESTPHAL, B. WILLKE, AND K. DANZMANN. **Towards a Suspension Platform Interferometer for the AEI 10 m Prototype Interferometer**. *Journal of Physics: Conference Series*, **228**(1):012027, 2010. 4
- [39] K. DAHL ET AL. **Status of the AEI 10 m prototype**. *Classical and Quantum Gravity*, **29**:145005, 2012. 4

-
- [40] K. DAHL, G. HEINZEL, B. WILLKE, K. A. STRAIN, S. GOSSLER, AND K. DANZMANN. **Suspension platform interferometer for the AEI 10 m prototype: concept, design and optical layout.** *Classical and Quantum Gravity*, **29**(095024), 2012. 4
- [41] C. M. CAVES. **Quantum-Mechanical Radiation-Pressure Fluctuations in an Interferometer.** *Phys. Rev. Lett.*, **45**(2):75–79, Jul 1980. 7
- [42] K. SOMIYA ET AL. **Conceptual design of an interferometer with a sub-SQL sensitivity.** LIGO Document T0900069, 2009. 8, 9
- [43] F. Y. KHALILI. **Reducing the mirrors coating noise in laser gravitational-wave antennae by means of double mirrors.** *Physics Letters A*, **334**(1):67–72, 2005. 9
- [44] K. SOMIYA. **Reduction and Possible Elimination of Coating Thermal Noise Using a Rigidly Controlled Cavity with a Quantum-Nondemolition Technique.** *Phys. Rev. Lett.*, **102**(23):230801, Jun 2009. 9
- [45] G. M. HARRY. **Titania-doped tantala/silica coatings for gravitational-wave detection.** *Classical and Quantum Gravity*, **24**:405, 2007. 9
- [46] C. GRÄF ET AL. **Optical layout for a 10 m Fabry-Perot Michelson interferometer with tunable stability.** *Classical and Quantum Gravity*, 2012. 10, 11
- [47] C. GRÄF. PhD thesis, Leibniz Universität Hannover, 2013. submitted for examination. 11
- [48] A. WANNER. *Seismic Attenuation System (AEI-SAS) for the AEI 10 m Prototype.* PhD thesis, Leibniz Universität Hannover, 2013. 12, 13, 14, 15, 63, 111, 113
- [49] G. LOSURDO ET AL. **An inverted pendulum preisolator stage for the VIRGO suspension system.** *Review of Scientific Instruments*, **70**(5):2507, May 1999. 13
- [50] A. TAKAMORI ET AL. **Inverted pendulum as low-frequency pre-isolation for advanced gravitational wave detectors.** *Nuclear Instruments and Methods in Physics Research Section A: Accelerators, Spectrometers, Detectors and Associated Equipment*, **582**(2):683–692, 2007. 13

- [51] A. STOCHINO, R. DESALVO, Y. HUANG, AND V. SANNIBALE. **% bf Improvement of the seismic noise attenuation performance of the Monolithic Geometric Anti-Spring filters for gravitational wave interferometric detectors.** *Nuclear Instruments and Methods in Physics Research Section A: Accelerators, Spectrometers, Detectors and Associated Equipment*, **580**:1559, 2007. 14
- [52] H. GROTE. *Making it Work: Second Generation Interferometry in GEO600!* PhD thesis, Universität Hannover, 2003. 17
- [53] M. FREDE ET AL. **Fundamental mode, single-frequency laser amplifier for gravitational wave detectors.** *Opt. Express*, **15**(2):459–465, Jan 2007. 17
- [54] **Mephisto laser data sheet.** <http://www.innolight.de/index.php?id=mephisto>, July 2012. 17
- [55] F. KAWAZOE ET AL. **Designs of the frequency reference cavity for the AEI 10 m Prototype interferometer.** *Journal of Physics: Conference Series*, **228**(1):012028, 2010. 17
- [56] E. D. BLACK. **An introduction to Pound–Drever–Hall laser frequency stabilization.** *American Journal of Physics*, **69**(1):79–87, 2001. 17
- [57] F. KAWAZOE ET AL. **The AEI 10 m Prototype Interferometer frequency control using the reference cavity and its angular control.** *J. Phys.: Conf. Ser.*, 2012. 18
- [58] E. MORRISON, B. J. MEERS, D. I. ROBERTSON, AND H. WARD. **Experimental demonstration of an automatic alignment system for optical interferometers.** *Appl. Opt.*, **33**(22):5037–5040, Aug 1994. 18
- [59] R. BORK. **AdvLigo CDS Design Overview.** *LIGO Document Control Center*, (T0900612), 2010. 18
- [60] T. WESTPHAL ET AL. **The 10m AEI prototype facility A brief overview.** *Applied Physics B: Lasers and Optics*, **340**, 2012. 18
- [61] ERIC D. BLACK. **An introduction to Pound–Drever–Hall laser frequency stabilization.** *American Journal of Physics*, **69**(1):79–87, 2001. 19

-
- [62] D. A. SHADDOCK. **Digitally enhanced heterodyne interferometry**. *Opt. Lett.*, **32**(22):3355–3357, 2007. 20
- [63] G. DE VINE ET AL. **Picometer level displacement metrology with digitally enhanced heterodyne interferometry**. *Opt. Express*, **17**(2):828–837, Jan 2009. 20
- [64] J. MILLER, S. NGO, A. J. MULLAVEY, B. J. J. SLAGMOLEN, D. A. SHADDOCK, AND D. E. MCCLELLAND. **Control and tuning of a suspended Fabry-Perot cavity using digitally enhanced heterodyne interferometry**. *Opt. Lett.*, **37**(23):4952–4954, 2012. 20
- [65] R. L. BYER, M. M. FEJER, B. LANTZ, AND R. ROUTE. https://dcc.ligo.org/DocDB/0093/T1200312/001/LIGO_1068596_ATR_2012_v2.pdf, 2012. 20
- [66] D. CLARK. **PhD Dissertation Defense - The Seismic Platform Interferometer**. LIGO Document G1201203-v1, 2012. 20
- [67] S. C. COHEN. **Heterodyne detection: phase front alignment, beam spot size, and detector uniformity**. *Applied Optics*, **14**:1953, 1975. 23
- [68] M. SALEM AND J. P. ROLLAND. **Heterodyne efficiency of a detection system for partially coherent beams**. *J. Opt. Soc. Am. A*, **27**(5):1111–1119, May 2010. 23
- [69] R. DIAZ-URIBE, M. ROSETE-AGUILAR, AND R. ORTEGA-MARTINEZ. **Position sensing of a Gaussian beam with a power meter and a knife edge**. *Revista Mexicana de Fisica*, **39**(3):484–492, 1993. 25, 26
- [70] G. D. RACCA AND P. W. MCNAMARA. **The LISA Pathfinder Mission**. *Space Science Reviews*, **151**:159, 2010. 27
- [71] G. WANNER. *Complex optical systems in space: numerical modelling of the heterodyne interferometry of LISA Pathfinder and LISA*. PhD thesis, Leibniz Universität Hannover, 2010. 27, 62
- [72] W. STAUD AND J. T. WEED, editors. *Updates on the coefficient of thermal expansion property and surface finish capability of CLEARCERAM-Z series for EUVL photomask substrate application*, **5567**. SPIE, 2004. 29, 44, 53

- [73] **Suprasil data sheet.** http://heraeus-quarzglas.com/media/webmedia_local/downloads/broschren_mo/DataandProperties_Optics_fusedsilica.pdf, January 2013. 29, 53
- [74] E. J. ELLIFFE ET AL. **Hydroxide-catalysis bonding for stable optical systems for space.** *Classical and Quantum Gravity*, **22**(10):S257–S267, 2005. 30, 44, 73, 74, 77
- [75] J. N. REDDY. *Theory and analysis of elastic plates.* Taylor & Francis, 1999. 30
- [76] C. KILLOW ET AL. **LTP interferometer — noise sources and performance.** *Classical and Quantum Gravity*, **22**(10):S155–S163, 2005. 32, 77
- [77] V. WAND ET AL. **Noise sources in the LTP heterodyne interferometer.** *Classical and Quantum Gravity*, **23**(8):S159–S167, 2006. 32, 103
- [78] H. AUDLEY ET AL. **The LISA Pathfinder interferometry — hardware and system testing.** *Classical and Quantum Gravity*, **28**(9):094003, 2011. 32
- [79] **Adjustable optics holder AAH 5 AXES.** <http://www.pimicos.com/web2/data/download/sheet/photon/albatros/2.2251.pdf>, January 2013. 33, 82
- [80] **Fiber collimators.** http://www.sukhamburg.com/onTEAM/pdf/fk60fc_e.pdf, January 2013. 34
- [81] A. THÜRING AND N. LASTZKA. **JamMt (version 0.24) - Just another mode matching tool.** <http://www.sr.bham.ac.uk/dokuwiki/doku.php?id=geosim:jammt>, 2011. Simulation Tool. 34
- [82] S. SKORUPKA. *Rauschuntersuchungen an hochstabilen Lasersystemen für die wissenschaftliche Weltraummission LISA.* PhD thesis, Leibniz Universität Hannover, 2007. 36
- [83] G. HEINZEL ET AL. **The LTP interferometer and phasemeter.** *Classical and Quantum Gravity*, **21**(5):S581–S587, 2004. 36, 37, 39
- [84] **Innolight iodine frequency stabilization data sheet.** http://www.innolight.de/fileadmin/user_upload/produktblatt_pdf/Produktblatt_Laser_Accessoires.pdf, August 2012. 37, 44, 50, 53

-
- [85] V. WAND. *Interferometry at low frequencies: optical phase measurement for LISA and LISA Pathfinder*. PhD thesis, Leibniz Universität Hannover, 2007. 37, 103
- [86] G. HEINZEL, A. RÜDIGER, AND R. SCHILLING. **Spectrum and spectral density estimation by the Discrete Fourier transform (DFT), including a comprehensive list of window functions and some new flat-top windows**, February 2002. 38
- [87] D. GERING. *Phasemeter Interface*. Diploma thesis, Fachhochschule Hannover, 2009. 40
- [88] **First Sensor QP data sheet**. http://www.first-sensor.com/sites/www.first-sensor.com/files/downloads/datasheets/optical_sensors/components/detectors/quadrant_photodiodes_qp_-_qp_series/series_6/qp50-6-500142-500732_1.pdf, January 2013. 49, 53
- [89] R. FLEDDERMANN. *Interferometry for a space-based gravitational wave observatory Reciprocity of an optical fiber*. PhD thesis, Leibniz Universität Hannover, 2012. 51
- [90] M. TRÖBS ET AL. **Testing the LISA optical bench**. Proc. of the International Conference on Space Optics, 2012. 52, 53
- [91] H. STÖCKER, editor. *Taschenbuch der Physik : Formeln, Tabellen, Übersichten*. Deutsch, Frankfurt am Main, 5., korrigierte aufl., nachdr. edition, 2007. 53
- [92] C. DIEKMANN. *Development of core elements for the LISA optical bench - Electro-optical measurement systems and test devices*. PhD thesis, Leibniz Universität Hannover, 2013. 53, 54
- [93] R. SCHILLING. **OPTOCAD (version 0.90c): A Fortran 95 module for tracing Gaussian TEM₀₀ beams through an optical set-up**. [http://www.rzg.mpg.de/~sim\\$ros/optocad.html](http://www.rzg.mpg.de/~sim$ros/optocad.html), 2010. Simulation Tool. 55
- [94] G. HEINZEL. **IFOCAD: A framework of C subroutines to plan and optimize the geometry of laser interferometers**, 2010. Simulation Tool. 55
- [95] **Private communication with Gerhard Heinzel**, 12 2012. 58

- [96] H. ARMANDULA. **Silicate Bonding Procedure (Hydroxide-Catalysis Bonding)**. LIGO Document E050228, 2005. 73
- [97] V. GRECO, F. MARCHESINI, AND G. MOLESINI. **Optical contact and van der Waals interactions: the role of the surface topography in determining the bonding strength of thick glass plates**. *Journal of Optics A: Pure and Applied Optics*, **3**(1):85, 2001. 76
- [98] **Optocast adhesives data sheet**. http://www.emiuv.com/media/files/OPTOCAST_8-15-2011.pdf, 2011. 76
- [99] F. STEIER, R. FLEDDERMANN, J. BOGENSTAHL, C. DIEKMANN, G. HEINZEL, AND K. DANZMANN. **Construction of the LISA back-side fibre link interferometer prototype**. *Classical and Quantum Gravity*, **26**(17):175016 (7pp), 2009. 77
- [100] M. HERNLA. *Messunsicherheit bei Koordinatenmessungen: Abschätzung der aufgabenspezifischen Messunsicherheit mit Hilfe von Berechnungstabellen*. Expert-Verlag, Renningen, 2007. 81, 135, 136
- [101] E. D. FITZSIMONS ET AL. **Precision absolute positional measurement of laser beams**. *Appl. Opt.*, **52**(12):2527–2530, Apr 2013. 82
- [102] C. J. KILLOW ET AL. **Construction of the LTP Optical Bench Interferometer**. *AIP Conf. Proc.*, **873**:297, 2006. 82
- [103] M. SOMMERFELD. *Development of a calibrated quadrant photodiode pair (CQP)*. Diploma thesis, Universität Hannover, 2010. 82, 84
- [104] J.-S. HENNIG. *Konstruktion und Charakterisierung von ultra-stabilen Faserkopplern*. Bachelor’s thesis, Leibniz Universität Hannover, 2011. 84, 85, 98, 129
- [105] J. BOGENSTAHL ET AL. **LTP fibre injector qualification and status**. *Journal of Physics: Conference Series*, **154**(1):012011, 2009. 85
- [106] M. E. CALDWELL ET AL. **Prototype optical bench instrument in the interferometer for the LISA Pathfinder space mission**. *Opt. Eng.*, **45**:125601, 2006. 88
- [107] **Laser spirit level data sheet**. http://www.hilti.de/holdere/page/module/product/prca_productdetail.jsf?lang=de&nodeId=-521720&selProdOid=1259822, February 2013. 94

-
- [108] A. F. GARCIA MARIN. *Minimisation of optical pathlength noise for the detection of gravitational waves with the spaceborne laser interferometer LISA and LISA Pathfinder*. PhD thesis, Leibniz Universität Hannover, 2007. 103
- [109] G. HEINZEL ET AL. **Investigation of noise sources in the LTP interferometer S2-AEI-TN-3028**. http://pubman.mpdl.mpg.de/pubman/item/escidoc:149897:2/component/escidoc:149896/ltp_noise.pdf, July 2008. 103
- [110] **Streckeisen STS-2**, April 2013. 106, 110
- [111] **Geophone L-4C data sheet**, April 2013. 110
- [112] D. FLACK. **Measurement Good Practice Guide No. 41: CMM Measurement Strategies**. Technical report, National Physical Laboratory, 2001. 133
- [113] M. R. MCCAULEY. **A Conceptual Data Model of Datum Systems**. *J. Res. Natl. Inst. Stand. Technol.*, **104**:349, 1999. 133
- [114] J. BOGENSTAHL. *Interferometer zur Charakterisierung von optischen Komponenten*. Master's thesis, Universität Hannover, 2005. 141
- [115] A. PRESTON, B. BALABAN, AND G. MUELLER. **Hydroxide-Bonding Strength Measurements for Space-Based Optical Missions**. *International Journal of Applied Ceramic Technology*, **5**(4):365–372, 2008. 141

List of publications

- [P9] K. Izumi, K. Arai, B. Barr, J. Betzwieser, A. Brooks, **K. Dahl**, S. Doravari, J. C. Driggers, W. Z. Korth, H. Miao, J. Rollins, S. Vass, D. Yeaton-Massey, and R. Adhikari. **Multi-color Cavity Metrology** *JOSA A* 29 (2092) 2012.
- [P8] **K. Dahl**, T. Alig, G. Bergmann, A. Bertolini, M. Born, Y. Chen, A. V. Cumming, L. Cunningham, C. Gräf, G. Hammond, G. Heinzl, S. Hild, S. H. Huttner, R. Jones, F. Kawazoe, S. Köhlenbeck, G. Kühn, H. Lück, K. Mossavi, P. Oppermann, J. Pödl, K. Somiya, A. A. van Veggel, A. Wanner, T. Westphal, B. Willke, K. A. Strain, S. Gößler, and K. Danzmann. **Status of the AEI 10 m prototype**. *Class. Quantum Grav.* 29 (145005) 2012.
- [P7] **K. Dahl**, G. Heinzl, B. Willke, K. A. Strain, S. Gößler, K. Danzmann. **Suspension platform interferometer for the AEI 10 m prototype: concept, design and optical layout**. *Class. Quantum Grav.* 29 (095024) 2012.
- [P6] T. Westphal, G. Bergmann, A. Bertolini, M. Born, Y. Chen, A. Cumming, L. Cunningham, **K. Dahl**, C. Gräf, G. Hammond, G. Heinzl, S. Hild, S. Huttner, R. Jones, F. Kawazoe, S. Köhlenbeck, G. Kühn, H. Lück, K. Mossavi, J. Pödl, K. Somiya, A. van Veggel, A. Wanner, B. Willke, K. A. Strain, S. Gößler, and K. Danzmann. **Design of the 10 m AEI prototype facility for interferometry studies**. *Appl. Phys. B* 106 (551) 2012.
- [P5] **K. Dahl**, A. Bertolini, M. Born, Y. Chen, D. Gering, S. Gößler, C. Gräf, G. Heinzl, S. Hild, F. Kawazoe, O. Kranz, G. Kühn, H. Lück, K. Mossavi, R. Schnabel, K. Somiya, K. A. Strain, J. R. Taylor, A. Wanner, T. Westphal, B. Willke, and K. Danzmann. **Towards a suspension**

- platform interferometer for the AEI 10 m prototype interferometer.** *Journal of Physics: Conference Series* 228 (012027) 2010.
- [P4] S. Goßler, A. Bertolini, M. Born, Y. Chen, **K. Dahl**, D. Gering, C. Gräf, G. Heinzl, S. Hild, F. Kawazoe, O. Kranz, G. Kühn, H. Lück, K. Mossavi, R. Schnabel, K. Somiya, K. A. Strain, J. R. Taylor, A. Wanner, T. Westphal, B. Willke, and K. Danzmann. **The AEI 10 m prototype interferometer.** *Classical and Quantum Gravity* 27 (084023) 2010.
- [P3] F. Kawazoe, J. R. Taylor, A. Bertolini, M. Born, Y. Chen, **K. Dahl**, D. Gering, S. Goßler, C. Gräf, G. Heinzl, S. Hild, O. Kranz, G. Kühn, H. Lück, K. Mossavi, R. Schnabel, K. Somiya, K. A. Strain, A. Wanner, T. Westphal, B. Willke, and K. Danzmann. **Designs of the frequency reference cavity for the AEI 10 m prototype interferometer.** *accepted for publication in Journal of Physics: Conference Series* 228 (012028) 2010.
- [P2] L. Spani Molella, **K. Dahl**, R.-H. Rinkleff, and K. Danzmann. **Coupling probe laser spectroscopy of degenerate two-level systems: An experimental survey of various polarisation combinations.** *Optics Communications*, 282 (17:3481) 2009.
- [P1] **K. Dahl**, L. Spani Molella, R.-H. Rinkleff, and K. Danzmann. **Switching from “absorption within transparency” to “transparency within transparency” in an electromagnetically induced absorption dominated transition.** *Opt. Lett.*, 33 (9:983) 2008.

Publications within the LSC

- [P25] J. Aasi,..., R. M. Cutler, **K. Dahl**, M. Damjanic, ..., J. Zweizig. **Einstein@Home all sky search for periodic gravitational waves in LIGO S5 data** *Phys. Rev. D* 87 (042001) 2013.
- [P24] J. Aasi,..., R. M. Cutler, **K. Dahl**, M. Damjanic, ..., J. Zweizig. **Search for gravitational waves from binary black hole inspiral, merger and ringdown in LIGO-Virgo data from 2009-2010** *Phys. Rev. D* 87 (022002) 2013.
- [P23] J. Abadie,..., R. M. Cutler, **K. Dahl**, S. L. Danilishin, ..., J. Zweizig. **Search for gravitational waves from low mass compact binary**

-
- coalescence in LIGO's sixth science run and Virgo's science runs 2 and 3 *Phys. Rev. D* 85 (082002) 2012.
- [P22] J. Abadie,..., R. M. Cutler, **K. Dahl**, S. L. Danilishin, ..., J. Zweizig. **All-sky search for periodic gravitational waves in the full S5 LIGO data** *Phys. Rev. D* 85 (022001) 2012.
- [P21] J. Abadie,..., R. M. Cutler, **K. Dahl**, S. L. Danilishin, ..., W. Zheng. **Implementation and testing of the first prompt search for gravitational wave transients with electromagnetic counterparts** *Astronomy & Astrophysics* 539 (A124) 2012.
- [P20] J. Abadie,..., R. M. Cutler, **K. Dahl**, S. L. Danilishin, ..., X.-L. Zhang. **First low-latency LIGO+Virgo search for binary inspirals and their electromagnetic counterparts** *Astronomy & Astrophysics* 541 (A155) 2012.
- [P19] J. Abadie,..., R. M. Cutler, **K. Dahl**, S. L. Danilishin, ..., J. Zweizig. **Upper limits on a stochastic gravitational-wave background using LIGO and Virgo interferometers at 600-1000 Hz** *Phys. Rev. D* 85 (122001) 2012.
- [P18] J. Abadie,..., R. M. Cutler, **K. Dahl**, S. L. Danilishin, ..., J. Zweizig. **All-sky search for gravitational-wave bursts in the second joint LIGO-Virgo run** *Phys. Rev. D* 85 (122007) 2012.
- [P17] J. Abadie,..., R. M. Cutler, **K. Dahl**, S. L. Danilishin, ..., J. Zweizig. **Search for gravitational waves associated with gamma-ray bursts during LIGO science run 6 and VIRGO science runs 2 and 3** *The Astrophysical Journal* 760 (12) 2012.
- [P16] J. Abadie,..., R. M. Cutler, **K. Dahl**, S. L. Danilishin, ..., J. Zweizig. **Search for gravitational waves from intermediate mass binary black holes** *Phys. Rev. D* 85 (102004) 2012.
- [P15] J. Aasi,..., R. M. Cutler, **K. Dahl**, M. Danjanic, ..., J. Zweizig. **The characterization of Virgo data and its impact on gravitational-wave searches** *Classical and Quantum Gravity* 29 (155002) 2012.
- [P14] J. Abadie,..., R. M. Cutler, **K. Dahl**, S. L. Danilishin, ..., J. Zweizig. **Implications for the origin of GRB 051103 from LIGO observations** *The Astrophysical Journal* 755 (2) 2012.

- [P13] P. A. Evans,..., R. M. Cutler, **K. Dahl**, M. Danjanic, ..., J. Zweizig. **Swift follow-up observations of candidate gravitational-wave transient events** *The Astrophysical Journal Supplement Series* 203 (28) 2012.
- [P12] J. Abadie,..., R. M. Cutler, **K. Dahl**, S. L. Danilishin, ..., J. Palfreyman. **A gravitational wave observatory operating beyond the quantum shot-noise limit** *Nature Physics* 7 (962-965) 2011.
- [P11] J. Abadie,..., E. Cuoco, **K. Dahl**, S. L. Danilishin, ..., J. Palfreyman. **Directional limits on persistent gravitational waves using LIGO S5 science data** *Phys. Rev. Lett.* 107 (271102) 2011.
- [P10] J. Abadie,..., E. Cuoco, **K. Dahl**, S. L. Danilishin, ..., J. Palfreyman. **Beating the spin-down limit on gravitational wave emission from the Vela pulsar.** *The Astrophysical Journal* 737 (93) 2011.
- [P9] J. Abadie,..., L. Cunningham, **K. Dahl**, S. L. Danilishin, ..., J. Zweizig. **Search for gravitational waves associated with August 2006 timing glitch of the Vela pulsar.** *Phys. Rev. D* 83 (042001) 2011.
- [P8] J. Abadie,..., E. Cuoco, **K. Dahl**, S. L. Danilishin, ..., J. Zweizig. **Search for gravitational wave bursts from six magnetars.** *The Astrophysical Journal* 734 (L35) 2011.
- [P7] J. Abadie,..., E. Cuoco, **K. Dahl**, S. L. Danilishin, ..., J. Zweizig. **Search for gravitational waves from binary black hole inspiral, merger, and ringdown.** *Phys. Rev. D* 83 (122005) 2011.
- [P6] J. Abadie,..., E. Cuoco, **K. Dahl**, M. Danjanic, ..., J. Zweizig. **Predictions for the rates of compact binary coalescences observable by ground-based gravitational-wave detectors** *Classical and Quantum Gravity* 27 (173001) 2010.
- [P5] J. Abadie,..., L. Cunningham, **K. Dahl**, S. L. Danilishin, ..., J. Zweizig. **First search for gravitational waves from the youngest known neutron star.** *ApJ* 722 (1504) 2010.
- [P4] J. Abadie,..., L. Cunningham, **K. Dahl**, S. L. Danilishin, ..., J. Zweizig. **Calibration of the LIGO gravitational wave detectors in the fifth science run.** *Nuclear Instruments and Methods in Physics Research Section A: Accelerators, Spectrometers, Detectors and Associated Equipment* 624 (223) 2010.

- [P3] J. Abadie,..., E. Cuoco, **K. Dahl**, S. L. Danilishin, ..., J. Zweizig. **All-sky search for gravitational-wave bursts in the first joint LIGO-GEO-Virgo run.** *Phys. Rev. D* 81 (102001) 2010.
- [P2] J. Abadie,..., E. Cuoco, **K. Dahl**, S. L. Danilishin, ..., J. Zweizig. **Search for gravitational-wave inspiral signals associated with short gamma-ray bursts during LIGO's fifth and VIRGO's first scientific run.** *ApJ* 715 (1453) 2010.
- [P1] J. Abadie,..., E. Cuoco, **K. Dahl**, S. L. Danilishin, ..., J. Zweizig. **Search for gravitational waves from compact binary coalescence in LIGO and Virgo data from S5 and VSR1.** *Phys. Rev. D* 82 (102001) 2010.

Acknowledgements

I would like to express my gratitude to Karsten Danzmann for giving me the chance to be a PhD student in the then newly founded AEI 10 m prototype group. It was an unique experience to witness how a scientific project evolves from an empty hall to a stage at which the first interferometers operate in vacuum.

Acknowledgement to Benno Willke, who enthused me for the suspension platform interferometer. Although, the road towards a working SPI was sometimes a long and winding road, I never regretted my choice. Thank you Benno!

On this road, I had the pleasure to be accompanied by various people of the AEI 10 m prototype and LISA group. Thanks to Stefan Goßler, Harald Lück, and Gerhard Heinzel for being around and open to various questions. A big thank you to Michael Born for taking care of the phase meter interface and Conor Mow-Lowry for his last minute efforts to make the tables ready for the SPI. To the heiress to the SPI, Sina Köhlenbeck, thanks for the help in the last months and good luck in improving the SPI. Many thanks to the LISA folks for generously helping out with equipment and knowledge. To all my colleagues who are not named in person: thanks for valuable discussions and the nice atmosphere at the AEI.

Furthermore, thanks to Rana Adhikari for the invaluable opportunity to make a three months stay at the 40 m prototype at Caltech. It was truly enriching. Of course, thanks to Stefan Goßler for initiating this visit.

For proof reading of parts of this thesis I am truly grateful to (in alphabetic order): Christian Diekmann, Conor Mow-Lowry, Gudrun Wanner, Harald Lück, Heather Audley, Johanna Bogenstahl, Marina Dehne, Michael Born, Sina Köhlenbeck, Stefan Goßler, and Tobin Fricke. Your comments helped to improve this thesis. Thank you! Of course, any remaining mistakes and typos are my responsibility.

I thank Andreas Freise for being the Korreferent to this thesis and Christian Ospelkaus to chair the thesis defense.

To my family and Christian: thank you for you all-encompassing support.

Katrin Dahl, May 2013

About the author

Katrin Dahl, born on 16th June 1983 in Ludwigslust, Germany, received the Abitur from Goethe Gymnasium Ludwigslust in 2002. She studied physics at the Universität Rostock, Universität Regensburg, and Leibniz Universität Hannover. In 2007 she received her diploma degree in physics at the Leibniz Universität Hannover for work on transition from electromagnetically induced absorption to transparency in cesium. Since then she works as a research associate at Max-Planck-Institut für Gravitationsphysik (Albert-Einstein-Institut) and Institut für Gravitationsphysik, Leibniz Universität Hannover. In fall 2011, she was a visiting student researcher at California Institute of Technology, USA.